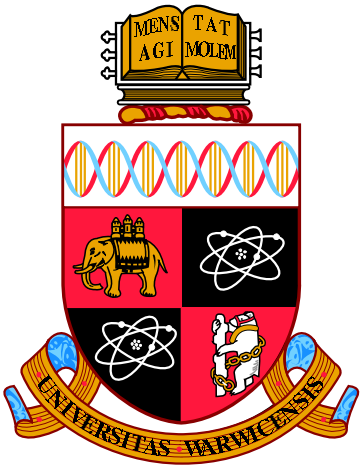

Magnetohydrodynamic Oscillations in Solar Coronal Rain

by

Petra Kohutova

Thesis

Submitted to the University of Warwick

for the degree of

Doctor of Philosophy

Department of Physics

May 2018

THE UNIVERSITY OF WARWICK

"Now I shall try what none has tried.
Now I shall do what none has done."

–Vladimir Nabokov, *Pale Fire*

Contents

List of Tables

List of Figures

Acknowledgments

First and foremost I am grateful to my supervisor Erwin Verwichte for all his help, support, encouragement and for keeping his sense of humour even when I lost mine. I would also like to thank the members of the ISSI coronal rain team for helpful discussions and insights during our meetings. I owe a special mention to Patrick Antolin and Gregal Vissers, my co-observers during the SST observation campaign at La Palma for their help and advice. I am also grateful to Tony Arber and Chris Brady for their patience with answering my more or less (usually more) clueless questions about the gory details of the Lare2d code. I feel obligated to thank the guys from the Centre for Scientific Computing for not brushing me off when requesting countless disk quota extensions.

I am further grateful to all the people in my life who were there for me unconditionally. First of all, to my family; to my mum, well, for everything, to my sister for making me laugh when I most needed it, and to my grandmother, who will sadly never see this finished, for all the nice memories. To Jaro for all the bike rides, laughs and spare chain links. To James for sharing my fondness for Mr. Pink, Bukowski's profanities, origami unicorns and for everything I've learned from him. To Sam Irvine and Simon Ridley for sharing the ups and downs of our PhD quest. To Tomas Forsberg for continuous inspiration and emotional support during late night coding sessions. And to Randall Munroe for making Monday mornings bearable.

Last but not least, I will always be grateful to Dan Mason for showing me that nothing was impossible if you believed in yourself*. The world needs more teachers like him.

*Except for avoiding existential crisis after learning about Copenhagen interpretation. That stuff ruins your childhood.

Declarations

This thesis is submitted to the University of Warwick in support of my application for the degree of Doctor of Philosophy. It has been composed by myself and has not been submitted in any previous application for any degree. The work presented in this thesis has been published in the following peer-reviewed journal articles:

1. P. Kohutova and E. Verwichte, Analysis of coronal rain observed by IRIS, HINODE/SOT, and SDO/AIA: Transverse oscillations, kinematics, and thermal evolution, ApJ, 2016, 827 39
2. P. Kohutova and E. Verwichte, Dynamics of plasma condensations in a gravitationally stratified coronal loop, A&A, 2017, 602 A23
3. P. Kohutova and E. Verwichte, Excitation of vertical coronal loop oscillations by plasma condensations, A&A, 2017, 606 A120
4. P. Kohutova and E. Verwichte, Excitation of vertical coronal loop oscillations by impulsively driven flows, A&A, 2018, in press

Abstract

Coronal rain composed of cool plasma condensations falling from coronal heights along magnetic field lines is a phenomenon occurring in active region coronal loops. This work combines high-resolution observations and numerical simulations to understand the interplay between coronal rain and MHD oscillations. We analyse oscillations and kinematics of the coronal rain using high resolution observations. Two different regimes of transverse oscillations traced by the rain are detected: small-scale persistent oscillations driven by a continuously operating process and localized large-scale oscillations excited by a transient mechanism. The plasma condensations are found to move with accelerations largely below the free-fall rate. The observed evolution of the emission of the plasma at the loop top is found to exhibit clear signatures of a gradual cooling consistent with the limit cycle model and suggests the loop is going through a sequence of periodically repeating heating-condensation cycles. We further investigate the evolution and dynamics of coronal rain using 2.5D MHD simulations. We model the evolution of a cool plasma condensation in a gravitationally stratified coronal loop. The motion of plasma condensations is found to be strongly affected by the pressure of the coronal loop plasma. High coronal magnetic field or low condensation mass are found to lead to damped oscillatory motion of the condensations. The combined effect of plasma pressure gradients and magnetic tension force can therefore explain observed sub-ballistic motion and longitudinal oscillations of coronal rain. We finally address the possibility of excitation of loop oscillations by coronal rain. We carry out MHD simulations of a coronal loop containing a cool and dense condensation region near the loop apex. This is found to excite fundamental harmonic of a vertically polarised kink mode. As the condensations fall towards the loop footpoints, the fundamental mode period is found to decrease as a result of the change in distribution of mass along the loop. We also carry out simulations of a coronal loop with a siphon flow between the footpoints which is likely to arise in asymmetrically heated loops. The action of the centrifugal force associated with plasma moving along the curved axis of the loop is found to excite vertically polarised loop oscillations. We find that flows with realistic speeds are sufficient to excite oscillations with observable amplitudes. We therefore propose coronal rain as a possible excitation mechanism for transverse loop oscillations.

Chapter 1

Introduction

1.1 The solar atmosphere

Solar activity has been subject to observations for thousands of years. Its manifestations range from local mass and energy transport processes to large scale events such as solar flares and coronal mass ejections (CMEs) which can directly influence the conditions on Earth. The level of solar activity is determined by the variations in the solar magnetic field. It varies with an 11 year solar cycle during which the polarity of the global solar magnetic field flips. The magnitude of the solar magnetic dipole moment varies from its maximum value at the solar minimum to nearly zero at solar maximum. The solar magnetic field is complex and originates in the solar interior. It is produced by the dynamo action in the tachocline, an interface layer between the radiative zone and the convection zone. The different rotation rates of the radiative zone, which rotates as a solid body and the convection zone, subject to differential rotation, result in strong shear flows leading to amplification of the magnetic field.

All of the directly observable solar activity takes place in the solar atmosphere. The solar atmosphere consists of multiple layers; photosphere, chromosphere, transition region and corona, each with different thickness and properties. The density of the solar atmosphere drops exponentially, while its temperature structure is more complex and its cause remains one of the open questions (Figure 1.1).

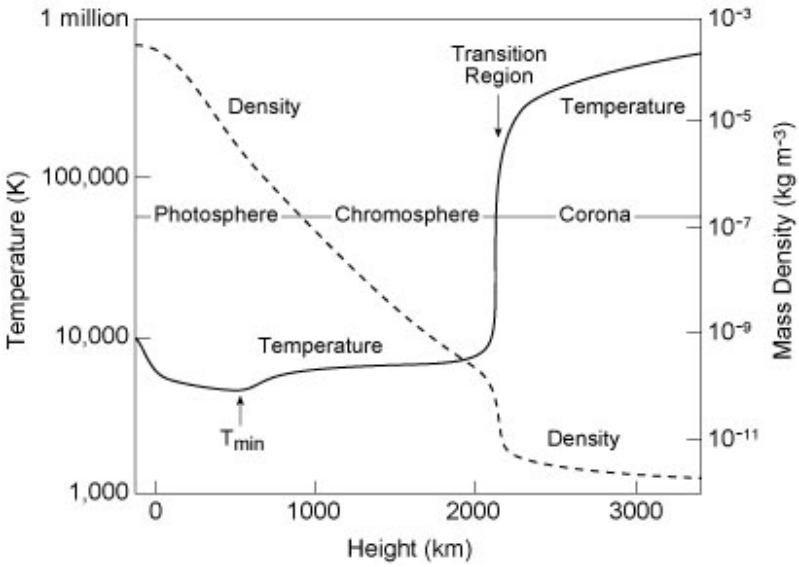

Figure 1.1: Temperature and density structure of the solar atmosphere as a function of height above the solar surface. Courtesy of E. Avrett.

1.1.1 Photosphere

Photosphere, or the visible surface of the sun is the lowermost layer of the solar atmosphere and emits most of the solar radiation in visible, UV and IR wavelengths. Its temperature varies between 4000 and 6000 K and decreases with increasing height. The electron number density also decreases with height and varies between 10^{21} - 10^{23} m^{-3}. The opacity is predominantly caused by the H^- bound-free absorption and with height decreases sufficiently for the photons to be able to escape [Foukal, 2004]. The photosphere can be approximated as being in local thermodynamic equilibrium (LTE), such that the level populations are determined by the Saha-Boltzmann statistics depending on the local temperature [Gray, 2005]. The small scale photospheric structure is formed by granulation [Spruit et al., 1990]. Granules are small cells of plasma with diameter of the order of 1000 km and lifetime of about 20 minutes. They correspond to the the top of the convective cells where hot plasma rises upwards in the bright cell centres, spreads out, cools and then sinks downwards along the dark cell edges. Their large-scale versions are known as supergranules, measure 10 000s of km across and typically last days. They correspond to large scale flows carrying bundles of magnetic field lines and forming the edges of chromospheric network. The dark regions of concentrated magnetic flux are known as sunspots and are cooler than the surrounding plasma with the typical temperature in the sunspot centre, or umbra being around 3700 K [Solanki,

2003]. Sunspot magnetic fields are of the order of 1000 G and typically connect two groups of sunspots; one having positive and another one with negative polarity. Such bipolar magnetic field configurations with large extent are known as active regions and are often locations of intense magnetic activity that can lead to eruptive events like flares and CMEs. Lifetimes of sunspots range from days to several weeks. The sunspot number, defined as $R = k(10g + s)$ with s being the number of sunspots, g the number of sunspot groups and k the scaling factor based on observing conditions, varies with the solar cycle phase and has long been used as a solar cycle proxy. As the solar cycle progresses from maximum to minimum, the sunspots migrate from higher latitudes towards the equator. Faculae are small bright areas that also correspond to the regions of concentrated magnetic field, although with magnitudes much smaller than in sunspots [Dumont et al., 1982; Keller et al., 2004]. The photosphere is a high β plasma where gas pressure dominates over magnetic pressure and the magnetic field is moved along by the fluid flows. The photospheric magnetic field is non-uniformly distributed and accumulates in flux tubes. These originate in the upper layers of the convection zone and rise towards the surface due to magnetic buoyancy [Parker, 1955] in the process known as flux emergence.

1.1.2 Chromosphere

Above the photosphere the temperature starts to increase again from the photospheric temperature minimum to reach a maximum of 10 000 - 20 000 K. The density of the chromosphere decreases rapidly from 10^{15} to 10^{11} cm^{-3} and the LTE approximation breaks down. The thickness of the chromosphere is about 2000 km. Chromospheric plasma is partially ionised and optically thin for continuum radiation, but optically thick for many important emission lines such as H-alpha, Mg II H and K and Ca II H and K lines [Athay, 1976]. The plasma-β of the chromospheric plasma varies with height, the chromosphere therefore contains both magnetic pressure dominated and gas pressure dominated regions. The chromosphere is therefore non-homogeneous and highly structured (Figure 1.2). The aforementioned chromospheric network is best visible in H-alpha line and forms a web-like pattern across the solar disk. Masses of cool chromospheric plasma suspended in the coronal heights and supported against gravity are known as prominences and are most easily observed in emission at the solar limb [Labrosse et al., 2010; Mackay et al., 2010; Parenti, 2014]. When located on-disk, they appear as dark string-like structures and are referred to as filaments. Most prominences are quiescent and typically remain in a quasi-equilibrium state for days or even weeks. However, when the equilibrium is

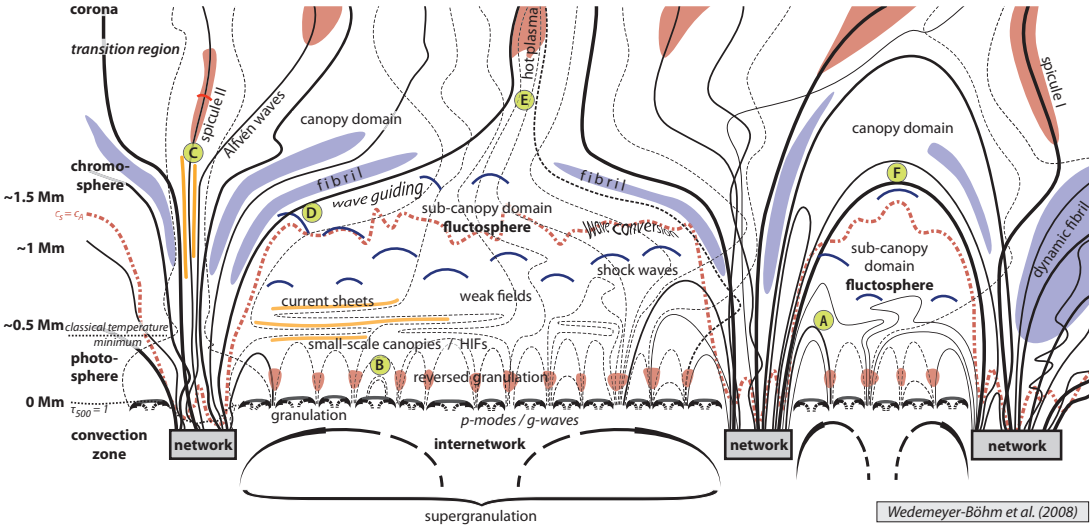

Figure 1.2: Atmospheric structure of quiet Sun regions. Taken from Wedemeyer-Böhm et al. [2009].

lost, mostly due to an internal instability growth, the magnetic structure supporting the prominence is destabilised leading to sudden eruption. Prominence eruptions are often associated with CMEs, with CME cavities often containing cores of prominence remnants. Another type of abundant features observable in the chromospheric wavelength are spicules, short and spike-like jets of chromospheric plasma with short lifetimes on the order of minutes [Sterling, 2000; De Pontieu and Erdélyi, 2006].

1.1.3 Transition region

The thin layer between the chromosphere and the corona of 100 km thickness corresponds to the transition region where the temperature increases rapidly from 10 000 K to millions of K and the density drops to 10^{15} m^{-3}. The transition region is almost completely ionised and emits mostly in C IV, O IV, and Si IV lines in the UV part of the spectrum. It is subject to various mass and energy transport processes from the chromosphere to the corona and therefore non-uniform.

1.1.4 Corona

The corona is the outermost layer of the solar atmosphere extending into interplanetary space. The temperature in the corona reaches millions of K while the typical

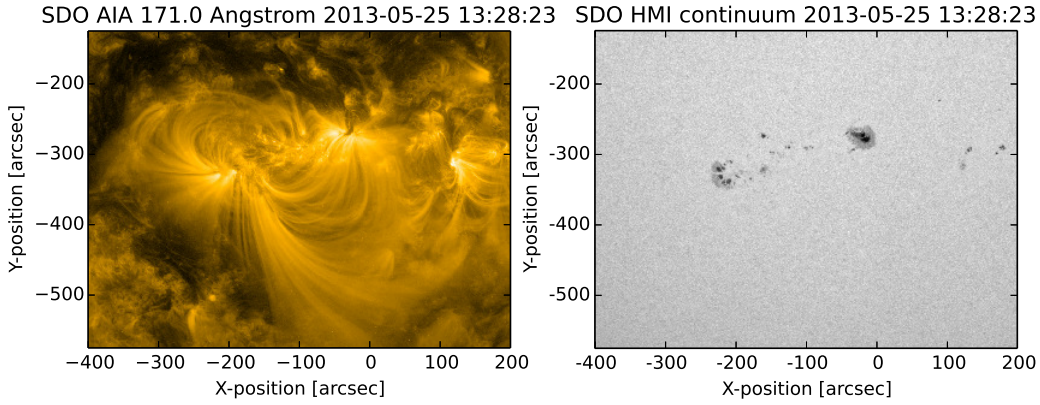

Figure 1.3: Left: Active region as seen by SDO/AIA 171 Å. Right: SDO/HMI continuum.

coronal densities at heights of the order of 100 Mm above the solar surface are around 10^{14}-10^{15} m^{-3}. The reasons behind the high coronal temperatures, known as coronal heating problem, have been for long subject of active research. This comprises questions about the source of the energy heating the corona and how this energy is transported into and dissipated in the corona as heat. Complete answers to these require accurate knowledge of coronal conditions and parameters such as coronal density and magnetic field which can be measured only indirectly and have large uncertainties associated with them. High coronal temperatures mean that the corona primarily emits in EUV and X-ray wavelengths. Standard coronal diagnostic emission lines are Lyman-α (1216 Å) and ionised iron lines such as the Fe XVIII (94 Å), Fe VIII, XXI (131 Å), Fe IX (171 Å), Fe XII, XXIV (193 Å), Fe XIV (211 Å) and Fe XVI (335 Å). Because of high temperatures the corona is almost fully ionised and the optically thin approximation is valid in this case. The corona is a low β plasma and therefore dominated by the magnetic pressure. The structure of the corona is complex and formed by flux tubes filled with hot plasma, known as coronal loops (Figure 1.3). Other coronal structures include coronal holes, regions associated with open magnetic field lines located predominantly at the poles. Coronal holes are the source of high speed solar wind [Cranmer, 2009]. Helmet streamers are large long-lived cusp-shaped structures extending several solar radii above the solar limb. They lie above active regions and often contain a prominence at the base. They consist of two parts, bottom part containing closed magnetic field lines and an extended pointed peak associated with open magnetic field that is formed by the action of the solar wind [Pneuman, 1968]. Polar plumes are long thin streams of plasma located near the poles formed by the action of solar wind that are associated

with small magnetic regions [Poletto, 2015].

Coronal loops

The basic building structures of the corona are coronal loops, magnetic flux tubes anchored to the solar surface at both ends confining the hot plasma. Their lengths vary from tens of Mm (short post flare loops) to hundreds of Mm (large active region loops). The simplest coronal loop models assume hydrostatic equilibrium, meaning the plasma in the loop is stratified such that the balance between the gravity and plasma pressure is satisfied. The stratification scale height is dependent on the temperature and density structure of the loop plasma. Including a constant heating rate and a single power law radiative loss function leads to the RTV scaling law [Rosner et al., 1978]:

$$T_{\max} = 14000(p_0 L)^{1/3} \tag{1.1}$$

$$E_{\mathrm{H0}} = 9.5 \times 10^{-12} T_{\max}^{7/2} L^{-2}\,, \tag{1.2}$$

where $T_{\max}$ is the temperature at the loop top, p_0 is the base pressure, E_{H0} is the uniform heating rate and L is the length of the loop. If the coronal magnetic field is assumed to be potential, loops need to have variable cross-section in order to satisfy conservation of the magnetic flux. Loop expansion factor is therefore greater than 1 which has implication for modelling the coronal loop dynamics. However, in practice most coronal loops are out of hydrostatic equilibrium and subject to a range of mass and energy transport processes [Aschwanden et al., 2001]. These include direct injection of the matter from the chromosphere, chromospheric evaporation and condensation, transport and loss of thermal energy via thermal conduction and radiation and siphon flows caused by the pressure difference in different regions of the loop. More sophisticated coronal loop models therefore need to account for these. In addition, there is a number of macroscopic instabilities likely to occur in coronal loops that affect the loop state and evolution. The Rayleigh-Taylor instability occurs when the density gradient of the coronal loop plasma has an opposite direction to gravity. A perturbation to this state triggers the development of growing ripples at the fluid boundary [Priest, 1978]. The Kelvin-Helmholtz instability arises from shear flows at the interface of fluids with different velocities. This type of instability is likely to occur if the flow occurs in the direction perpendicular to the axis of the coronal loop, e.g. during transverse motion of the coronal loop relative to the background plasma [Terradas et al., 2008; Antolin et al., 2014]. This is due to the

stabilizing effect of the magnetic field along the loop. The shear flows then lead to the development of Kelvin-Helmholtz vortices at the loop boundary. The kink instability corresponds to growing transverse displacement along a fluxtube and can occur in coronal loops with finite azimuthal magnetic field component [Anzer, 1968; Hood and Priest, 1979]. If a coronal loop with a magnetic field twist exceeding a critical value is displaced in a transverse direction, the magnetic field lines along the inner side of the kink are pushed closer together, leading to an increase of the magnetic pressure at the inner side. Conversely, at the outer side of the kink the field lines are pushed apart, leading to the decrease of magnetic pressure. This creates a net outward force in the same direction as the displacement, resulting in an instability growth and eventually in an eruption. The kink instability is likely to play an important role in prominence eruptions and in the onset of solar flares and CMEs. Thermal instability occurs in coronal loops heated predominantly at the footpoints. If the heating is spatially concentrated and the thermal conduction along the loop is inefficient, the radiative losses from the upper parts of the loop can overcome the heating input leading to catastrophic cooling of the plasma at the loop top [Field, 1965].

Coronal magnetic field

Coronal magnetic fields have complex structure and are responsible for some of the most violent events occurring in the solar atmosphere. Detailed knowledge of the coronal magnetic field geometry and topology is essential as it provides a direct link between theoretical models and solar observations. Direct measurements of coronal magnetic fields are however difficult and subject to large uncertainties compared to the typical magnetic field magnitudes. The structure of the coronal magnetic field is therefore usually determined indirectly and can be obtained either by using coronal loops as a proxy for magnetic field lines or using a more sophisticated approach based on extrapolation of photospheric magnetic field vectors. The approach based on stereoscopy relies on having solar observations taken from 2 different vantage points, enabling full 3D reconstruction of coronal loops. This was one of the primary aims of the STEREO mission consisting of two identical spacecraft orbiting the Sun at varying separation [Kaiser, 2005]. Magnetic field extrapolation models on the other hand require knowledge of the photospheric magnetic field, typical values of which are orders of magnitude larger than the coronal values and therefore easier to measure. The surface magnetic fields are determined by measuring Zeeman splitting of spectral lines and by using Stokes spectropolarimetry to obtain

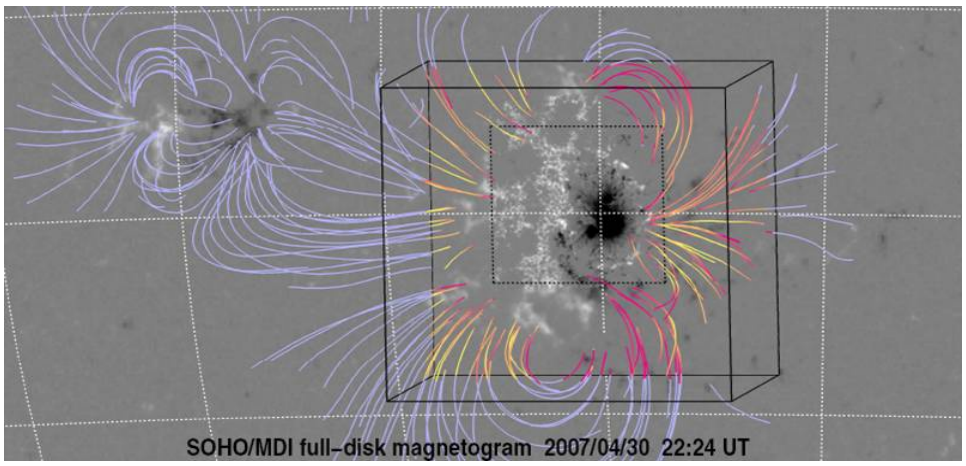

Figure 1.4: Part of SOHO/MDI magnetogram and the corresponding magnetic field reconstructed using STEREO data. Taken from DeRosa et al. [2009].

all three components of the magnetic field vector. This is done by magnetograph instruments and spectropolarimeters in both space and ground based observatories (these include SDO/HMI [Scherrer et al., 2012], Hinode SOT/SP [Tsuneta et al., 2008] and CRISP at SST [Scharmer, 2006]) providing solar magnetograms such as one shown in Figure 1.4. Current state of the art magnetic field models rely on solving non-linear force free field equations with the boundary conditions determined from the surface magnetograms.

1.2 Magnetohydrodynamics

Plasma, known as the fourth state of matter, is an ionised gas consisting of ions and electrons. It is created by heating the gas or by subjecting it to strong electromagnetic field such that the electrostatic forces binding the electrons and ions together are overcome and electrons are stripped from the atomic nuclei. Plasma is the most common state of matter in the universe, but does not naturally occur on Earth, except for thunderstorms and aurorae.

Magnetohydrodynamics is based on modelling the plasma as an electrically conducting fluid. The particles interact with each other via long range Coulomb forces leading to collective movements, thus making the continuous fluid description applicable. It can be used to describe dynamics of plasmas on large spatial and long temporal scales. The properties of a plasma need to satisfy a number of assumptions for the MHD approximation to be valid. Firstly, it is assumed that plasma is

strongly collisional such that the distribution of particles is Maxwellian. The characteristic length scales are much longer that the mean free path of the particles and the characteristic time scales are long compared to the collisional time. Secondly, characteristic length scales are assumed to be much longer that the ion skin depth and ion gyroradius. Similarly, characteristic time scales are much longer that the ion gyroperiod. Finally, it is assumed that plasma velocities are not relativistic. Under these assumptions the plasma is governed by the Navier-Stokes equations of fluid dynamics and by the Maxwell's equations without the displacement current, together forming a self-consistent set of MHD equations.

1.2.1 MHD equations

Firstly, the mass continuity equation is

$$\frac{\partial \rho}{\partial t} + \vec{\nabla} \cdot (\rho \vec{V}) = 0 \,, \tag{1.3}$$

where ρ is the plasma density and $\vec{V}$ is the plasma velocity and implies that the matter is neither created nor destroyed. D/Dt is the advective derivative, i.e. derivative evaluated in the frame comoving with the fluid:

$$\frac{D}{Dt} = \frac{\partial}{\partial t} + \vec{V} \cdot \vec{\nabla} \,. \tag{1.4}$$

The momentum equation is

$$\rho \frac{D\vec{V}}{Dt} = -\vec{\nabla} p + \rho \vec{g} + \frac{1}{\mu_0} (\vec{\nabla} \times \vec{B}) \times \vec{B} \,, \tag{1.5}$$

where p is the pressure and is equivalent to Newton's second law applied to conductive fluid. Here the change of the momentum of the fluid element is equal to the sum of pressure gradient force, Lorentz force and gravity. The Lorentz force term can be expanded as

$$\frac{1}{\mu_0} (\vec{\nabla} \times \vec{B}) \times \vec{B} = \frac{1}{\mu_0} (\vec{B} \cdot \vec{\nabla}) \vec{B} - \vec{\nabla} \Big(\frac{B^2}{2\mu_0} \Big) \,, \tag{1.6}$$

where $(\vec{B} \cdot \vec{\nabla}) \vec{B} / \mu_0$ is the magnetic tension or restoring force resisting bending of the magnetic field lines and $-\vec{\nabla} \Big(B^2 / 2\mu_0 \Big)$ is the magnetic pressure force resisting

the accumulation of the magnetic flux. The energy equation is given by

$$\frac{1}{(\gamma-1)}\frac{Dp}{Dt}+\frac{\gamma}{\gamma-1}p\vec{\nabla}\cdot\vec{V}=E_{\rm H}-E_{\rm R}-\vec{\nabla}F_{\rm C}\,, \tag{1.7}$$

where γ is the ratio of specific heats ($\gamma = 5/3$ for fully ionised plasma), $E_{\rm H}$ is the rate of heating per unit volume, $E_{\rm R}$ is the rate of radiative losses per unit volume and $F_{\rm C}$ is the conductive flux. The temperature T is determined by p and ρ using the ideal gas law:

$$p=\frac{\rho k_{\rm B}T}{\mu}\,, \tag{1.8}$$

where $k_{\rm B}$ is Boltzmann constant and $\mu = \rho/n$, n being the particle number density, is the reduced mass, approximately equal to 0.5 $m_{\rm p}$ for ionised hydrogen. The magnetic field $\vec{B}$ satisfies the solenoidal condition

$$\vec{\nabla}\cdot\vec{B}=0\,. \tag{1.9}$$

The induction equation can be obtained from generalised Ohm's law:

$$\frac{1}{\sigma}\vec{j}=\vec{E}+\vec{V}\times\vec{B}\,, \tag{1.10}$$

where $\vec{j}$ is the current density, $\vec{E}$ is the electric field and σ is the conductivity. The resistivity $1/\sigma$ is significant when $|\vec{\nabla}\times\vec{B}|$ is large, e.g. in current sheets and can be neglected under quiet sun coronal conditions. Assuming perfect conductivity and substituting Eq. (1.10) into Faraday's law given by

$$\frac{\partial\vec{B}}{\partial t}=-\vec{\nabla}\times\vec{E}\,, \tag{1.11}$$

leads to the induction equation in its standard form when neglecting the resistivity:

$$\frac{\partial\vec{B}}{\partial t}=\vec{\nabla}\times(\vec{V}\times\vec{B})\,. \tag{1.12}$$

The ratio of the thermal plasma pressure to magnetic pressure is known as the plasma-β:

$$\beta=\frac{p}{B^2/2\mu_0}\,. \tag{1.13}$$

The magnitude of the plasma-β determines the behaviour of the plasma. For $\beta > 1$, as is the case in the solar interior, the plasma pressure dominates and magnetic field is pushed around by the fluid. For $\beta < 1$, as is the case in the solar corona, the magnetic pressure dominates and the behaviour of the plasma is controlled by

the magnetic field. In both cases, due to high conductivity, the plasma obeys the frozen-in flux approximation and the plasma particles are magnetically confined.

1.2.2 MHD waves

Plasmas can support a variety of waves. The individual wave modes can be investigated by first considering the simplest equilibrium case of a uniform, static magnetised plasma for which $\partial/\partial t = 0$ and $\vec{V} = 0$. Considering small perturbations to the equilibrium quantities:

$$\begin{aligned}
\vec{B}(\vec{r},t) &= \vec{B}_0 + \vec{B}'(\vec{r},t) && (1.14)\\
\vec{V}(\vec{r},t) &= 0 + \vec{V}'(\vec{r},t) && (1.15)\\
p(\vec{r},t) &= p_0 + p'(\vec{r},t) && (1.16)\\
\rho(\vec{r},t) &= \rho_0 + \rho'(\vec{r},t)\,, && (1.17)
\end{aligned}$$

where the perturbations are represented by the primed quantities. Substituting the above into ideal MHD equations (i.e. not considering thermal conduction, radiative losses and heating terms in the energy equation) and neglecting nonlinear terms leads to a set of linearised MHD equations:

$$\begin{aligned}
\frac{\partial \rho'}{\partial t} + \rho_0 \vec{\nabla}\cdot\vec{V}' &= 0 && (1.18)\\
\rho_0 \frac{\partial \vec{V}'}{\partial t} &= -\vec{\nabla}p' + \vec{j}' \times \vec{B}_0 && (1.19)\\
\frac{\partial p'}{\partial t} &= -(\vec{V}'\cdot\vec{\nabla})p_0 - \gamma p_0 \vec{\nabla}\cdot\vec{V}' && (1.20)\\
\frac{\partial \vec{B}'}{\partial t} &= \vec{\nabla}\times(\vec{V}'\times\vec{B}_0)\,. && (1.21)
\end{aligned}$$

The first wave equation can be determined from the component of the linearised induction equation parallel to $\vec{B}_0$:

$$\frac{\partial \vec{B}'}{\partial t}\cdot\vec{B}_0 = -B_0^2\vec{\nabla}\cdot\vec{V}' + B_0(\vec{B}_0\cdot\vec{\nabla})\vec{V}'_{\parallel}\,. \qquad (1.22)$$

Taking the time derivative of the above leads to

$$\frac{\partial^2 \vec{B}'}{\partial t^2}\cdot\vec{B}_0 = -B_0^2\frac{\partial(\vec{\nabla}\cdot\vec{V}')}{\partial t} + B_0(\vec{B}_0\cdot\vec{\nabla})\frac{\partial v_{\parallel}}{\partial t}\,. \qquad (1.23)$$

We note that

$$\vec{B}' \cdot \vec{B}_0 = \mu_0(p'_{\rm T} - p')\,, \tag{1.24}$$

where $p'_{\rm T}$ is the total pressure perturbation equal to the sum of magnetic and thermal plasma pressure perturbations. Further using the expressions for the parallel component and divergence of the momentum following from the momentum equation:

$$\rho_0 \frac{\partial V'_\parallel}{\partial t} = -(\vec{1}_\parallel \cdot \vec{\nabla})p' \tag{1.25}$$

$$\rho_0 \frac{\partial(\vec{\nabla} \cdot \vec{V}')}{\partial t} = -\nabla^2 p'_{\rm T}\,, \tag{1.26}$$

and substituting these into Eq. (1.23) leads to

$$\frac{\partial^2 p'_{\rm T}}{\partial t^2} = \frac{\partial^2 p'}{\partial t^2} + \frac{B_0^2}{\mu_0\rho_0}\nabla^2 p'_{\rm T} - \frac{B_0^2}{\mu_0\rho_0}(\vec{1}_\parallel \cdot \vec{\nabla})^2 p'\,, \tag{1.27}$$

where $\vec{1}_\parallel = \vec{B}_0/B_0$ is the unit vector in the direction of the magnetic field. Taking the time derivative of the above equation twice and substituting the expressions for the Alfvén speed $V_{\rm A}$ and sound speed $C_{\rm S}$ given by

$$V_{\rm A} = \frac{B_0}{\sqrt{\mu_0\rho_0}} \tag{1.28}$$

$$C_{\rm S} = \sqrt{\frac{\gamma p_0}{\rho_0}}\,, \tag{1.29}$$

results in the magnetoacoustic wave equation:

$$\frac{\partial^4 p'_{\rm T}}{\partial t^4} - C_{\rm S}^2\frac{\partial^2}{\partial t^2}\nabla^2 p'_{\rm T} + V_{\rm A}^2\frac{\partial^2}{\partial t^2}\nabla^2 p'_{\rm T} + C_{\rm S}^2 V_{\rm A}^2(\vec{1}_\parallel \cdot \vec{\nabla})^2\nabla^2 p'_{\rm T} = 0\,. \tag{1.30}$$

Assuming plane wave solutions leads to a dispersion relation:

$$\omega^4 - (C_{\rm S}^2 + V_{\rm A})k^2\omega^2 + C_{\rm S}^2 V_{\rm A}^2 k_\parallel^2 k^2 = 0\,. \tag{1.31}$$

The solution to the above is

$$\omega^2 = \frac{1}{2}(C_{\rm S}^2 + V_{\rm A}^2)k^2\left[1 \pm \sqrt{1 - 4\frac{C_{\rm T}^2}{(C_{\rm S}^2 + V_{\rm A}^2)}\frac{k_\parallel^2}{k^2}}\right], \tag{1.32}$$

where C_{T} is the tube speed given by

$$C_{\mathrm{T}} = \frac{C_{\mathrm{S}} V_{\mathrm{A}}}{\sqrt{C_{\mathrm{S}}^2 + V_{\mathrm{A}}^2}} \,. \tag{1.33}$$

The negative sign solution corresponds to the slow magnetoacoustic wave and the positive sign solution corresponds to the fast magnetoacoustic wave. The phase speed diagrams for both types of waves in different plasma-β limits are shown in Figure 1.5. Both types of waves are polarised in the plane given by $\vec{k}$ and $\vec{B}_0$ and have both longitudinal and transverse components. In both cases, the restoring forces are the plasma pressure and the magnetic pressure forces. In the slow wave case, the magnetic and plasma pressure perturbations are in antiphase and they partially cancel out. The slow waves are anisotropic and don't propagate in the direction perpendicular to the magnetic field. The energy flow is also anisotropic and is most pronounced in the direction of the magnetic field. In the fast wave case, the plasma and magnetic pressure perturbations are in phase. The fast waves are nearly isotropic and so is the energy flow.

Similarly, the Alfvén wave equation can be obtained using the parallel component of the Ampère's law:

$$\mu_0 j'_{\parallel} = (\vec{\nabla} \times \vec{B}') \cdot \vec{1}_{\parallel} \,, \tag{1.34}$$

where $j'_{\parallel}$ is the current density perturbation. Taking the time derivative of Eq. (1.34) leads to

$$\mu_0 \frac{\partial j'_{\parallel}}{\partial t} = (\vec{\nabla} \times \frac{\partial \vec{B}'}{\partial t}) \cdot \vec{1}_{\parallel} \,. \tag{1.35}$$

Substituting parallel component of the induction equation gives

$$\mu_0 \frac{\partial j'_{\parallel}}{\partial t} = (\vec{B}_0 \cdot \vec{\nabla})(\vec{\nabla} \times \vec{V}') \cdot \vec{1}_{\parallel} \,. \tag{1.36}$$

The time derivative of the above is

$$\mu_0 \frac{\partial^2 j'_{\parallel}}{\partial t^2} = (\vec{B}_0 \cdot \vec{\nabla}) \frac{\partial}{\partial t} (\vec{\nabla} \times \vec{V}') \cdot \vec{1}_{\parallel} \,. \tag{1.37}$$

Substituting the curl of the momentum equation leads to the Alfvén wave equation:

$$\frac{\partial^2 j'_{\parallel}}{\partial t^2} - V_{\mathrm{A}}^2 (\vec{1}_{\parallel} \cdot \vec{\nabla})^2 j'_{\parallel} = 0 \,. \tag{1.38}$$

This leads to dispersion relation

$$\omega^2 = V_{\mathrm{A}}^2 k_{\parallel}^2 \,. \tag{1.39}$$

The solution is given by

$$j'_{\parallel} = A\mathrm{e}^{i(k_{\parallel}x_{\parallel} - \omega t)} + B\mathrm{e}^{i(k_{\parallel}x_{\parallel} + \omega t)} \,, \tag{1.40}$$

i.e. the Alfvén waves propagate along the magnetic field at the speed V_{A}. The restoring force in this case is the magnetic tension force. Alfvén waves are transverse, the velocity and magnetic field perturbations are perpendicular to $\vec{B}_0$. In the linear case the Alfvén waves are incompressible, there are no associated density or pressure perturbations. They are anisotropic and cannot propagate energy across the magnetic field lines. The energy flow is purely along the direction of the magnetic field.

1.2.3 Waves in magnetic cylinder

Coronal plasma is confined within coronal loops that act as waveguides. Their oscillatory behaviour can therefore be determined by modelling them as long straight cylinders. In order to be able to determine wave solutions of the MHD equations in the cylindrical geometry analytically, a simplified model of a uniform cylinder embedded in a magnetic environment with constant magnetic field along the z-direction is introduced. Following the analysis done by Edwin and Roberts [1983], the pressure balance at the cylinder boundary requires

$$p_0 + \frac{B_0^2}{2\mu_0} = p_{\mathrm{e}} + \frac{B_{\mathrm{e}}^2}{2\mu_0} \,. \tag{1.41}$$

where subscripts 0 and e correspond to quantities inside the cylinder and in the external medium respectively. The solution is assumed to be of the form

$$p'_{\mathrm{T}}(\vec{r}, t) = \tilde{p}_{\mathrm{T}}(r) \exp i(kz + n\theta + \omega t) \,. \tag{1.42}$$

Substituting this into the wave equations (1.30) and (1.38) leads to a Bessel differential equation for the pressure perturbations:

$$\frac{d^2\tilde{p}_{\mathrm{T}}}{dr^2} + \frac{1}{r}\frac{d\tilde{p}_{\mathrm{T}}}{dr} - (m_0^2 + \frac{n^2}{r^2})\tilde{p}_{\mathrm{T}} = 0 \,, \tag{1.43}$$

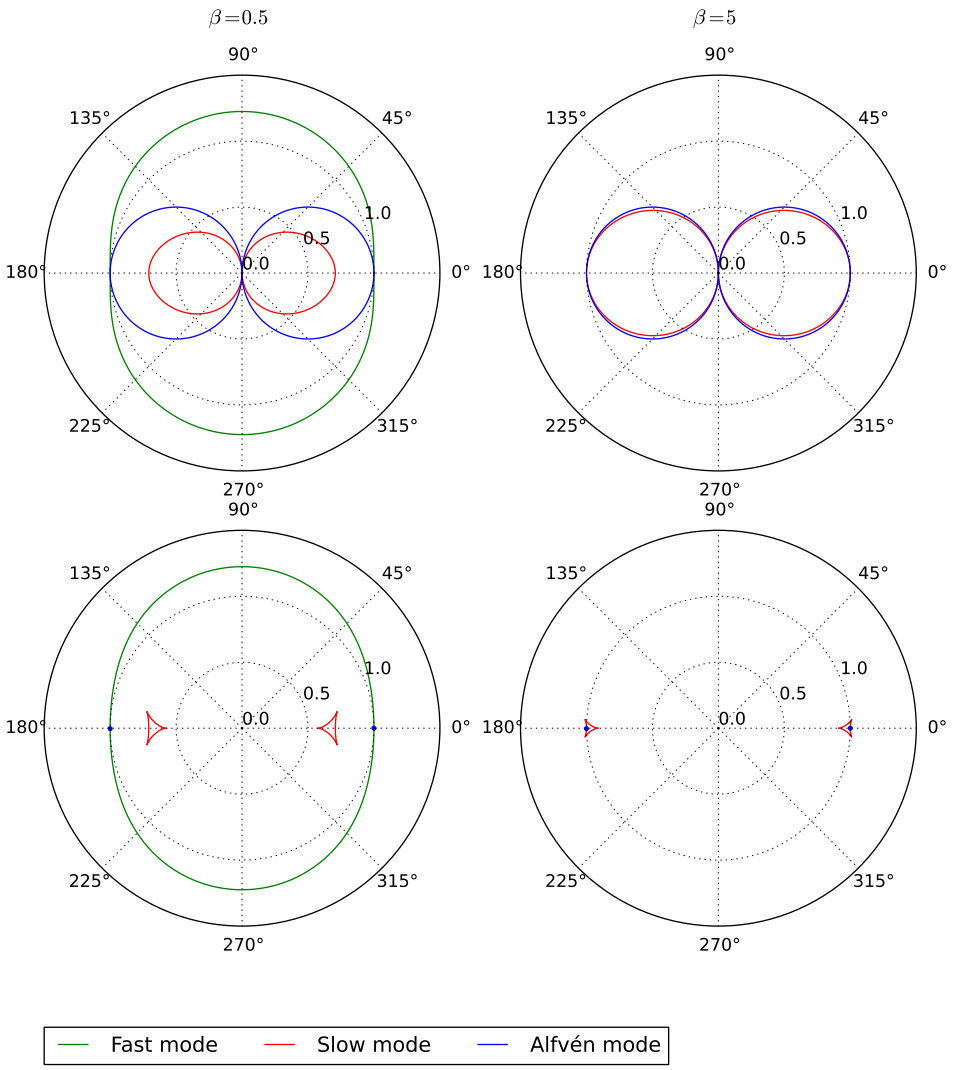

Figure 1.5: Diagram of phase speed (top) and group speed (bottom) of fast, slow and Alfvén modes for $\beta < 1$ (left) and $\beta > 1$ (right) normalised to the Alfvén speed. Polar coordinate corresponds to the angle between $\vec{k}$ and $\vec{B}_0$.

where

$$m_0^2 = \frac{(k^2 C_{\rm S0}^2 - \omega^2)(k^2 V_{\rm A0}^2 - \omega^2)}{(C_{\rm S0}^2 - V_{\rm A0}^2)(k^2 C_{\rm T0}^2 - \omega^2)}\,, \tag{1.44}$$

is the square of the radial wavenumber. C_T is given by:

$$C_{\rm T} = \frac{C_0 V_{\rm A}}{(C_0^2 + V_{\rm A}^2)^{\frac{1}{2}}}\,. \tag{1.45}$$

The solutions are given by Bessel functions:

$$\tilde{p}_{\rm T} = A_0 \begin{cases} I_n(m_0 r), & m_0^2 > 0 \\ J_n(n_0 r), & n_0 = -m_0^2 > 0 \end{cases} \tag{1.46}$$

if $r < a$, i.e. inside the cylinder and

$$\tilde{p}_{\rm T} = A_1 K_n(m_{\rm e} r)\,, \tag{1.47}$$

outside the cylinder. Here A_0 and A_1 are constants, I_n, J_n and K_n are Bessel functions of order n and $m_{\rm e}$ is given by

$$m_e^2 = \frac{(k^2 C_{\rm Se}^2 - \omega^2)(k^2 V_{\rm Ae}^2 - \omega^2)}{(C_{\rm Se}^2 - V_{\rm Ae}^2)(k^2 C_{\rm T0}^2 - \omega^2)}\,. \tag{1.48}$$

Requiring continuity of the radial velocity component and of the total pressure at the cylinder boundary then leads to dispersion relations

$$\rho_0(k^2 V_A^2 - \omega^2) m_e \frac{K_n'(m_e a)}{K_n(m_e a)} = \rho_e(k^2 V_{Ae}^2 - \omega^2) m_0 \frac{I_n'(m_0 a)}{I_n(m_0 a)}\,, \tag{1.49}$$

for surface waves ($m_0^2 > 0$) and

$$\rho_0(k^2 V_A^2 - \omega^2) m_e \frac{K_n'(m_e a)}{K_n(m_e a)} = \rho_e(k^2 V_{Ae}^2 - \omega^2) n_0 \frac{J_n'(n_0 a)}{J_n(n_0 a)}\,, \tag{1.50}$$

for body waves ($m_0^2 < 0$). Here $K_n'(m_{\rm e} a) = (d/dx)K_n(x)$ evaluated at $x = m_{\rm e} a$. Solutions to the above dispersion relations are shown in Figure 1.6.

Under coronal conditions where typically $V_{\rm Ae}$, $V_{\rm A} > C_{\rm S}$, $C_{\rm Se}$ there are two classes of body modes and no surface modes. If $V_{\rm Ae} > V_{\rm A}$, i.e. in the case of high internal density, the cylinder can sustain fast body waves with periods corresponding to Alfvénic time scales. The slow modes, on the other hand, arise in both high and low internal density cases. $n = 0$ corresponds to fast sausage modes which are azimuthally sym-

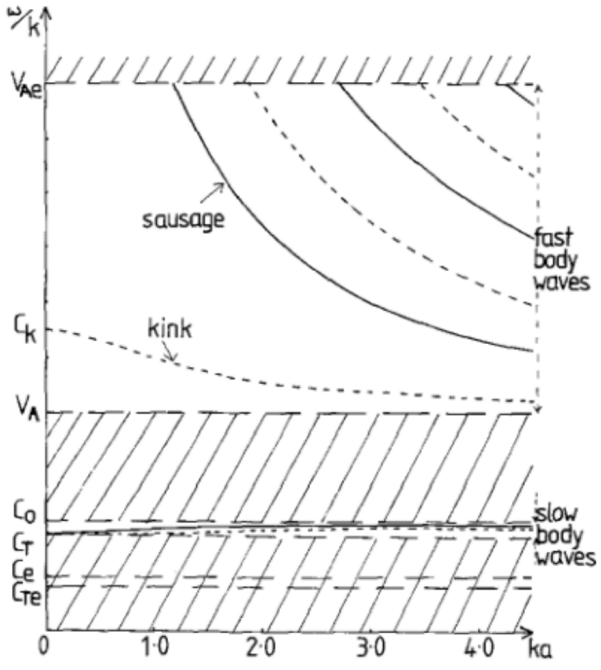

Figure 1.6: Phase speed diagram for MHD modes of magnetic cylinder taken from Edwin and Roberts [1983] valid under coronal conditions.

metric, $n = 1$ corresponds to fast kink modes which are azimuthally antisymmetric, and $n > 1$ corresponds to fluting or balooning modes. The characteristic speed of propagation of the sausage mode C_T is known as tube speed and is defined in Eq. (1.33) and the characteristic speed of the kink mode $C_{\rm k}$ is known as kink speed and is given by

$$C_k = \Big(\frac{\rho_0 V_{\rm A0}^2 + \rho_{\rm e} V_{\rm Ae}^2}{\rho_0 + \rho_{\rm e}}\Big)^{1/2}. \tag{1.51}$$

Sausage modes are compressible and perturb the cylinder cross-section without affecting the cylinder axis. Kink modes on the other hand are nearly incompressible and displace the axis of the cylinder. As shown in Figure 1.6, sausage modes have a low wavenumber cut-off at $ka \sim 1$, which means that the cylinder can only support higher order harmonics of the sausage mode with wavelengths comparable to its radius. At low wavenumbers the sausage mode becomes leaky and the energy is radiated into the external medium. This does not apply to the kink mode for which also lower order harmonics are supported. The period of the fundamental harmonic of kink mode is given by

$$\tau = \frac{2L}{C_{\rm k}}, \tag{1.52}$$

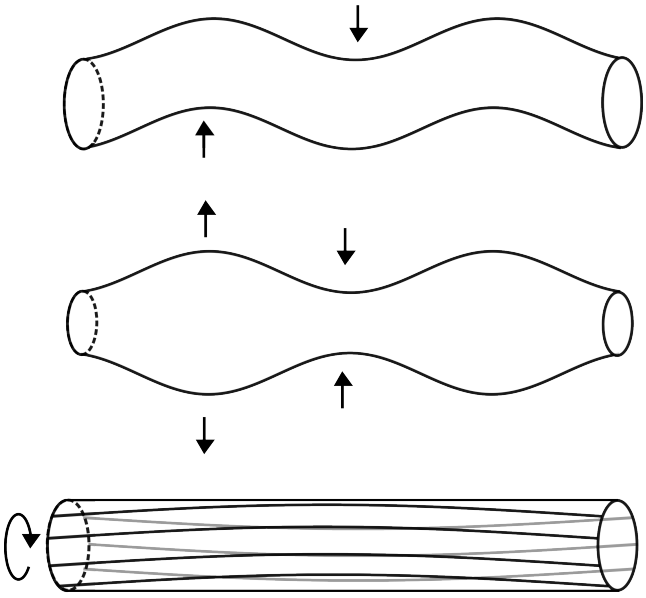

Figure 1.7: MHD modes of magnetic cylinder: kink (top), sausage (middle) and torsional Alfvén mode (bottom).

where L is the length of cylinder. In contrast, typical periods of the sausage modes are much shorter as only higher order harmonics are present. Finally, Alfvén modes propagate with characteristic speed V_{A} and correspond to the torsional motion of the cylinder with the velocity in the azimuthal direction. They perturb neither the cylinder cross-section nor cylinder axis and hence do not cause intensity variations in the cylinder.

1.3 Thermal instability and coronal rain

The otherwise hot and diffuse solar corona contains numerous cool and dense plasma structures in the form of prominences and coronal rain. Coronal rain consists of cool plasma condensations falling from coronal heights to the solar surface guided by the magnetic field lines [Schrijver, 2001; De Groof et al., 2004]. These condensations form as a result of thermal instability onset in coronal loops, which leads to catastrophic cooling of the plasma at the loop top. In this sense, the physical reasons behind the formation of prominences and coronal rain are similar, as both are a consequence of thermal instability caused by a localised loop heating. There are a number of parallels between them as both consist of cool plasma at chromospheric

and transition region temperatures. However, there are important differences relating to the morphology of the two phenomena and to the magnetic field geometry associated with them. Prominences are often quasi-stable and supported against gravity by dips in the magnetic field, whereas coronal rain is observed to fall towards the solar surface shortly after its formation. The structure of flows of prominence material appears continuous, while coronal rain structure is more clumpy and consists of a large number of small plasma blobs.

Recent high resolution observations have shown that coronal rain is much more common than previously thought, suggesting its important role in the chromosphere-corona mass cycle. Due to its origin, coronal rain also provides us with physical insight into the atmospheric thermal cycle and into prominence formation and evolution. Small sizes of coronal rain blobs make it a good tracer of coronal magnetic field. In order to understand the formation and evolution of coronal rain, we must first address the conditions leading to thermal instability of coronal loops.

1.3.1 Thermal instability in magnetised plasmas

The issue of the thermal stability of a plasma in the presence of a magnetic field can be studied analytically in the simplified uniform, optically thin case. We introduce a generalised heat loss function $L(\rho_0, T_0)$ defined as the rate of the energy loss minus the energy gain per unit mass, and therefore replacing the $E_{\rm H}$ and $E_{\rm R}$ terms in Eq. (1.7). The stability of the plasma is governed by the sign of the derivative of the heat loss function with respect to entropy of the system S, while a thermodynamic quantity A is held constant. The instability occurs when the derivative is positive:

$$\left(\frac{\partial L}{\partial S}\right)_A > 0\,. \tag{1.53}$$

Assuming ideal gas law, an isochoric perturbation satisfies $T\mathrm{d}S = C_{\rm v}\mathrm{d}T$. Similarly for an isobaric perturbation, $T\mathrm{d}S = C_{\rm p}\mathrm{d}T$. Here C is the specific heat. The corresponding instability criteria in these two cases are therefore

$$\left(\frac{\partial L}{\partial T}\right)_\rho < 0 \tag{1.54}$$

$$\left(\frac{\partial L}{\partial T}\right)_{\rm p} = \left(\frac{\partial L}{\partial T}\right)_\rho - \left(\frac{\partial \rho}{\partial T}\right)_{\rm p}\left(\frac{\partial L}{\partial \rho}\right)_{\rm T} < 0\,. \tag{1.55}$$

In order to derive the conditions for the onset of the thermal instability and the corresponding instability growth rates, we assume homogeneous optically thin plasma

with uniform magnetic field. Following the analysis by Field [1965], we start from a set of MHD equations, given in section 1.2.1. We rewrite Eq. (1.7) using a generalised heat loss function and expanding the thermal conduction term:

$$\frac{1}{(\gamma-1)}\frac{Dp}{Dt}+\frac{\gamma}{\gamma-1}p\vec{\nabla}\cdot\vec{V}=-\rho L+\vec{\nabla}\cdot(\kappa\vec{\nabla}T)\,, \tag{1.56}$$

where κ is the thermal conductivity. As in Section 1.2.2, we linearise the MHD equations by assuming small perturbations of the form $x(\vec{r},t)=x'(nt+i\vec{k}\cdot\vec{r})$:

$$\begin{aligned} n\rho' &= -\rho_0 i\vec{k}\cdot\vec{V}' && (1.57)\\ n\rho_0\vec{V}' &= -i\vec{k}p'+i(\vec{B_0}\cdot\vec{B}')\frac{k}{\mu_0}-ik_\parallel\frac{B_0\vec{B}'}{\mu_0} && (1.58)\\ \frac{n}{(\gamma-1)}p'-\frac{n\gamma p_0}{(\gamma-1)\rho_0}\rho' &= -\rho_0 L_\rho p'-\rho_0 L_{\rm T}T'-(\kappa_\parallel k_\parallel^2+\kappa_\perp k_\perp^2)T' && (1.59)\\ nB' &= -i\vec{B}_0(\vec{k}\cdot\vec{V}')+ik_\parallel B_0\vec{V}\,, && (1.60) \end{aligned}$$

where $L_{\rm T}=(\partial L/\partial T)_\rho$, $L_\rho=(\partial L/\partial\rho)_T$, i.e. the linear terms of the Taylor expansion of the heat loss function near the equilibrium and indices $\parallel$ and $\perp$ correspond to components parallel and perpendicular to the magnetic field respectively. These lead to the characteristic equation for the growth rate n:

$$\begin{aligned} n^5+n^4C_{\rm S}k_{\rm Tc}+n^3k^2(C_{\rm S}^2+a^2)+n^2k^2\Big[\frac{C_{\rm S}^3(k_{\rm Tc}-k_\rho)}{\gamma}+a^2C_{\rm S}k_{\rm Tc})\Big]\\ +nC_{\rm S}^2a^2k^4\cos^2\theta+\frac{(k_{\rm Tc}-k_\rho)C_{\rm S}^3a^2k^4\cos^2\theta}{\gamma}=0\,, \end{aligned} \tag{1.61}$$

where θ is the angle between $\vec{k}$ and $\vec{B}_0$. The instability occurs when the roots corresponding to the growth rate are real and positive. Here we have introduced the wavenumbers

$$k_\rho=\frac{\mu(\gamma-1)\rho_0L_\rho}{RC_{\rm S}T_0}\,,\quad k_{\rm T}=\frac{\mu(\gamma-1)L_{\rm T}}{RC_{\rm S}T_0}\,,\quad k_{\rm K}=\frac{RC_{\rm S}\rho_0}{\mu(\gamma-1)\kappa}\,. \tag{1.62}$$

where k_ρ and $k_{\rm T}$ are sound wave wavenumbers with angular frequencies equal to the growth rates of the isothermal and isochoric perturbations respectively and $1/k_{\rm K}$ is the mean free path of the conducting particles. $k_{\rm Tc}$ corresponds to $k_{\rm T}$ modified by the conduction effects:

$$k_{\rm Tc}=k_{\rm T}+\frac{k_\parallel^2}{k_{\rm K\parallel}}+\frac{k_\perp^2}{k_{\rm K\perp}}=k_{\rm T}+k^2\Big(\frac{\cos^2\theta}{k_{\rm K\parallel}}+\frac{\sin^2\theta}{k_{\rm K\perp}}\Big)\,. \tag{1.63}$$

For the case $k_{\mathrm{Tc}} = k_\rho = 0$, the roots of Eq. (1.63) are 0 for the condensation mode and for the wave modes we get:

$$n_0^2 = \frac{1}{2}k^2\{-C_{\mathrm{S}}^2 - V_{\mathrm{A}}^2 \pm \sqrt{[(C_{\mathrm{S}}^2 + V_{\mathrm{A}}^2)^2 - 4V_{\mathrm{A}}^2 C_{\mathrm{S}}^2 \cos^2\theta]}\}\,, \tag{1.64}$$

where we recovered the result for angular frequencies of the slow and fast magnetoacoustic modes derived in Section 1.2.2. If k_{Tc} are k_ρ small, we use an expansion $n = n_0 + n_1 + ...$ up to the first order in k_{Tc} and k_ρ. When $\theta \neq \pi/2$, the roots of Eq. (1.63) modify such that

$$n_1 = \frac{C_{\mathrm{S}}(k_\rho - k_{\mathrm{Tc}})}{\gamma}\,, \tag{1.65}$$

for the condensation mode and

$$n_1 = \frac{-C_{\mathrm{S}}^3(n_0^2 + V_{\mathrm{A}}^2 k^2\cos^2\theta)[k_\rho + (\gamma-1)k_{\mathrm{Tc}}]}{2\gamma(C_{\mathrm{S}}^2 + V_{\mathrm{A}}^2)[n_0^2 + 2C_{\mathrm{S}}^2 V_{\mathrm{A}}^2 k^2\cos^2\theta/(C_{\mathrm{S}}^2 + V_{\mathrm{A}}^2)]}\,, \tag{1.66}$$

for the wave modes. The requirement for the instability onset in this case matches the isobaric criterion (1.55). Thermal conduction has a stabilising effect on the radiative instability. For wavenumbers larger than a critical wavenumber k_{c} the instability is always suppressed through thermal conduction:

$$k_{\mathrm{c}}(\theta) = \sqrt{\frac{k_{\mathrm{K}}(k_\rho - k_{\mathrm{T}})}{(\cos^2\theta + \sin^2\theta\kappa_\perp/\kappa_\parallel)}}\,. \tag{1.67}$$

In the special case of $\vec{k}$ being perpendicular to the magnetic field, the roots corresponding to the slow mode vanish, and the growth rate of the fast mode reduces to

$$n_1 = \frac{-C_{\mathrm{S}}^3[k_\rho + (\gamma-1)k_{\mathrm{Tc}}]}{2\gamma(C_{\mathrm{S}}^2 + V_{\mathrm{A}}^2)}\,. \tag{1.68}$$

The growth rate of the condensation mode is modified such that

$$n_1 = \frac{C_{\mathrm{S}}(C_{\mathrm{S}}^2 + \gamma V_{\mathrm{A}}^2)[k_\rho/(1 + \gamma V_{\mathrm{A}}^2/C_{\mathrm{S}}^2) - k_{\mathrm{Tc}}]}{\gamma(C_{\mathrm{S}}^2 + V_{\mathrm{A}}^2)}\,. \tag{1.69}$$

The critical wavenumber for the stabilisation by the thermal conduction modifies to

$$k_{\mathrm{c}\perp} = \sqrt{k_{\mathrm{K}\perp}\Big(\frac{k_\rho}{1 + \gamma V_{\mathrm{A}}^2/C_{\mathrm{S}}^2} - k_{\mathrm{T}}\Big)}\,. \tag{1.70}$$

The overall effect of the magnetic field on the condensation mode compared to the purely hydrodynamic case is the inhibition of the instability when $\vec{k}$ is perpendicular to the magnetic field, as the condensation leads to the accumulation of the magnetic pressure in the condensation region. The pressure in the rarefied regions has to be large enough to overcome this. Conversely, if $\vec{k}$ is parallel to the magnetic field, the condensation mode is unaffected.

The stratification of the plasma in the presence of gravity will affect the thermal stability of the plasma. Compared to the case of the uniform medium, where the scale of the temperature variations required to compensate for the density variations to maintain the pressure balance have to be large in order for the growth of the condensation not to be prevented by the thermal conduction, in the stratified case the pressure variations are compensated by gravity and the condensation growth occurs even for small scales.

1.3.2 Thermally unstable coronal loops

As shown in the previous section, the thermal instability in plasma can occur if there is an imbalance between temperature-independent energy gains and temperature-dependent radiative losses. The runway cooling occurs when radiative losses increase with decreasing temperature. All coronal loops are subject to heating, radiative losses and thermal conduction, and in principle there exist stationary solutions where the balance is achieved between all three processes. If however, the thermal conduction is not efficient enough for the heating to balance radiative losses, this leads to loop becoming thermally unstable, as seen in Section 1.3.1. The formation of coronal rain is believed to be linked to rapid cooling of thermally unstable coronal loops which are subject to heating concentrated toward the footpoints [Müller et al., 2003, 2004, 2005]. This footpoint heating leads to uneven temperature profile along the loop length. Chromospheric evaporation and direct injection of plasma into the corona result in high densities near the top of the loop. When the radiation losses near the loop top overcome the heating input, this results in an onset of a thermally unstable regime. A perturbation to the loop such as shock wave can then trigger catastrophic cooling leading to the formation of condensations which subsequently fall down towards the solar surface along the magnetic field lines within the coronal loop (Figure 1.8). This process continues until the heating and cooling regain equilibrium and pressure balance is restored.

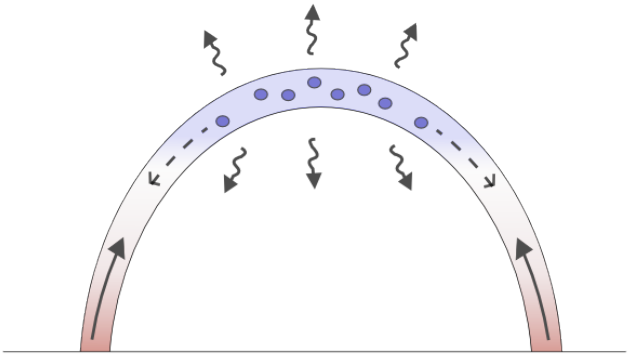

Figure 1.8: Schematic diagram of a thermally unstable loop subject to footpoint-concentrated heating with the radiative losses from the loop top overcoming the heating input leading to the formation of condensations.

Heating function

The nature of the heating of coronal loops determines their stability. Contrary to the traditional scaling laws that assume constant heat deposition along the loop or heating proportional to loop density [e.g., Rosner et al., 1978; Priest, 1978], the observational evidence suggests that the majority of coronal loops are heated predominantly at the footpoints [Aschwanden et al., 2000, 2001]. The energy input is therefore better parametrised as a damped exponential with a short scale height relative to the length of the loop [Serio et al., 1981]:

$$E_{\mathrm{H}} = E_{\mathrm{H0}} \exp(-s/s_{\mathrm{H}}) \,, \tag{1.71}$$

Where E_{H0} is the rate of the energy deposition at the base of the loop, s is the height along the loop and s_{H} is the heating scale-height. If the the heating scale height is shorter that a critical value, the hydrostatic solutions result in a density inversion. The coronal loops with the healing scale height less than $\sim 1/6$ of the length of the loop are therefore dynamically unstable.

Radiative loss function

The exact nature of the radiative losses can in principle be incorporated into the model by solving the MHD equations coupled with equations for radiative trans-

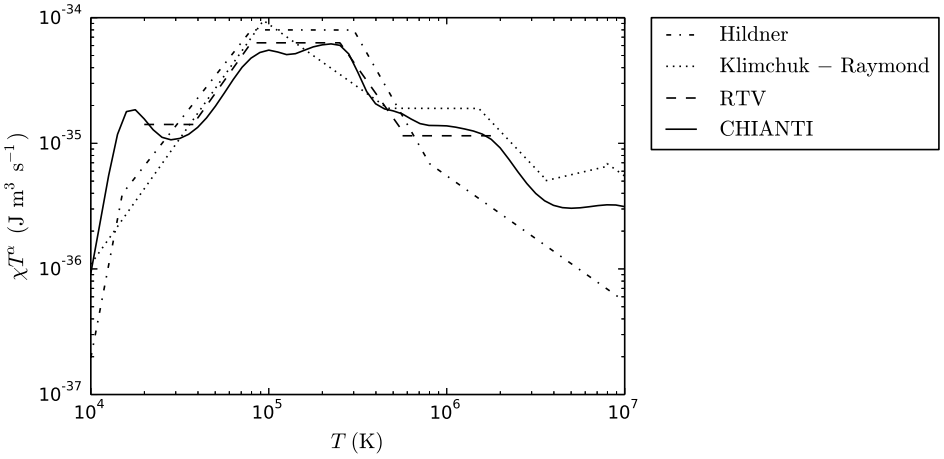

Figure 1.9: Radiative loss functions as a function of temperature calculated by Hildner [1974] (dash-dotted), Rosner et al. [1978] (dashed), Klimchuk and Cargill [2001] (dotted) and determined by using CHIANTI v8.0 (solid).

fer. In practice, this would be too computationally expensive for multidimensional models. Instead, the radiative losses are assumed to be optically thin and due to resonant emission lines and are usually incorporated into MHD models by using a precalculated radiative loss function. The radiative cooling term in the energy equation can then be written as $E_{\rm R} = n_{\rm e}^2 \Lambda(T)$, where $\Lambda(T)$ is the temperature dependent radiative loss function. The standard approach is to use semi-empirical parametrisations of the form $\Lambda(T) = \chi T^{\alpha}$ [e.g., Hildner, 1974; Rosner et al., 1978; Klimchuk and Cargill, 2001], where χ and α are dimensionless fit parameters. The main differences between different models are caused mainly by different assumptions about solar elemental abundances. Currently the most accurate version is calculated based on data for solar elemental abundances from CHIANTI v8.0 atomic database (Figure 1.9).

1.3.3 Coronal rain observations

Despite being first observed more than 40 years ago [Kawaguchi, 1970; Leroy, 1972], coronal rain has not received much attention up until recent years. This was partially due to the lack of instruments with resolution sufficient for detailed observations. Coronal rain was also believed to be a relatively rare phenomenon occurring only sporadically in active regions on the time scales of days [Schrijver, 2001]. Recent work has however shown that coronal rain is in fact much more common than previously thought, typically occurring on the time scales of hours [Antolin et al., 2010;

Antolin and Rouppe van der Voort, 2012]. This short period of a typical heating-condensation cycle, together with the fact that a significant fraction of coronal loops are out of hydrostatic equilibrium constantly undergoing heating and cooling phases [Aschwanden et al., 2001] and hence prone for the condensation to occur suggest that coronal rain may have an important role in the chromosphere-corona mass cycle [Marsch et al., 2008; Berger et al., 2011; McIntosh et al., 2012].

The cooling sequence of the loops predicted by the instability model has been investigated by a number of multi-channel observations. The EUV intensity variations of the active region loops have been analysed using TRACE observations with loop tops brightening first in 195 Å and then in 171 Å channel [Schrijver, 2001] and by combining observations from SOHO/EIT and Big Bear Solar Observatory with coronal rain plasma first showing in 304 Å channel followed by Hα [De Groof et al., 2005]. Sequential brightening and subsequent fading of multiple loop structures has also been observed in soft X-ray and EUV channels using TRACE and SXT [Ugarte-Urra et al., 2006] and Hinode/EIS [Ugarte-Urra et al., 2009], both pointing towards continuous heating and cooling scenario. The cooling sequence has also been observed in loops exhibiting coronal rain [Antolin et al., 2015b]. Such peak intensity variations with time and wavelength are therefore likely to be a signature of the thermal instability in the loops. On larger scale, the occurrence interval of the thermal instability onset leading to formation of the coronal rain in a loop with footpoint-concentrated heating is estimated to be on a time scale of several hours [Antolin and Rouppe van der Voort, 2012]. Similar long term periodic EUV pulsations with periods of several hours were observed in warm active region coronal loops [Auchère et al., 2014; Froment et al., 2015], as well as in prominences [Foullon et al., 2004, 2009]

Coronal rain is usually observed in emission in cool chromospheric lines of both neutral (Hα, Lyα) and ionised atoms (Ca II, He II); or in absorption in EUV [Schrijver, 2001]. The temperatures of the rain plasma range from transition region ($\sim 10^5$ K) to chromospheric ($\sim 10^4$ K). Coronal rain has been detected in the 304 Å channel of SDO/AIA [Kamio et al., 2011] and SOHO/EIT [De Groof et al., 2004, 2005], in the 1600 Å channel of TRACE [Schrijver, 2001], in Ca II H line using Hinode/SOT [Antolin et al., 2010; Antolin and Verwichte, 2011], in Hα by the SST/CRISP [Antolin and Rouppe van der Voort, 2012] and in IRIS FUV and NUV channels [Kleint et al., 2014]. Material resembling coronal rain has also been observed in photospheric wavelengths by SDO/HMI [Martínez Oliveros et al., 2014]. Despite best resolved coronal rain being usually observed off-limb, some on-disk coronal rain events have

also been observed [e.g. Antolin et al., 2012; Antolin and Rouppe van der Voort, 2012]. The coronal rain is observed to form in both active region and post-flare loops [Antolin and Rouppe van der Voort, 2012; Scullion et al., 2016]. The observations also show that the motion of coronal rain blobs is significantly sub-ballistic [e.g. De Groof et al., 2005; Antolin and Verwichte, 2011; Antolin and Rouppe van der Voort, 2012], suggesting that forces other than gravity have an important effect on its dynamics and evolution. High resolution solar observations that became available with the launch of Hinode and later IRIS spacecraft have enabled detailed study of the morphology of the coronal rain. It is typically observed to have a strand-like clumpy structure with the widths of the individual blobs on the order of 100 km [Antolin and Rouppe van der Voort, 2012; Antolin et al., 2015b]. The individual blobs elongate as they fall, often undergoing complex motions. The temperature structure of the individual condensations can be analysed using multi-wavelength observations and suggests that the coronal rain plasma is multithermal [Antolin et al., 2015b].

The small size of coronal rain blobs makes it suitable for tracing the strength and structure of the coronal magnetic field [Antolin and Rouppe van der Voort, 2012]. The degree to which the rain follows the direction of the magnetic field however depends on the strength of the coupling between recombined atoms created during the condensation phase and the local ion population. In the case of the strong coupling, any disturbance of the magnetic field in the loop will be reflected in the motion of the rain blobs. A number of observations have shown presence of transverse MHD waves in the coronal loops [Aschwanden et al., 1999; Nakariakov et al., 1999]. Coronal rain occurring in a loop oscillating transversely will also be subject to transverse oscillatory motion. Such MHD oscillations in coronal rain were first detected by Antolin and Verwichte [2011]. In the case of a non-negligible inertia of the coronal rain blobs, the rain itself is expected to have an effect on the loop oscillations.

1.3.4 Coronal rain simulations

The thermal instability onset and the process of formation and evolution of plasma condensations have been subject to a number of numerical studies. Early numerical studies of thermal instability have shown that the formation of condensations due to radiative losses can occur on realistic timescales comparable to typically observed timescales for prominence formation [Goldsmith, 1971; Hildner, 1974]. Mok et al. [1990] and Antiochos and Klimchuk [1991] included the effect of footpoint-localised heating to form prominence-like condensations at the top of the coronal

loop. Formation of quasi-stable condensations was further addressed by Dahlburg et al. [1998], who in addition to the footpoint-concentrated heating specified the dipped magnetic field geometry as a necessary requirement in order to support the condensation against gravity. Using an improved resolution due to the adaptive grid approach, Antiochos et al. [1999] simulated the complete growth of the condensation and found that it reaches a quasi-steady state after a sufficient amount of time. It was further shown that magnetic dips were in fact not necessary for the condensation formation. The onset of the thermal instability due to localised heating was found to lead to the formation of dynamic condensations even in loops without magnetic dips in the sequence of multiple cycles consisting of the condensation formation, downward drift and subsequent destruction [Karpen et al., 2001]. This particular scenario therefore carries more resemblance to downfalling coronal rain condensations rather than quasi-stable prominence material. The studies of formation of prominence condensations have since evolved through accounting for complex magnetic field geometries [e.g., Karpen et al., 2005, 2006] to multidimensional, fully self-consistent models [Xia et al., 2012]. It has also been shown that the condensation formation seen in the simulations matches the linear instability criteria derived by Parker [1953] and Field [1965] [Xia et al., 2011].

Numerical coronal rain studies were also initially restricted to simplified 1-dimensional cases. One of the first attempts to model the formation of the condensation region and its subsequent evolution was done by Müller et al. [2003, 2004, 2005], indicating that a loop with exponential heating function localised at the footpoints develops a thermal instability followed by catastrophic cooling resulting in a formation of downfalling coronal rain blobs, and that a thermal instability in a loop can occur even using a heating function that is constant in time, as long as it is sufficiently localised. This basic model was further expanded by Antolin et al. [2010] by accounting for variable loop cross-section, impulsive nature of heating and Alfvén wave dissipation near the footpoints. Trains of fast impulsive heating events were also found to result in the runway cooling of the plasma at the loop top [Mendoza-Briceño et al., 2005]. Luna et al. [2012] simulated the evolution of a collection of independent footpoint heated 1D fluxtubes together forming a 3D arcade, observing the formation of both quasi-stable prominence condensation and smaller downfalling coronal rain condensations. The evolution of condensations for the case of fully ionized plasma was further analysed by modelling cool plasma blobs falling along a coronal loop in 1D hydrodynamic simulations [Oliver et al., 2014]. This has shown the blobs falling sub-ballistically, emphasising the role of the pressure effects on the coronal rain dynamics. Froment et al. [2017] has shown 1D simulations of asymmetrically

heated loops exhibiting periodic temperature and density variations related to the periodically repeating cycles of thermal non-equilibria.

It should be noted, however, that 1D hydrodynamic models are equivalent to simulating the evolution along a single magnetic field line and therefore miss a number of transverse effects in coronal loops that could be of interest. In order to study and understand the formation of coronal rain and the effect on the coronal loop in question, multidimensional MHD models are necessary. More recently, the formation process of coronal rain condensations and their evolution was studied by 2.5D MHD simulations [Fang et al., 2013, 2015]. It was found that the siphon flows caused by the pressure differences in the coronal loop can significantly influence the motion of the individual condensations and even counteract the effect of gravity. The whole cycle consisting of heating, resulting chromospheric evaporation, catastrophic cooling of the plasma at the loop top and resulting formation of the condensations, and finally the evacuation of the loop can periodically repeat, as this pattern was seen in both 1D and multidimensional models [Müller et al., 2003, 2004; Fang et al., 2015; Froment et al., 2017]. This is known as the limit cycle of loop evolution and has also been discussed in observational studies [Antolin and Rouppe van der Voort, 2012].

1.4 Waves in the solar corona

The solar corona supports a variety of waves. Large scale energy releases in the corona occurring during energetic events can trigger global propagating waves, also known as EIT or global EUV waves and their chromospheric counterpart known as Moreton waves [e.g. Moreton and Ramsey, 1960; Thompson et al., 1998; Ballai et al., 2005]. These originate from the source of solar eruption, rapidly propagate across the solar disc and often interact with coronal structures. Compressible waves were observed in solar plumes [Ofman et al., 1997, 1999; DeForest and Gurman, 1998]. Coronal loops are also subject to a variety of oscillations, including standing fast kink modes [Aschwanden et al., 1999; Nakariakov et al., 1999], standing slow magnetoacoustic modes [Kliem et al., 2002; Wang et al., 2002] as well as propagating slow modes [De Moortel et al., 2000; Robbrecht et al., 2001]. Transverse and longitudinal oscillations are often observed in prominence threads [e.g. Jing et al., 2003; Okamoto et al., 2007; Zhang et al., 2012; Luna et al., 2014]. Short period transverse oscillations were also detected in spicules [De Pontieu et al., 2007; He et al., 2009; Jess et al., 2012].

High resolution observations of oscillations in the corona are exploited by the coronal seismology [Nakariakov and Verwichte, 2005; Ruderman and Erdélyi, 2009; Andries et al., 2009; De Moortel and Nakariakov, 2012]. Coronal seismology is based on using the properties of the observed oscillations such as the amplitude, period and damping rate to deduce information about physical parameters of the coronal plasma including temperature, density stratification, magnetic field strength or energy transport coefficients.

1.4.1 Alfvén waves

Alfvén waves in the solar corona have long been subject of great interest, as they are the prime candidates for the energy transport from the sub-photospheric regions to the corona responsible for the coronal heating. They are not affected by reflection due to atmospheric stratification [Ofman, 2002]. Alfvén, or torsional modes present in a flux tube are incompressible and do not perturb the flux tube density. There is therefore no associated change in the plasma emission. The only observational signature of a torsional mode is a Doppler shift present in spectral data indicative of line-of-sight motion, resolvable only in long period cases. In short period cases (i.e. on the order of minutes), the torsional motions can be observed only indirectly via non-thermal line broadening. This is caused by the non-resolved motions of the plasma in the direction perpendicular to the axis of the flux tube. As the torsional motion occurs in both directions along the line-of-sight, it results in both red and blue shift simultaneously, leading to the broadening of emission lines. A number of recent studies reported observations indicative of such line broadening. These include periodic broadening of Hα line observed in a chromospheric bright point by SST [Jess et al., 2009], observations of increase in width Fe XII and Fe XIII lines in a polar region using Hinode/EIS observations that agree with scenario corresponding to propagating torsional waves with growing amplitude [Banerjee et al., 2009] and observations of growing line broadening in a polar coronal hole using SOHO/SUMER and Hinode/EIS observations corresponding to growing propagating disturbances that are either transverse or torsional in nature [Gupta et al., 2010]. Non-thermal line broadening can be however also caused by a number of other processes including turbulence, unresolved fine structure and magnetoacoustic modes, care is therefore needed when interpreting such observations. Direct observational evidence of torsional Alfvén waves in the corona is still missing.

1.4.2 Magnetoacoustic waves in coronal loops

As derived in Section 1.2.2, there are two classes of magnetoacoustic waves that can occur in a magnetic flux tube such as coronal loop - fast and slow modes. Both types can occur as either standing or propagating waves. Standing magnetoacoustic slow modes correspond to compressive longitudinal oscillations of the coronal loop. They are usually detected through Doppler shifts that suggest periodic line-of-sight motion along the axis of the coronal loop. They were first observed as periodic oscillations in the intensity and Doppler shift of the coronal Fe XIX and Fe XXI lines in the SOHO/SUMER observations with typical periods of 7 - 31 min and typical amplitudes of 50 - 100 $\mathrm{km\,s^{-1}}$ [Kliem et al., 2002; Wang et al., 2002]. Rapid increase in the line intensities and large Doppler shift typically observed in the initial stages of the oscillations suggest they are excited impulsively [Wang et al., 2003a]. They are often excited during small flaring events, which suggests that they are a natural response of the coronal loop to impulsive heating in the non-eruptive case when there is magnetic restructuring of the flaring loop. They are usually subject to strong damping more pronounced in loops with low density [Wang et al., 2003a,b; Pandey and Dwivedi, 2006; Wang et al., 2007], reasons for which are still not fully understood.

Propagating slow magnetoacoustic modes are typically seen as small amplitude intensity enhancements propagating upwards along the legs of coronal loops [e.g. De Moortel et al., 2000; Robbrecht et al., 2001; De Moortel et al., 2002a,b]. Their periods typically range from few to several minutes and their apparent speeds are lower than the sound speed in the local plasma. They are subject to damping which is caused by the dissipative processes such as thermal conduction and viscosity [Nakariakov et al., 2000]. They are sometimes observed to be reflected at the foot points traversing the loop multiple times before eventually fading [Kumar et al., 2013; Mandal et al., 2016]. A number of observations suggests existence of propagating slow waves in the lower corona with 3 and 5 min periods [De Moortel et al., 2002b; Marsh et al., 2003; Wang et al., 2009]. It has been suggested that their origin is connected to the global photospheric p-mode leakage [De Pontieu et al., 2005].

Fast sausage modes correspond to the axisymmetric variation of the loop cross-section resulting in contractions and widenings of the loop and therefore cause variations of the plasma density. The plasma flows occur mainly in the radial direction. This, together with the fact that the typical intensity variation due to density per-

turbation is of the order of few percent means that sausage modes are difficult to observe directly. Typical periods are in the range $5 - 30$ s, observations of sausage modes are therefore only possible using high cadence data. Sausage modes are usually observed in EUV and soft X-ray wavelengths as periodic variations of the intensity and non-thermal line broadening due to radial motion of the loop plasma. In flaring loops the sausage mode can be detected by observing the modulation of the microwave emission of the loop due to varying magnitude of magnetic field. It also modulates the population of non-thermal electrons by changing the magnetic mirror ratio in the legs of the flaring loops, which causes periodic increase and decrease of the precipitation of electrons. This leads to the modulation of the footpoint emission in white light and hard X-rays because of Bremsstrahlung [Zaitsev and Stepanov, 1982]. Spatially resolved sausage mode was first observed in a flaring loop in microwave band of Nobeyama Radioheliograph [Nakariakov et al., 2003; Melnikov et al., 2005]. Phase and group speeds of the mode depend strongly on the mode wave number. Long wavelength sausage modes are subject to cut-off, with the cut-off wavelength dependent on the density contrast between the loop and the background plasma. Sausage modes with large wave number are trapped in the loop. For wave numbers less than the cut-off the sausage mode becomes leaky and the mode energy is radiated into the external medium. In practice this means that the majority of loops are able to support only high-order harmonics. Fundamental sausage mode can only be sustained in a loop that is sufficiently thick and dense, which is most likely to be the case in flaring loops. Despite the difficulties associated with direct observations of sausage modes, they have useful seismological applications and the observed oscillation parameters can be used for determination of the magnetic field strength in the loop or to infer the density contrast between the loop and the surrounding corona.

The fast kink, or transverse, oscillations of the coronal loops correspond to the perpendicular displacement of the loop axis with all parts of the loop moving in phase. They were first observed by TRACE [Aschwanden et al., 1999; Nakariakov et al., 1999] and were identified as a fundamental harmonic of the fast magnetoacoustic kink mode. This particular event consisted of large bundle of loops undergoing large-amplitude damped transverse oscillations with period of ~ 260 s and damping time of ~ 900 s excited by a blast wave resulting from a nearby flare.

Since the first observational evidence, multiple regimes of transverse oscillations have been detected, ranging from periods on the order of seconds [e.g. Williams et al., 2001] to hours [e.g. Verwichte et al., 2010; Hershaw et al., 2011]. Both standing

[Nakariakov et al., 1999; White and Verwichte, 2012] and travelling kink oscillations [Williams et al., 2001; Tomczyk et al., 2007; McIntosh et al., 2011] are observed. They can be excited by a flare or other energetic event and subject to rapid damping [White and Verwichte, 2012; White et al., 2012; Nisticò et al., 2013], or persistent and decayless, driven by a continuous process [Wang et al., 2012; Nisticò et al., 2013; Anfinogentov et al., 2013]. The transverse oscillations are observed in horizontal polarisation where the loop displacement is perpendicular to the plane of the loop [Aschwanden et al., 1999; Nakariakov et al., 1999]; or in vertical polarisation, with the loop displacement occurring in the plane of the loop [Wang and Solanki, 2004]. Excitation of higher order harmonics of a fast kink mode has been observed [Verwichte et al., 2004; De Moortel and Brady, 2007; Van Doorsselaere et al., 2007]. This is likely to occur if the loop is hit off-centre by a flare-induced blast wave [De Moortel and Brady, 2007] or if the oscillation excitation mechanism is associated with the reconnection process [White et al., 2012]. Multiple harmonics were also observed to be present in a single coronal loop [Verwichte et al., 2004; Van Doorsselaere et al., 2007, 2009]. Observations of multimode loop oscillations are valuable from the seismological point of view, as the ratio of the fundamental period to twice the period of the second harmonic P_1/P_2 can be used as a diagnostic tool, given that the density stratification causes it to diverge from unity [Andries et al., 2005a; McEwan et al., 2006]. It can therefore be used for deducing information about the longitudinal density structure of the coronal loop.

Including the effect of the energy transport within the coronal loop can have an effect on the properties of the fundamental harmonic of the fast kink mode. The transverse oscillations of radiatively cooling coronal loops were studied by Morton and Erdélyi [2009], Ruderman [2011] and Magyar et al. [2015]. The decrease of temperature at the loop top due to the radiative cooling was found to lead to a gradual flow of plasma towards the loop footpoints as a result of the decrease in the stratification scale height. This results in the redistribution of the plasma along the length of the loop. Such changes in the loop density profile lead to change of the period of the fundamental harmonic of the loop during the cooling process.

The damping of the transverse loop oscillations occurs on the time scales of few oscillation periods and is thought to be caused by resonant absorption [Hollweg and Yang, 1988; Ruderman and Roberts, 2002; Goossens et al., 2002, 2010; Okamoto et al., 2015; Antolin et al., 2015a] and subsequent phase mixing [Heyvaerts and Priest, 1983; De Moortel et al., 1999]. The resonant absorption corresponds to the transfer of kink mode energy into localised azimuthal Alfén oscillations and occurs

in a magnetised cylinder with a non-homogeneous boundary layer, where the density varies between the internal (i.e. density of the loop plasma) and external value (i.e. density of the background medium). The sharp change of the plasma density at the boundary leads to mode conversion of global fast kink modes to the local Alfvén modes when the frequency of the kink mode matches with local Alfvén frequency. Local Alfvén waves are subsequently dissipated through phase mixing. The phase mixing corresponds to the energy dissipation in an inhomogeneous medium and is linked to the variation of the Alfvén speed in neighbouring field lines due to the spatial variation of quantities such as plasma density and temperature. This results in the Alfvén waves on different field lines propagating at different speeds and becoming increasingly out of phase, leading to large gradients in the direction perpendicular to the magnetic fields and hence to enhanced dissipation. The decay rate of the global oscillation due to resonant absorption is given by [Ruderman and Roberts, 2002]:

$$\frac{\tau_{\rm d}}{P} = \frac{2}{\pi}\frac{a}{l}\frac{\rho_{\rm i}+\rho_{\rm e}}{\rho_{\rm i}-\rho_{\rm e}}\,, \tag{1.72}$$

where a is the diameter of the cylinder, l is the width of the inhomogeneous boundary layer, P is the oscillation period and the constant (in this case $2/\pi$) depends on the shape of the transition layer. However, due to large uncertainties associated with the determination of the densities of coronal plasma, comparison with the observed decay rates is difficult.

1.5 Interplay of MHD oscillations and coronal rain

Strong coupling between the recombined atoms created during the condensation phase and the local ion population means that the motion of the coronal loop including transverse loop oscillations are traced by the individual coronal rain blobs [Antolin and Verwichte, 2011]. The coronal rain therefore has important seismological potential, especially when using high resolution observations in chromospheric and transition region temperatures that are otherwise insensitive to the coronal temperature plasma.

The transverse oscillatory motion of the coronal loop triggers an action of a ponderomotive force (PMF); a non-linear component of the Lorentz force acting along the direction of the magnetic field, directed towards the locations of the maximum oscillation amplitude that results from a transverse perturbation of the magnetic field. The problem can be addressed using the perturbation approach similarly as

in the previous sections, but this time expanding the physical quantities up to the second order and considering 1D case for simplicity [Rankin et al., 1994]. Here it should be pointed out that the solution for the standing Alfvén wave in the 1D case is equivalent to the solution for the standing transverse wave in the 2D case with the wave vector parallel to the magnetic field. The resulting individual components of the ponderomotive force are second-order in the perturbed quantities. In the $\beta << 1$ case, the second order driven perturbations in the density ρ'' and velocity along the magnetic field V_z'' satisfy

$$\frac{\partial V_z''}{\partial t} = \frac{C_S^2}{\rho_0}\frac{\partial \rho''}{\partial z} - \frac{1}{2\rho_0}\frac{\partial B_y'^2}{\partial z} \tag{1.73}$$

$$\frac{\partial \rho''}{\partial t} = -\rho_0 \frac{\partial V_z''}{\partial z}\,. \tag{1.74}$$

The PMF effect on the velocity of the plasma along the equilibrium magnetic field can then be determined by substituting the oscillatory solution for B_y' of the form $-V_0/V_A B_0 \sin(\omega t)\sin(k_z z)$ corresponding to the standing Alfén wave. This subsequently results in a density perturbation ρ'' given by

$$\frac{\rho''}{\rho_0} = \frac{1}{2}\Big(\frac{V_0}{V_A}\Big)^2\Big(\frac{\omega}{\omega_s}\Big)^2[1-\cos(\omega_s t)]\cos(2k_z z)\,, \tag{1.75}$$

where $\omega_s = 2k_z C_S$ is the period of the PMF-induced density variation and V_0 is the velocity amplitude of the oscillation. As the wavelength of the density perturbation is a half of the wavelength of the standing wave, the accumulation of mass occurs at the location of the maximum oscillation amplitude. We should note that here the zero-β approximation breaks down, as neglecting the effect of the plasma pressure leads to Eq. (1.75) becoming secular in time [Verwichte et al., 1999].

It has been shown that the ponderomotive force resulting from loop oscillations can cause large scale flows of plasma in the loop and create density enhancements in the antinodes of the oscillation [Terradas and Ofman, 2004]. For the case corresponding to the fundamental harmonic of the kink mode of the loop, this leads to the accumulation of the mass at the loop top, creating a non-hydrostatic density profile along the loop. The flows triggered by non-linear effects can in principle affect the motion and evolution of the individual condensations. Analytical results however suggest that for realistic loop oscillation amplitudes the effect of ponderomotive force is not strong enough to have significant effect on the motion of the coronal rain compared to other factors such as pressure effects that are present regardless of whether the loop is oscillating or not [Verwichte et al., 2017a].

The finite mass of the coronal rain blobs can also trigger oscillations, due to deformation of the loop axis by the massive condensations which is then restored through the action of the magnetic tension force leading to the transverse oscillatory motion of the loop and due to the centrifugal force that results from the downfalling rain blobs moving under the influence of gravity along a semicircular loop leading to outward displacement of the coronal loop axis. However, in order for the latter to have an observable effect, high speeds of the moving condensations are required, of the order of $\sqrt{g_\odot R} \sim 100\,\mathrm{km\,s^{-1}}$ [Verwichte et al., 2017b]. These can in principle be achieved e.g. in the presence of a background siphon flow in the coronal loop.

1.6 Observations

The solar atmosphere has been subject to observations for hundreds of years. Modern era solar observations are done by a variety of ground-based and space-based observatories. The largest ground-based solar observatories such as Big Bear Solar Observatory, Swedish 1-m Solar Telescope and Daniel K. Inouye Solar Telescope (currently under construction and to be completed in 2019) use large-aperture vacuum telescopes and are typically located at high altitudes to reduce effects of atmospheric seeing. Their main advantage is their cost-effectiveness, ability to use large diameter optics, long lifetime and easy maintenance. The ground-based observations are however limited by the Earth's atmosphere and their spatial resolution is affected by seeing. This effect can be partially reduced by using adaptive optics. The spacecraft missions on the other hand benefit from not being affected by the Earth's atmosphere, which means that it is possible to achieve higher resolution as well to observe the Sun in wavelengths that are normally blocked by the atmosphere, such as many FUV/EUV emission lines essential for observing the plasma at transition region and coronal temperatures. High resolution observations from recent solar missions have unveiled a dynamic nature of the solar corona and enabled us to study the coronal activity in unprecedented detail. For full understanding of the properties of thermally unstable coronal loops and of the formation and evolution of the coronal rain we require observations in both hot coronal wavelengths providing information about the unstable coronal loop before and after the catastrophic cooling occurs, as well as cool chromospheric and transition region lines necessary for observing the cool condensation plasma. Coordinated observations by different space-based and ground-based instruments combined to provide imaging and spectral data as well as coverage across a broad range of wavelengths are therefore

necessary to fully exploit the capabilities of the solar observatories for the study of coronal rain.

1.6.1 Solar Dynamics Observatory

The Solar Dynamics Observatory (SDO) is a space-based observatory designed to provide continuous observations of the full solar disk and was launched in February 2010. The instrument payload onboard SDO consists of Atmospheric Imaging Assembly (AIA) [Lemen et al., 2012], Extreme Ultraviolet Variability Experiment (EVE) [Woods et al., 2012] and Helioseismic and Magnetic Imager (HMI) [Scherrer et al., 2012]. AIA provides imaging data in 7 EUV bandpasses with 1.5″ spatial resolution and 12 s cadence. The bandpasses are centered on coronal and transition region emission lines: Fe XVIII (94 Å), Fe VIII, XXI (131 Å), Fe IX (171 Å), Fe XII, XXIV (193 Å), Fe XIV (211 Å), He II (304 Å), and Fe XVI (335 Å). The transmission functions for each bandpass are shown in Figure 1.10. EVE measures the solar EUV spectral irradiance in order to investigate short and long term solar irradiance variability. HMI provides magnetograms for full solar disk. Main advantage of using SDO observations for studies of thermal instability and coronal rain is getting continuous imaging data at multiple wavelengths enabling us to investigate the thermal evolution of the region of interest. The low AIA resolution (compared to other missions) is however a limiting factor for coronal rain observations and prevents an in-depth analysis of detailed structure, morphology and evolution of the individual condensations. Hence, SDO/AIA is useful for studying the heating and condensation phase of the coronal loop thermal cycle, but not the evacuation phase, during which the condensation plasma becomes too cool and the scale of the individual condensations becomes too small to be detected by AIA.

1.6.2 Interface Region Imaging Spectrograph

Interface Region Imaging Spectrograph (IRIS) [De Pontieu et al., 2014] is a spacecraft mission launched in June 2013. Its main aim is to study mass and energy flow in the chromosphere and transition region. It provides spectral and imaging data with maximum field of view of 175″ × 175″, 0.33″ - 0.4″ spatial resolution and 2 s maximum cadence. The imaging data is provided by slit-jaw imager in 4 passbands centered on 2 transition region lines (C II 1335 Å and Si IV 1400 Å), one chromospheric line (Mg II k 2796 Å) and one photospheric wavelength (2830 Å). The spectral data is provided using a spectrograph covering 2 FUV passbands

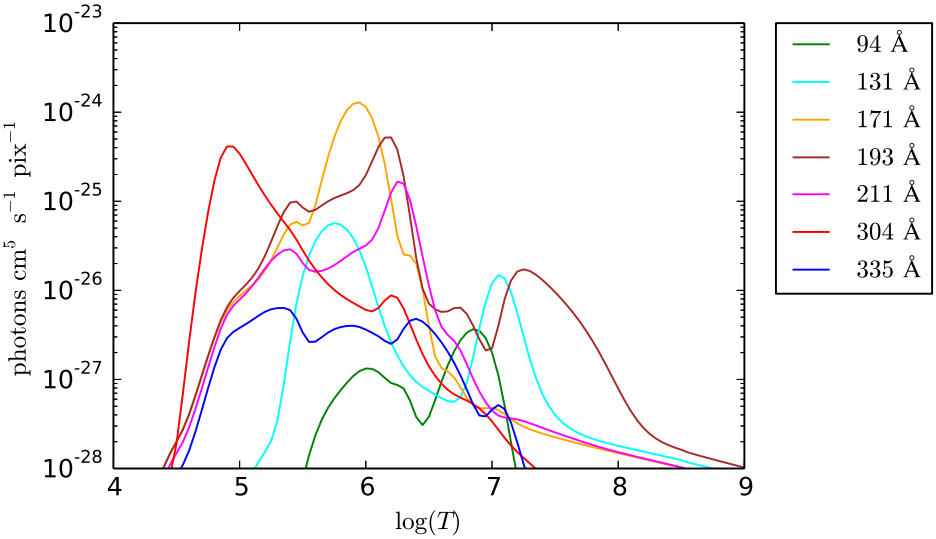

Figure 1.10: Transmission functions for each AIA bandpass.

(1332 Å - 1358 Å and 1389 Å - 1407 Å) and one NUV passband (2783 Å - 2835 Å) with the possibility of multiple rastering modes scanning over the region of interest. These range from sit-and-stare (fixed slit, no rastering) modes, dense rasters (providing high spatial resolution) to coarse rasters (allowing rapid scans of large regions). Sensitivity to plasma at chromospheric and transition region temperatures makes IRIS suitable for coronal rain observations, while the high spatial resolution enables detailed study of the coronal rain structure and evolution. High temporal cadence of the data is crucial for in-depth studies of waves and oscillations.

1.6.3 Hinode

Hinode [Kosugi et al., 2007] is a spacecraft in sun-synchronous polar orbit and was launched in September 2007. Its main objective is to study solar magnetic field generation, transport and dissipation. Its instrumental payload consists of three instrument suites: Solar Optical Telescope (SOT) [Tsuneta et al., 2008], X-ray Telescope (XRT) [Golub et al., 2007] and EUV Imaging Spectrometer (EIS) [Culhane et al., 2007]. SOT contains Optical Telescope Assembly, a 50 cm Gregorian telescope and a Focal Plane Package. Focal Plane Package consists of narrowband and broadband filtergraphs providing intensity, Doppler shift and polarimetric imaging and a Stokes Spectropolarimeter, which provides line profiles in all Stokes parameters. XRT is a 30 cm grazing incidence telescope and provides X-ray images in 9 bandpasses with

$34' \times 34'$ field of view, i.e. covering the full solar disk and $1''$ maximum spatial resolution. EIS provides spectral data in 170 Å - 211 Å and 246 Å - 292 Å wavelength bands with $2''$ maximum spatial resolution. SOT observations are particularly suitable for coronal rain analysis due to their $0.2''$ resolution, large $218'' \times 109''$ field of view, high cadence and sensitivity to cool chromospheric lines, such as Ca II H.

1.7 Simulations - Lare2d

In order to solve a nonlinear set of MHD equations, a fully numerical approach must be used. This work uses Lare2d [Arber et al., 2001], a Lagrangian remap code that solves the full set of MHD equations on a staggered Cartesian grid. The code is second order accurate in space and time and uses shock viscosity and gradient limiters to handle shock problems. It also includes effects of gravity, thermal conduction and radiative losses making it well suited for studying the formation and evolution of plasma condensations in coronal environment.

The standard resistive MHD equations solved by Lare2d are of the form:

$$\frac{\partial \rho}{\partial t} = -\vec{\nabla} \cdot (\rho \vec{V}) \tag{1.76}$$

$$\frac{\mathrm{D}\vec{V}}{\mathrm{D}t} = \frac{1}{\rho}\vec{j} \times \vec{B} - \frac{1}{\rho}\vec{\nabla} p \tag{1.77}$$

$$\frac{\partial \vec{B}}{\partial t} = -\vec{\nabla} \times \vec{E} \tag{1.78}$$

$$\frac{\mathrm{D}\epsilon}{\mathrm{D}t} = -\frac{P}{\rho}\vec{\nabla} \cdot \vec{V} + \frac{\eta}{\rho} j^2 \tag{1.79}$$

$$\vec{E} + \vec{V} \times \vec{B} = \eta \vec{j} \tag{1.80}$$

$$\vec{\nabla} \times \vec{B} = \mu_0 \vec{j}\,. \tag{1.81}$$

Pressure and temperature are given in terms of the specific internal energy density ϵ:

$$p = \frac{\rho k_B T}{\mu_m}$$
$$\epsilon = \frac{p}{\rho(\gamma - 1)}\,,$$

where μ_m is the reduced mass.

The equations are solved in normalised form. The physical variables are related

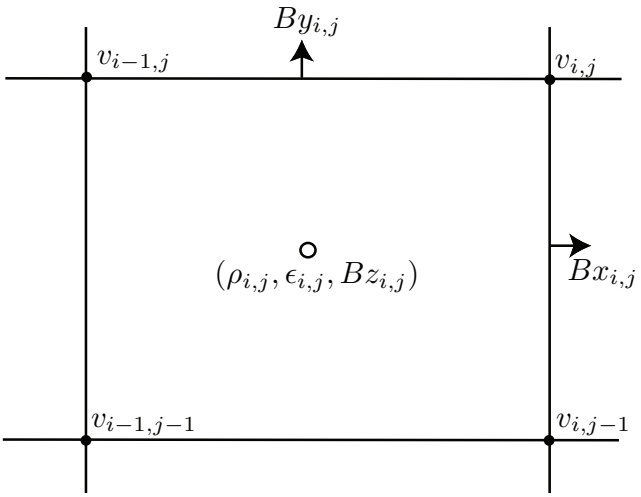

Figure 1.11: The staggered grid used by Lare2d.

to the dimensionless variables via user defined normalising constants L_0, ρ_0 and B_0, such that $x = L_0\tilde{x}$, $\rho = \rho_0\tilde{\rho}$ and $\vec{B} = B_0\tilde{\vec{B}}$, where $\tilde{x}$, $\tilde{\rho}$ and $\tilde{\vec{B}}$ are normalised quantities. The normalising constants for all other quantities can expressed in terms of L_0, ρ_0 and B_0.

Each timestep consists of a Lagrangian step and a remap step. During the Lagrangian step the above equations are solved in the Lagrangian frame (where grid moves with the fluid) using a second order accurate predictor-corrector scheme. This approach means it is straightforward to add additional terms into the MHD equations. During the remap step the solution is conservatively remapped onto the original Eulerian grid, while applying van Leer gradient limiters to ensure correct treatment of shocks.

Lare2d is essentially a 2.5D code, given that all vector variables have 3 components, but the equations are solved on a 2-dimensional grid, assuming no variation in the 3rd dimension. The grid is staggered to prevent the development of the checkerboard instability. The velocities are defined at cell corners, scalar quantities and B_z magnetic field component are defined at cell centres. B_x and B_y magnetic field components are defined at cell edges (Figure 1.11).

Thermal conduction used in the code is based on the Braginskii thermal conduction and is given by

$$\frac{\partial \epsilon}{\partial t} = \vec{\nabla}.\left(\left(\kappa \frac{\vec{B}}{B^2 + b_{\min}^2}.\vec{\nabla}T\right)\vec{B}\right) + \vec{\nabla}.\left(\kappa \frac{b_{\min}^2}{B^2 + b_{\min}^2}\vec{\nabla}T\right), \qquad (1.82)$$

where thermal conductivity $\kappa = \kappa_0 T^{\frac{5}{2}}$. Finite parameter $b_{\min}$ is used to make the thermal conduction isotropic in the absence of magnetic field. If sufficient heating occurs, the heat flux can exceed the free streaming heat flux $q_{\rm f} = v_{\rm th} k_{\rm B} T$, where v_{th} is the electron thermal velocity. In this case the heat flux is limited to $F_{\rm L} v_{\rm th} k_{\rm B} T$ with $F_{\rm L}$ being the flux limiter typically set to 0.05. The thermal conduction is treated using super time stepping methods. Super time stepping is an approach used to accelerate explicit time-stepping schemes by speeding up integration of parabolic operators [Meyer et al., 2012, 2014].

Lare2d also contains a user specified heating function that enables input of heating anywhere in the simulation domain. Optically thin radiative losses are calculated using the exact integration method by Townsend [2009] and are modelled by RTV radiative loss function. The exact integration method is based on integrating the cooling equation exactly rather than using an explicit finite difference scheme. The cooling equation can be written as

$$\frac{dT}{dt} = -\frac{(\gamma - 1)\bar{m} n_{\rm e} n_{\rm H} \Lambda(T)}{\rho k_{\rm B}}\,, \tag{1.83}$$

where $\Lambda(T)$ is the radiative loss function. Explicit schemes are based on solving fully discrete form of the cooling equation with the radiative loss function evaluated at the initial temperature T_i^n:

$$\frac{T_i^{n+1} - T_i^n}{\Delta t} = -\frac{(\gamma - 1)\bar{m} n_{\rm e} n_{\rm H} \Lambda(T_i^n)}{\rho_i k_{\rm B}}\,. \tag{1.84}$$

The updated temperature is then given by

$$T_i^{n+1} = T_i^n \left[1 - \frac{\Delta t}{t_{\rm cool}}\right], \tag{1.85}$$

where $t_{\rm cool}$ is the single point cooling time given by

$$t_{\rm cool} = \frac{2\bar{m} k_{\rm B} T_i^n}{(\gamma - 1)\rho_i \Lambda(T_i^n)}\,. \tag{1.86}$$

The main issue associated with use of explicit finite difference scheme is that solutions significantly depart from the exact values when the timestep Δt is comparable or larger than $t_{\rm cool}$, due to using the initial value of the radiative loss function which is not adjusted in response to the cooling process. This can be overcome by solving

Table 1.1: RTV radiative loss function coefficients

T(K)	$\log_{10}(\chi)$	α
$2 \times 10^4 - 3.98 \times 10^4$	-34.85	0
$3.98 \times 10^4 - 7.94 \times 10^4$	-44.0	2
$7.94 \times 10^4 - 2.51 \times 10^5$	-34.2	0
$2.51 \times 10^5 - 5.62 \times 10^5$	-23.4	-2
$5.62 \times 10^5 - 1.995 \times 10^6$	-34.94	0
$1.995 \times 10^6 - 1 \times 10^7$	-30.73	-2/3

the semi-discrete cooling equation exactly; rearranging it as

$$\frac{dT}{\Lambda(T_i)} = -\frac{(\gamma-1)\bar{m}n_{\rm e}n_{\rm H}}{\rho_i k_{\rm B}}dt\,, \tag{1.87}$$

and integrating across the timestep

$$\int_{T_i^n}^{T_i^{n+1}} \frac{dT}{\Lambda(T_i)} = -\frac{(\gamma-1)\bar{m}n_{\rm e}n_{\rm H}}{\rho_i k_{\rm B}}dt\,. \tag{1.88}$$

The integral can be evaluated by introducing a dimensionless temperature evolution function $Y(T)$ given by:

$$Y(T) = \frac{\Lambda(T_{\rm ref})}{T_{\rm ref}} \int_T^{T_{\rm ref}} \frac{dT'}{\Lambda(T')}\,, \tag{1.89}$$

where $T_{\rm ref}$ is an arbitrary reference temperature. Substituting this into Eq. (1.88) leads to

$$\frac{T_{\rm ref}}{T_i^n}\frac{\Lambda T_i^n}{\Lambda(T_{\rm ref})}[Y(T_i^n) - Y(T_i^{n+1})] = -\frac{\Delta t}{t_{\rm cool}}\,. \tag{1.90}$$

The updated temperature is then given by

$$T_i^{n+1} = Y^{-1}\left[Y(T_i^n) + \frac{T_i^n}{T_{\rm ref}}\frac{\Lambda(T_{\rm ref})}{\Lambda(T_i^n)}\frac{\Delta t}{t_{\rm cool}}\right]. \tag{1.91}$$

The form of the temperature evolution function depends on the functional form of the radiative loss function. We assume RTV radiative losses based on piecewise power law parametrisation [Rosner et al., 1978] given by

$$\Lambda(T) = \chi_k T^{\alpha_k} \qquad T_k \le T < T_{k+1} \tag{1.92}$$

where α_k and χ_k are coefficients given in Table 1.1 for $N-1$ temperature intervals.

T_N is chosen as the reference temperature. $Y(T)$ is given by

$$Y(T) = Y_k + \begin{cases} \frac{1}{1-\alpha_k}\frac{\Lambda_N}{\Lambda_k}\frac{T_k}{T_N}\Big[1 - \big(\frac{T_k}{T}\big)^{\alpha_k - 1}\Big] & \alpha_k \neq 1 \\ \frac{\Lambda_N}{\Lambda_k}\frac{T_k}{T_N}\ln\big(\frac{T_k}{T}\big) & \alpha_k = 1 \end{cases} , \tag{1.93}$$

where $\Lambda_k = \chi_k T_k^{\alpha_k}$, $\Lambda_N = \Lambda_{N-1}(T_N/T_{N-1})^{\alpha_{N-1}}$ and Y_k is the integration constant ensuring the continuity of $Y(T)$ that can be determined from

$$Y_k = Y_{k+1} - \begin{cases} \frac{1}{1-\alpha_k}\frac{\Lambda_N}{\Lambda_k}\frac{T_k}{T_N}\Big[1 - \big(\frac{T_k}{T_{k+1}}\big)^{\alpha_k - 1}\Big] & \alpha_k \neq 1 \\ \frac{\Lambda_N}{\Lambda_k}\frac{T_k}{T_N}\ln\big(\frac{T_k}{T_{k+1}}\big) & \alpha_k = 1 \end{cases} , \tag{1.94}$$

given that $Y_N = Y(T_{\rm ref}) = 0$. The inverse of the temperature evolution function is then given by

$$Y^{-1}(Y) = \begin{cases} T_k\Big[1 - (1-\alpha_k)\frac{\Lambda_k}{\Lambda_N}\frac{T_N}{T_k}(Y - Y_k)\Big]^{1/1-\alpha_k} & \alpha_k \neq 1 \\ T_k \exp\Big[-\frac{\Lambda_k}{\Lambda_N}\frac{T_N}{T_k}(Y - Y_k)\Big] & \alpha_k = 1 \end{cases} \qquad Y_k \leq Y < Y_{k+1}\,. \tag{1.95}$$

Chapter 2

Analysis of coronal rain observed by IRIS, Hinode/SOT AND SDO/AIA: transverse oscillations, kinematics and thermal evolution

Contents of this chapter have been published in Kohutova and Verwichte [2016].

2.1 Introduction

The resolution and cadence of solar observations from currently operational space-based instruments enables detailed analysis of coronal rain properties and evolution. This includes the detection of small amplitude oscillations with amplitudes of few hundred km, analysis of the fine-scale structure of the condensations down to length scales of 100 km and precise analysis of the condensation dynamics, with most of the uncertainties in the speeds and accelerations of the condensations coming from projection effects rather than from the limitations of the instruments. High resolution observations are particularly useful for precise determination of MHD oscillation parameters. MHD oscillations in coronal rain have coronal seismological potential and can be a source of information about coronal loop properties and magnetic field structure in the loop. They can also help to quantify the effect of the plasma con-

densations on the coronal loop and can affect dynamics of the coronal rain through a ponderomotive force exerted on the falling blobs. This highlights the importance of addressing the interplay between the coronal rain and MHD waves in order to better understand the coronal loop structure, evolution and energy transport mechanisms. Coordinating observations between different instruments provides the possibility for simultaneous observations in a range of wavelengths covering temperatures ranging from chromospheric to coronal, giving us a better picture of the thermal structure and evolution of coronal loops subject to catastrophic cooling.

This chapter covers analysis of a coronal rain event observed simultaneously by IRIS, Hinode/SOT and SDO/AIA. It is the first study of a coronal rain event covering analysis of transverse oscillations of the studied coronal loop traced by coronal rain, kinematics of the individual coronal rain condensations and the thermal evolution of the coronal loop plasma at the same time. Transverse oscillations in coronal rain were first observed in Hinode/SOT data by Antolin and Verwichte [2011]. They found the coronal rain oscillations to have small amplitudes on the order of few hundred km, periods ranging from 100 to 200 s, which are in agreement with the estimated period of the fundamental kink mode of the studied coronal loop and no observable damping. It became apparent that it is crucial to obtain and analyse observations of transverse oscillations of rainy coronal loops under a range of different conditions to pin down the factors affecting the oscillation properties and to understand the oscillation excitation mechanisms associated with thermal instability and coronal rain formation. In the following study, coronal rain oscillations were simultaneously observed by multiple instruments for the first time, enabling us to deduce information about the multi-thermal nature of the rain in different loop strands, and the degree to which the oscillatory behaviour of the individual strands occurs in a collective manner. The kinematics of the individual coronal rain condensations has been analysed by De Groof et al. [2004], De Groof et al. [2005], Antolin and Verwichte [2011], Antolin and Rouppe van der Voort [2012], Antolin et al. [2012] and Antolin et al. [2015b], finding that individual condensations mostly move with acceleration much less than the effective gravity in the loop. We employ similar approach to analysing the coronal rain kinematics. Finally, thermal evolution of coronal loop plasma during an onset of the thermal instability and coronal rain formation has been addressed by [Antolin et al., 2015b] by combining multiwavelength observations from SST/CRISP, IRIS, Hinode/SOT and SDO/AIA. They observed signatures of a gradual cooling of the plasma at the loop top, with the cooling itself exhibiting signatures of a two-step process, which was interpreted as being caused by the transition of the condensing plasma from optically thin to optically thick

regime. We therefore look for similar cooling signatures, focusing on the interpretation of the observations in the context of the evolution of both temperature and density of the coronal loop plasma.

The chapter is organized as follows: Section 2.2 covers the details of IRIS, Hinode/SOT and SDO/AIA observations used for analysis and the methods used for data processing. Section 2.3 focuses on analysis of MHD oscillations detected in the coronal rain. In Section 2.4 we investigate the kinematics of individual coronal rain blobs and present statistics of blob velocities and accelerations. In Section 2.5 we analyse the evidence for the thermal evolution of the loop plasma and the heating-condensation cycle of the coronal loop responsible for the coronal rain formation. Section 2.6 contains detailed discussion of the analysis outcomes and their implications.

2.2 Observations and data processing

We focus on observations taken by IRIS [De Pontieu et al., 2014], AIA on board SDO [Lemen et al., 2012] and SOT on board Hinode [Tsuneta et al., 2008]. The dataset analysed below was taken as a part of Hinode-IRIS-SST coordination (HOP 262) during August 2014 observing campaign focused on coronal rain with Warwick participation. An event from 2014 August 25 near NOAA AR 12151 is analysed using coordinated IRIS-Hinode observations and complemented by full-disk SDO/AIA data. We used IRIS level 2 SJI data taken between 7:46 and 10:30 UT retrieved from mission web page (http://iris.lmsal.com/search) in the NUV (Mg II k) and FUV (Si IV) filters with an exposure time of 8 s, 19 s cadence and the field of view centered at $[-984'', -196'']$ in solar heliocentric coordinates. We further used Hinode level 0 Ca II H data centered at $[-993'', -205'']$ in solar heliocentric coordinates, with the exposure time of 1.229 s and 12 s cadence taken between 8:20 and 9:37 UT. Using the AIA Cutout Service (http://www.lmsal.com/get_aia_data/) we retrieved the required subframes of level 1.5 SDO/AIA data with 12 s cadence that were normalised by the exposure time.

IRIS level 2 and SDO/AIA level 1.5 data used in this work already include geometric correction, dark correction and flat-fielding. The dark current correction and the flat-fielding of the Hinode level 0 data was carried out using the *fg_prep* Solarsoft routine. The data further required additional pre-processing in order to be suitable for the coronal rain analysis, in particular noise reduction, edge en-

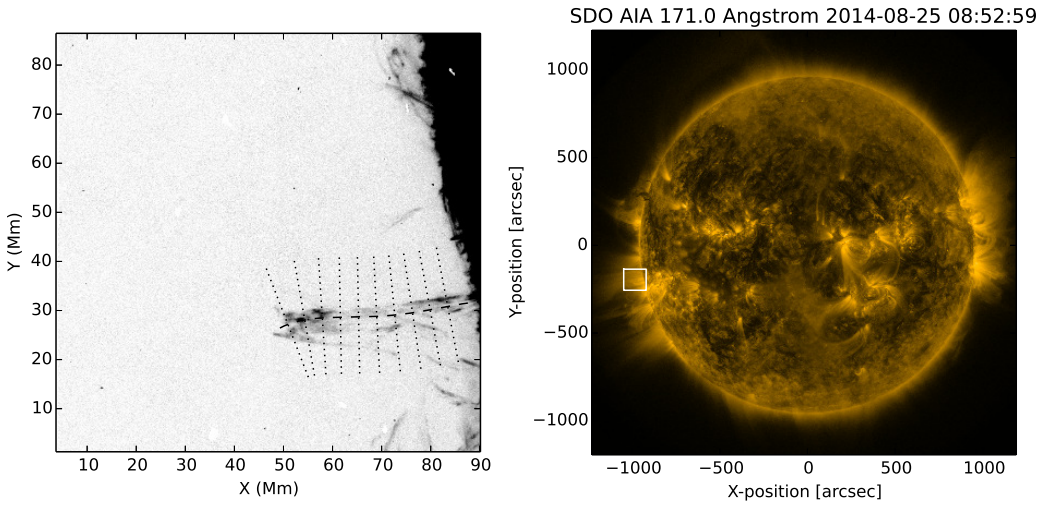

Figure 2.1: Left: Complete field of view of the IRIS Si IV observation used for analysis with the axis of the studied loop outlined. The cuts for the time-distance plots were taken along 10 slits perpendicular to the loop axis. Right: Position of IRIS field of view in the full-disk image as seen by SDO/AIA.

hancement and removal of trends in brightness variation across the data cube. Two dimensional Mexican hat wavelet transform filtering was used to achieve this by enhancing the features in the image with sizes close to the characteristic scale of the wavelet [Witkin, 1983; White and Verwichte, 2012]. We focus on a coronal loop outlined in Figure 2.1 showing IRIS Si IV SJI data. The loop is visible during the whole observing sequence; the coronal rain occurring in the loop can be observed for about an hour. The studied loop does not cross the spectrograph slit; no spectral information is therefore available and the analysis is restricted to the imaging data. The coronal rain is visible in IRIS FUV and NUV, Hinode Ca II H and SDO/AIA 304 Å bandpasses suggesting a multithermal nature of the phenomenon. The individual plasma condensations are best discernible in the Si IV line (1400 Å), which was therefore chosen for analysis.

The studied loop exhibits significant amount of coronal rain downflows as well as upflowing material. Most of the upward flow of the plasma occurs in the remote leg while the condensations are falling down preferentially along the loop leg closer to the observer. This asymmetry is likely caused by a background siphon flow due to a pressure difference between the footpoints. Such background flow can move the region where the thermal instability and subsequent condensation occurs to the side away from the apex resulting in coronal rain falling along one leg only.

The view of the observed event is limited to a single vantage point, we can therefore only make approximate estimates about the loop geometry. The loop plane appears approximately perpendicular to the solar surface. The positions of the axis of the loop, loop apex and foot points were determined from a series of multiple SJI time frames superimposed on each other to highlight the flows of the material in the loop. Multiple strands of plasma tracing the loop's magnetic field lines are observed, the loop therefore appears to have considerable thickness. The radius of the loop was estimated to be 40.9 Mm using the distance from the apex to the loop baseline connecting the two footpoints. Assuming the loop has a semi-circular shape, the estimate of the loop radius and the observed projected distance between the footpoints of 12.8 Mm was used to estimate the angle between the loop plane and the line-of-sight to be 9°.

The plasma condensations falling along the coronal loop are found to have considerable thickness of about 0.5 Mm, often grouping into strands. The individual strands clearly exhibit transverse oscillations which are best visible near the loop apex. The strands were observed to separate and merge again multiple times, thus complicating the tracking of the individual plasma blobs. The most pronounced elongation of the plasma blobs into strands occurs in the lower half of the loop. Individual strands were observed to converge as approaching the loop footpoints.

Longer duration AIA 304 Å dataset covering two 12 hour windows before and after the coronal rain event observed by IRIS and Hinode shows that it is a part of a sequence of successive coronal rain events occurring in the same coronal loop. A total of 4 events were detected on the day of observation. Other events were however much less clear due to multiple short-lived rainy loops appearing in the foreground, detailed analysis of the full 24 hour AIA dataset has therefore not been carried out.

2.3 Transverse oscillations

In order to detect any transverse oscillations of the structure, we set up 10 slits perpendicular to the loop axis (Figure 2.1). A cut through data was then taken along each slit and the data was superimposed over 30 pixels in longitudinal direction to detect oscillations of small blobs as well as of longer strands. The longitudinal superposition length was chosen as being long enough to detect short strand oscillations and short enough to capture any behaviour dependent on the longitudinal distance. The cuts at each time step were then stacked to create time distance

plots, each corresponding to different position along the loop. The time distance plots created using aligned IRIS Si IV, Mg II k and Hinode Ca II H data show large degree of similarity with the majority of strand-like structures being identifiable in all three wavelengths (Figure 2.2). This co-spatial emission with comparable intensities across temperatures ranging from chromospheric to transition region suggests multithermal nature of the coronal rain plasma. Time distance plots created using IRIS Si IV observations corresponding to two slits, one at the loop apex and another 22 Mm above the footpoint are shown in Figure 2.3. Multiple transverse oscillations are visible along the whole loop length. The contamination lasting from 75 min to 85 min in the IRIS observational sequence is caused by a surge of particles due to the spacecraft passing through the South Atlantic Anomaly.

Due to the large number of strands present at the same longitudinal distance, traditionally used automated strand detection methods based on fitting a Gaussian to the image intensity profile at each time step [Verwichte et al., 2009, 2010] proved unsuitable. The strand centre coordinates were therefore extracted manually from the time-distance plot for each slit to avoid errors that an automated procedure might introduce due to the nature of the intensity profiles. The strand centre displacement time series for each oscillation was then extracted and fitted with function $\xi(t) = \xi_0 \sin(\omega t + \Phi)$ using Levenberg-Marquardt algorithm in order to determine oscillation parameters. 150 oscillations were observed in total. The standard deviations on the best fit parameters for the individual oscillations were found to be 7%, 3% and 40% for the amplitude, period and phase respectively.

The time distance plots created using IRIS FUV data shown in Figure 2.3 suggest presence of two oscillation regimes: short period oscillations with small amplitude present along the whole loop length but being most prominent in the upper part of the loop; and long period oscillations with larger amplitudes visible only in the lower half of the loop. We repeat above analysis using SDO/AIA observations in 171 Å. Due to the 1.5 $''$ resolution of SDO/AIA, only large amplitude long period oscillation regime can be observed. Figure 2.4 shows the variation of the oscillation amplitude with the longitudinal distance of the corresponding slit from the loop apex corrected for the projection effects. There is no clear trend in the amplitude variation; however, the plot shows the distribution of the two populations of oscillations.

The amplitudes of the short period oscillations were found to mostly lie within a range 0.2 - 0.4 Mm. No prominent damping of the individual oscillations was observed, although one should note that since only few periods of the individual

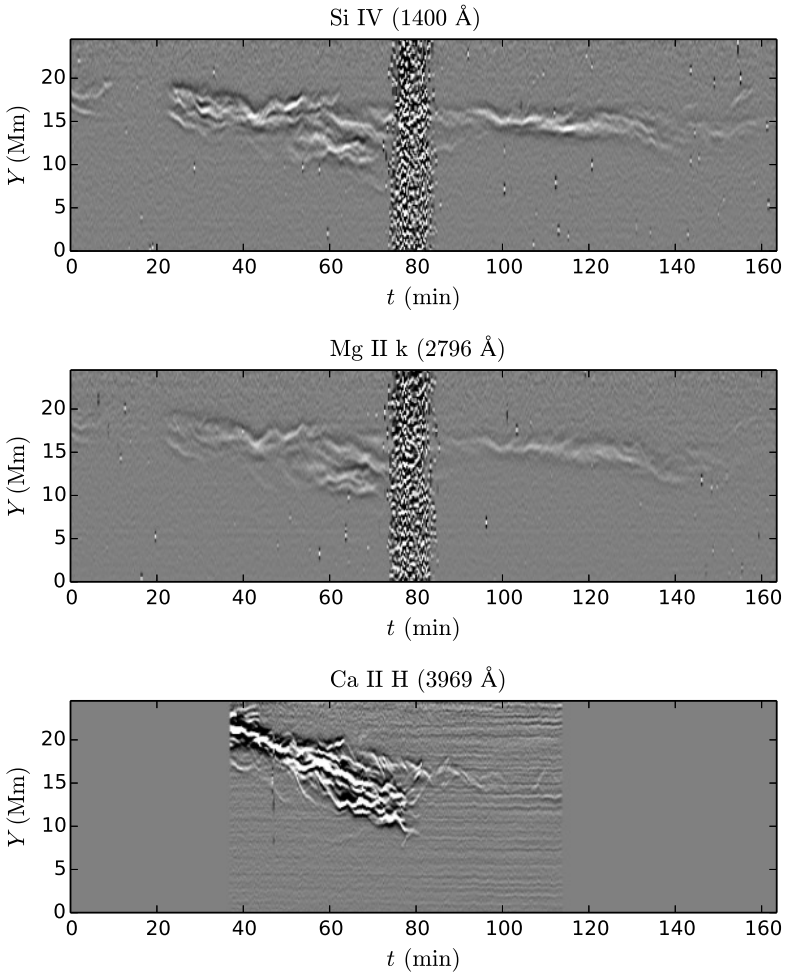

Figure 2.2: Time-distance plots corresponding to slit near the apex in IRIS Si IV (top), Mg II k (centre) and Hinode Ca II H line (bottom). Hinode data was interpolated to match IRIS time resolution and time range. Co-spatiality of the plasma emission suggest a multithermal nature of the coronal rain. Note somewhat different features at t = 40-50 min captured by Hinode only.

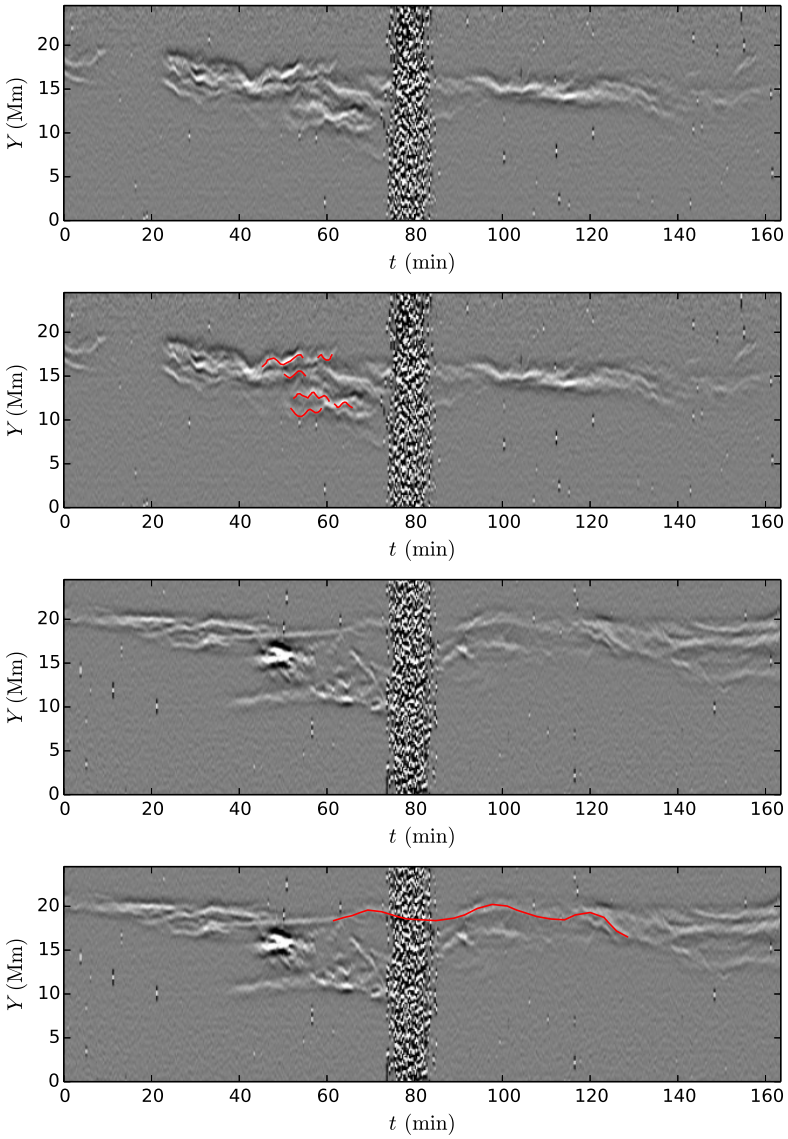

Figure 2.3: Time-distance plots corresponding to slits near the apex (top) and 22 Mm above the footpoint (bottom). We repeat each plot with the oscillation patterns highlighted. Small scale oscillations are present in both plots. A prominent large scale oscillating structure is visible only in the lower part of the loop. The particle contamination occurring during 75-85 min is due to the spacecraft passing through the South Atlantic Anomaly.

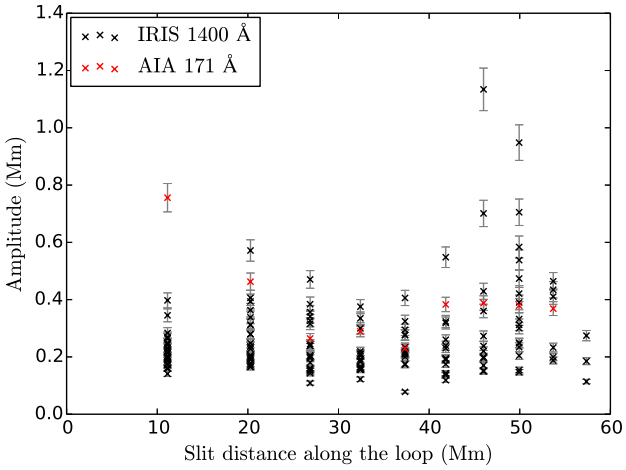

Figure 2.4: Variation of oscillation amplitude with the longitudinal distance of each slit from the loop apex corrected for projection effects.

oscillating strands can be observed, any gradual damping is likely to remain undetected. The mean period of the short period oscillations was found to be 3.4 min. The scatter of the periods of the individual oscillations around the mean value is likely to be a result of the uncertainty on the period measurements. If, despite the measurement errors, this scatter was real, varying periods of the oscillations detected in different positions within the loop would suggest large variations in the properties of the coronal loop plasma. However, due to the fact that a certain level of a collective behaviour of individual strands has been observed, we consider this scenario unlikely. A change of the mean oscillation period with time would in turn imply a presence of a non-linear driving process.

Multiple groups of nearby strands were observed to oscillate in phase. Synchronous oscillations were observed to be most prominent in the upper half of the loop. This is likely connected to the fact that only a small number of oscillations was observed near the loop foot points rather than being a significant evidence of a loss of collective behaviour in this part of the loop. There was no significant phase shift detected by comparing different heights, suggesting that the short period oscillation patterns are a manifestation of a global standing wave. However, the best-fit phase estimates are limited by large uncertainties due to the thickness of the individual strands.

The presence of synchronous oscillations of nearby strands together with the standing wave assumption points towards a number of possible scenarios for the nature of the wave in the coronal loop responsible for the observed oscillation patterns;

one such possibility is a global kink mode affecting the coronal loop as a whole. Alternatively, multiple kink modes present in the loop affecting each strand separately could cause in-phase transverse oscillating behaviour if triggered by a common source. Short period oscillations traced by the coronal rain with similar characteristics as described above were reported previously [Antolin and Verwichte, 2011].

Amplitudes of the long period oscillations observed in IRIS 1400 Å passband are of the order of 1 Mm. When observing the cool coronal rain plasma emitting at the chromospheric wavelengths they appear to be most pronounced in the lower part of the loop and fading higher up. At a distance of 37 Mm from the apex they cannot be observed at all. This is due to the cool plasma being more sparse in the upper part of the loop during the latter half of the observational sequence, which complicates tracking of long period oscillatory patterns. In the hot coronal wavelengths the long period oscillations are observable along the whole loop length, having similar periods as in IRIS observations but lower amplitudes (Figure 2.4). This amplitude discrepancy can be attributed to limited resolution of SDO/AIA, with the typical peak to peak amplitude of this oscillation regime being 3 pixels. At such short scales, the standard deviation of best-fit oscillation parameters estimated from a sample oscillation pattern might be an underestimate of the true uncertainty. The mean period of this oscillation regime is 17.4 min, i.e. much longer than typical period of the fundamental standing mode of the kink oscillation expected for a loop with comparable length. This suggests that the oscillatory pattern is a manifestation of a propagating rather than standing wave. In the propagating wave scenario the expected phase shift for such long period oscillations would be too small to be observed in the dataset with this duration.

2.4 Kinematics of coronal rain

The kinematics of the plasma condensations was analysed by tracking the individual blobs along their paths over the period during which they could be observed in the given bandpass. The individual plasma blobs were best discernible in the data taken in the IRIS Si IV filter, which was therefore chosen for kinematics analysis. Not all plasma blobs were observable during their entire motion from loop apex all the way to the footpoints; this is likely due to change in emission in the SI IV line following a temperature change.

By superimposing multiple time frames on each other, we were able to track 18 paths

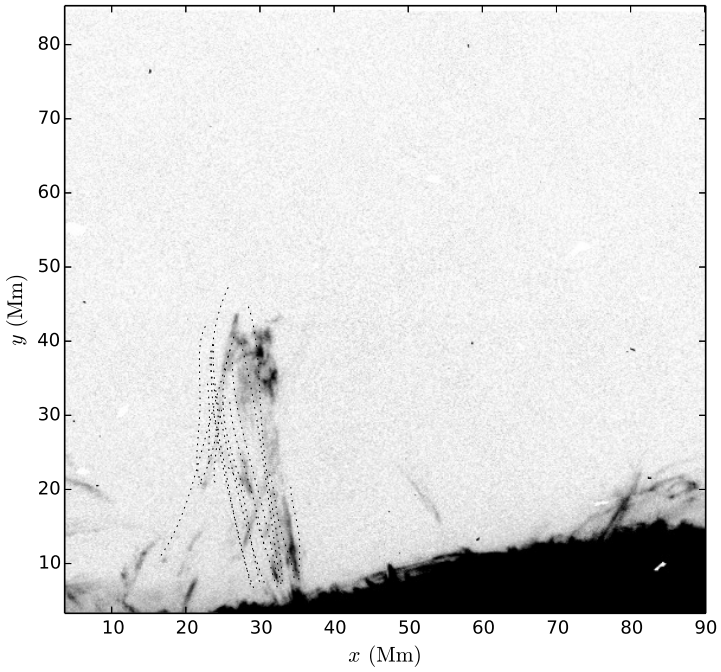

Figure 2.5: Observation snapshot with superimposed paths followed by condensations.

along which the condensations were moving (Figure 2.5). For each such path a time-distance plot was extracted. Three such time-distance plots are shown in Figure 2.6. The bright traces correspond to the trajectories of the individual condensations. A total of 115 plasma blobs were tracked, out of which 18 were part of the upflowing material and the remaining 97 blobs were falling condensations. In the subsequent analysis we focused on the coronal rain blobs. We extracted their trajectories and corrected them for projection effects by calculating the real distance travelled along the loop corresponding to the observed distance of the blob from the apex (assuming 9° loop plane angle and semicircular loop axis). For each blob an initial and final velocity was determined, enabling us to deduce mean acceleration of each blob.

The initial and final velocities and mean accelerations of the coronal rain blobs are shown in Figure 2.7. The distribution of velocities is broad ranging from small velocities of only few km s^{-1} to large velocities over 150 km s^{-1}, with the mean velocity being 45 km s^{-1}. The variation of the observed velocity with height is shown in Figure 2.8. The observed velocities of the individual blobs are largely below free-fall values, shown by the solid line. The distribution of blob accelerations is on the other hand much narrower and is clustered around the mean acceleration of 95 m s^{-2}. The average effective gravity along an ellipse is given by $\langle g_{eff} \rangle = 2/\pi \int_0^{\pi/2} g_\odot \cos\theta(s) ds$

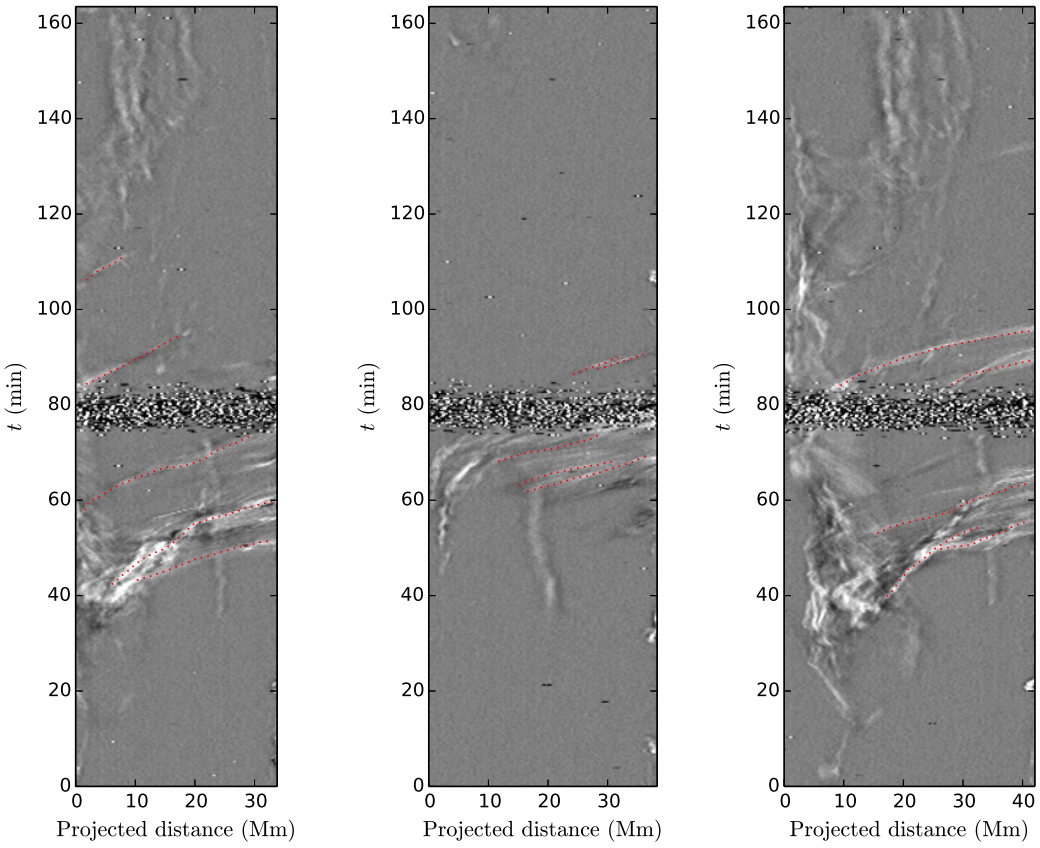

Figure 2.6: Time-distance plots extracted along 3 different paths followed by condensations. The horizontal axis corresponds to the projected distance along the path. The bright traces correspond to trajectories of individual blobs. In the rightmost plot, a number of blobs can be observed to oscillate around the loop top before falling down to the solar surface. The faint features stationary in the longitudinal direction are caused by background loops intersecting the axis of the studied coronal loop.

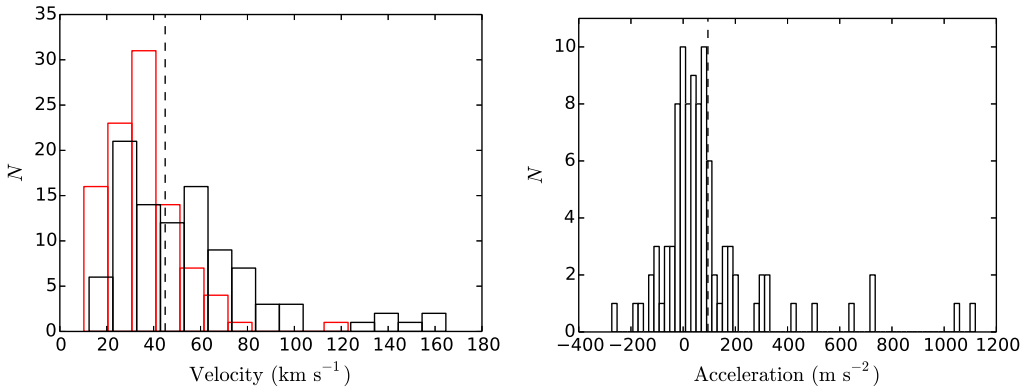

Figure 2.7: Left: the distribution of blob initial (red) and final velocities (black). Right: The distribution of mean blob accelerations. The dashed lines correspond to the average values of 45 km s^{-1} and 95 m s^{-2} for velocities and accelerations respectively.

where s is the coordinate along the ellipse and θ is the angle between the tangent to the path and the vertical. If assuming a semicircular loop axis, the average effective gravity along the loop is 174 m s^{-2}. The measured average acceleration is therefore significantly lower than what would be expected for a free-fall motion. Such sub-ballistic fall rates of coronal rain condensations were reported previously [Schrijver, 2001; De Groof et al., 2004; Antolin et al., 2010; Antolin and Verwichte, 2011; Antolin and Rouppe van der Voort, 2012]. Complete velocity and acceleration profiles of individual blobs also show multiple acceleration and deceleration phases as opposed to purely accelerated motion expected if the blobs would be moving solely under the influence of gravity (Figure 2.6).

2.5 Heating-condensation cycle

In order to determine the temperature evolution of the plasma in the studied coronal loop during the period of observation, we analyse the temporal change in emission in selected SDO/AIA filters. Here we use level 1.5 SDO/AIA data with 12 s cadence normalised by the exposure time, that we aligned with previously analysed IRIS and Hinode datasets. We select a region of the size 5×5 pixels at the loop top as shown in Figure 2.9. The normalised emission intensity in each filter is determined by averaging the data number (DN) counts over the region of interest and normalising by the total mean DN counts in each filter. Figure 2.9 shows the evolution of the total and normalised emission in 94 Å, 131 Å, 171 Å, 193 Å, 211 Å, 304 Å and

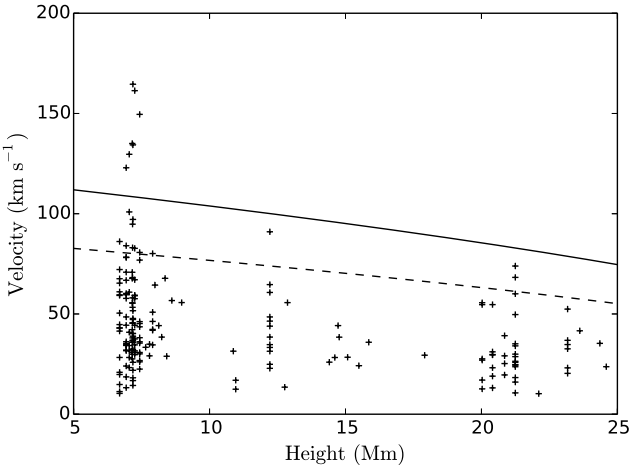

Figure 2.8: Dependence of blob velocity on the height above the solar surface. The velocity dependence expected for a free fall motion is shown by the solid line and the velocity dependence expected for a motion with the mean observed acceleration of 95 m s^{-2} is shown by the dashed line.

335 Å. The emission first peaks in 94 Å, followed by peaks in 335 Å, 171 Å, 131 Å and 304 Å, i.e. in progressively cooler bandpasses. It should be however noted that low intensities measured in 94 Å and 335 Å suggest that uncertainties in these light curves are large, thus reducing their reliability. In addition, the lack of single well-defined peak in the instrumental response functions of the 94 Å and 335 Å channels [Boerner et al., 2011] makes it non-trivial to infer a cooling sequence from the light curves in these two channels. The emission in 193 Å and 211 Å is on the other hand observed to be steadily increasing, with a number of secondary peaks. The sequence of prominent peaks in 171 Å, 131 Å and 304 Å channels therefore clearly suggests a gradual cooling of the plasma at the loop top, while the emission in 94 Å, 335 Å, 193 Å and 211 Å channels does not provide additional evidence of cooling.

We further estimate the temperature distribution of the emission of the loop plasma integrated along the line of sight as a function of time. This can be quantified by the differential emission measure (DEM) $\xi(T)$ defined as

$$\xi = n_e^2 \frac{dz}{dT} \tag{2.1}$$

where n_e is the electron density, z is the distance along the line of sight and T is the temperature. The observed intensities are a result of a convolution of the DEM

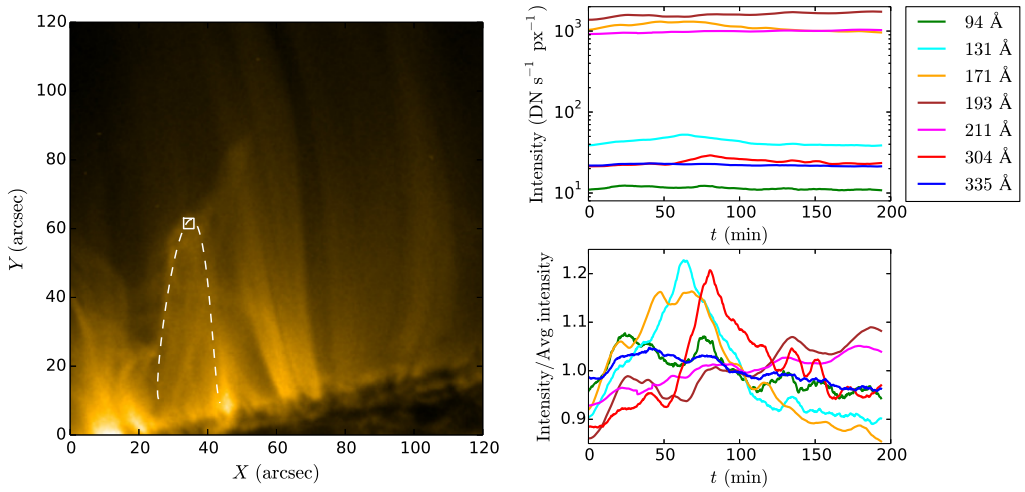

Figure 2.9: Left: SDO/AIA 171 Å view of the studied coronal loop. The marked region at the loop top used to obtain the evolution of the intensity of the emission. Top right: Evolution of the observed emission intensities in 7 SDO/AIA filters corresponding to the region at the loop top. Bottom right: Emission intensities normalised by the average number of counts.

with the instrumental response functions:

$$F_i = \int \xi(T) R_i(T) dT \tag{2.2}$$

where F_i is the intensity measured in the ith bandpass and R_i is the instrumental response function of the ith filter dependent on the temperature. This can be projected into finite-dimensional space as:

$$F_i = R_{i,j} \xi(T_j) \tag{2.3}$$

Determining the DEM from the above linear equation however poses two main challenges. First, due to the limited number of the instrument bandpasses the number of the temperature bins of the observed intensities is typically smaller than the number of the temperature bins for which the DEM is evaluated, thus leading to the DEM inversion being an under-constrained problem. Second, the large differences between the magnitudes of the individual components of the response matrix R result in large noise amplification by the inverse mapping. These can be overcome by adding additional constraints to the problem. To do this, we use the zero-order Tikhonov regularisation based on selecting the solution with the smallest norm [Tikhonov,

1963]. This is equivalent to using Lagrange multipliers to solve the least square problem subject to constraints imposed by adding the regularisation term:

$$\Phi = |R\xi(T) - F|^2 + \lambda |L(\xi(T) - \xi_0(T))|^2 \tag{2.4}$$

with Φ to be minimised, λ being the regularisation parameter, L being the constraint matrix (proportional to the identity matrix in the case of zero-order regularisation) and $\xi_0(T)$ being the expected (or guess) solution. This is then solved by diagonalising the matrices R and L using generalised singular value decomposition, with the $1/\lambda$ term in the resulting expression effectively smoothing the solution by filtering out small singular components. To implement the steps above, we use the DEM regularisation method by Hannah and Kontar [2012], which we adapted to Python programming language. We run the DEM regularisation using the SDO/AIA data in the same bandpasses as above averaged over the region of interest shown in Figure 2.9. We further averaged the data over 20 time frames to increase signal-to-noise ratio. We reconstruct the DEM for a temperature range between $\log T = 4.5$ and $\log T = 7.3$ and further apply additional constraint on DEM by requiring it to be positive. Time evolution of the resulting DEM is shown in Figure 2.10.

The prominent DEM peak is centred around $\log T = 6.0$. We are most concerned with the DEM evolution below $\log T = 6.0$, especially with the secondary peak that develops around $\log T = 5.0$. The amount of plasma in the transition region temperature increases during the first 50 min of the observation coinciding with the time interval of the coronal rain occurrence in the upper part of the loop. It should however be noted that the validity of the DEM inversion is based on the implicit assumption of the optically thin emission, the resulting DEM evolution in the lower end of the analysed temperature range should therefore be treated with caution.

Given that the 304 Å channel is most likely to be sensitive to optically thick emission, we repeated the DEM inversion without using the 304 Å channel (Figure 2.10). This mostly affects the evolution of the low-temperature region, with the early time peak shifted to $\log T = 5.5$. Aside from that the overall shape remains similar. Figure 2.11 shows the evolution of the DEM integrated along the whole temperature range (representing the evolution of the total amount of plasma at the loop top) and the intensity in the IRIS Si IV time-distance plot corresponding to the slit at the apex (as shown in Figure 2.3) averaged in transverse direction. The linear correlation coefficients between the Si IV emission intensity and EM recovered with and without using the 304 Å channel are 0.41 and -0.10 respectively. When including

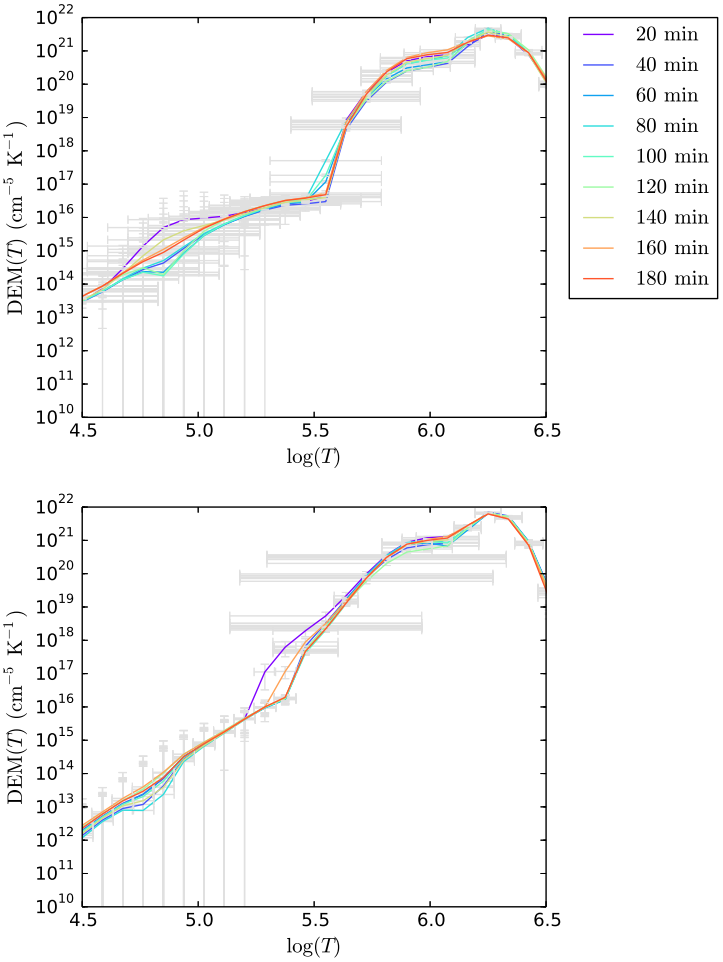

Figure 2.10: Evolution of the regularised DEM plotted every 100 time steps including (top) and (bottom) excluding the 304 Å channel.

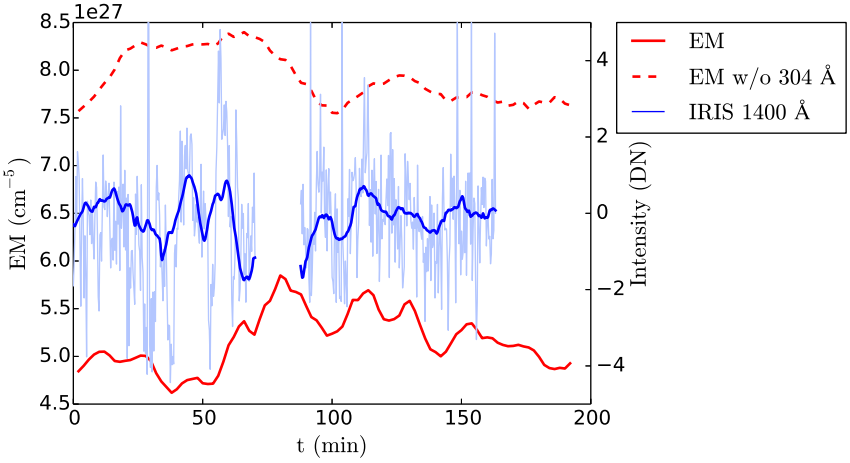

Figure 2.11: Evolution of the emission measure integrated along the whole temperature range (red) and of the Si IV emission intensity in the time-distance plot corresponding to the slit at the loop apex (blue). The solid and dashed lines show the emission measure recovered with and without using 304 Å channel respectively. All time series have been smoothed for clarity. The data gap in Si IV emission time series corresponds to the SAA-contaminated data.

the 304 Å channel the overall amount of plasma correlates well with the evolution of the emission in Si IV line, with matching time scales on which the quasi-periodic large scale variations occur. In the second case no clear correlation is present. We therefore conclude that due to its broad temperature response the 304 Å channel can help to better constrain the DEM in the lower temperature range.

The DEM reconstruction and the evolution of the individual light curves together with the occurrence of successive coronal rain events in the same loop suggest that the observed sequence is a part of a continuously repeating heating-condensation cycle, consisting of a heating phase, followed by radiative cooling of the loop top leading to the thermally unstable regime and subsequent condensation of the plasma, which is then followed by another heating phase.

We further verify the above scenario by forward modelling the expected emission intensities in the individual SDO/AIA bandpasses corresponding to a simple heating-cooling process. We created a synthetic time-dependent model of the DEM consisting of 2 components. The constant background component corresponds to the background emission of the coronal plasma and was modelled using the CHIANTI active region model [Dere and Mason, 1993]. The low temperature part (below $\log T = 5.5$) was removed and the remaining DEM scaled down by an arbitrary factor of 20 to account for the fact that we are modelling an off-limb region. The emis-

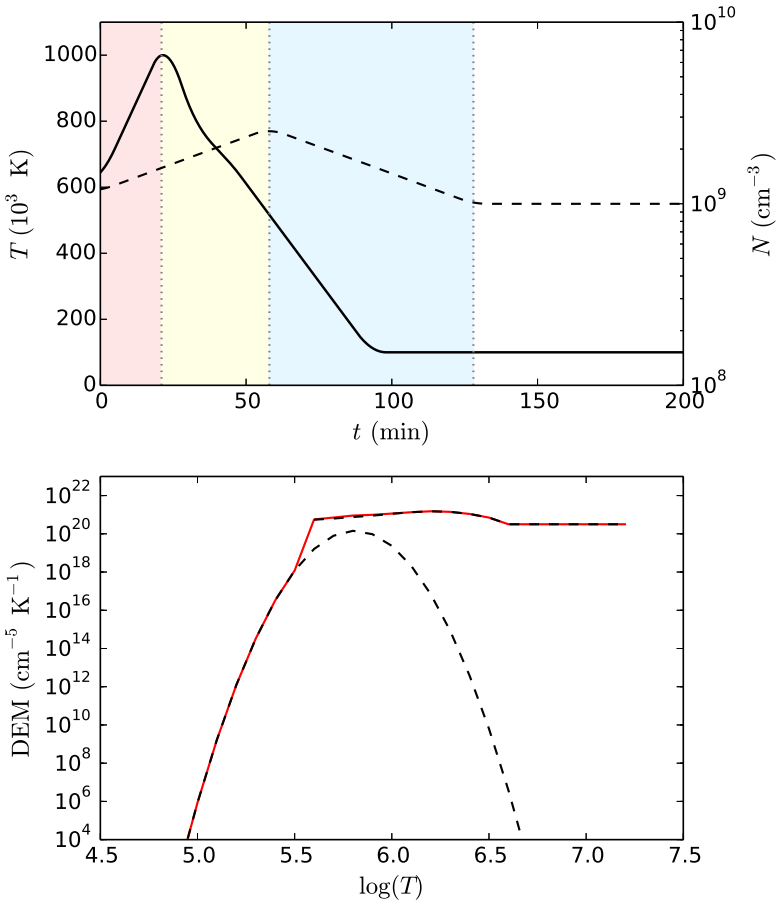

Figure 2.12: Top: Evolution of the mean temperature T_0 (solid line) and density (dashed line) of the plasma at the loop top used to generate the DEM model. The coloured sections mark the individual phases of the loop thermal cycle: Heating (red), condensation (yellow) and evacuation (blue). Bottom: The DEM model at $t = 0$ used to calculate simulated intensities is shown in red. The individual components (constant CHIANTI active region DEM and Gaussian DEM corresponding to the loop plasma) are shown by the dashed line.

sion therefore does not contain the low-corona, transition region and chromospheric elements present in on-disk observation. The foreground component corresponds to the emission of the plasma at the loop top and is time-dependent. We model the foreground DEM as a Gaussian of the form:

$$\xi(T) = \xi_0(T) \exp(\frac{-(\log T - \log T_0)^2}{2\sigma^2}) \tag{2.5}$$

where $\xi_0(T) \propto n_e^2 z$ is the peak emission measure dependent on the electron density and the line-of-sight integration depth, which we estimate to be of the order of 1 Mm, $\sigma = 0.1$ and $\log T_0$ is the mean temperature of the loop plasma. $\log T_0$ evolves according to a process consisting of a heating stage characteristic by a linear increase in temperature up to maximum value of $\log T = 6.0$, catastrophic cooling stage associated with the coronal rain formation where the temperature decreases exponentially and a final gradual cooling stage down to $\log T = 5.0$ (Figure 2.12). The evolution of the plasma density is modelled in a similar manner to vary linearly between $\log n_e = 9.0$ and $\log n_e = 9.4$ but with the peak slightly delayed, as shown in Figure 2.12. The initial and peak values were chosen based on typical values expected in active region coronal loops. No direct correlation between the plasma temperature and density is explicitly assumed due to hydrostatic non-equilibrium being the fundamental characteristic of the footpoint-heated loops likely to undergo catastrophic cooling. This evolution effectively marks 3 distinct phases in the cycle: 1. heating with chromospheric evaporation associated with increasing T and n_e, 2. radiative cooling followed by thermal instability and plasma condensation associated with decreasing T and increasing n_e and 3. further cooling accompanied by evacuation of the plasma at the loop top associated with decreasing T and n_e.

The synthetic light curves for each SDO/AIA bandpass are calculated by convolving the composite DEM with the SDO/AIA instrumental response functions [Boerner et al., 2011] using Eq. (2.2). Figure 2.13 shows the absolute modelled emission intensities and the intensities normalised by the average value in each bandpass for the sake of easy comparison with the observed values. Large scale characteristics, average values and amplitude of variations in the observed emission intensities are generally in good agreement with those predicted for the heating-cooling cycle with the given temperature and density evolution. The average observed emission intensities in the 193 Å and 211 Å bandpasses are however higher than predicted; this is likely is caused by the fact that the background model used here underestimates the emission in hot coronal wavelengths for the observed region. As with the observed

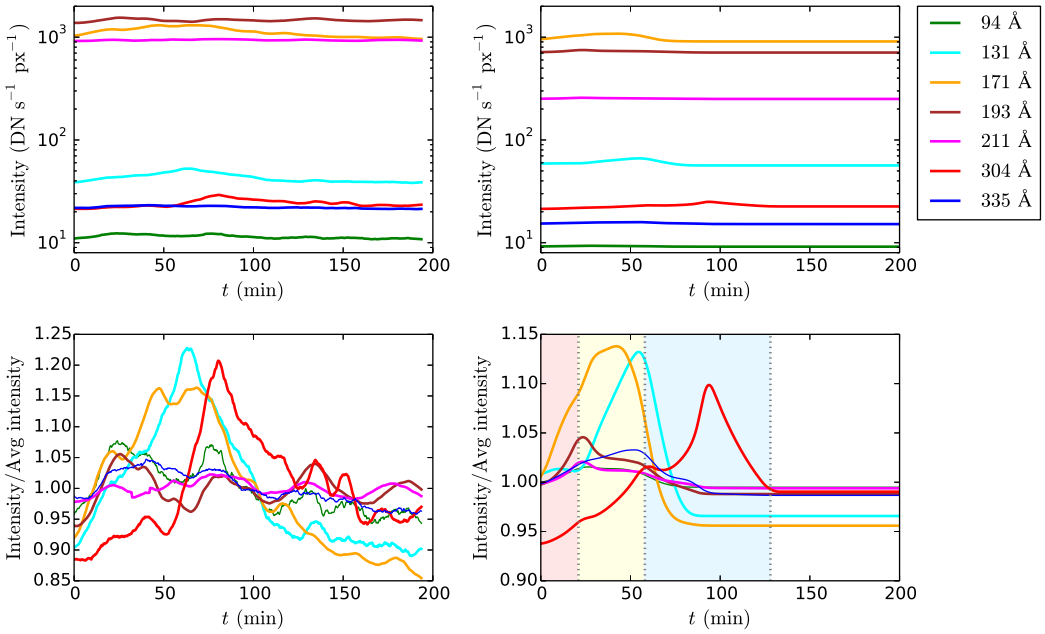

Figure 2.13: Comparison of the observed (left) and simulated emission intensities based on a 2 component DEM model corresponding to a simple heating-cooling process (right). The linear trend from the observed emission in 193 Å and 211 Å channels has been removed. Bottom panels show the emission intensities normalised by the average number of counts. The coloured sections mark the individual phases of the loop thermal cycle: Heating (red), condensation (yellow) and evacuation (blue).

intensities, a clear signature of gradual cooling of the plasma in modelled evolution of the emission is present, consisting of the emission peaking in subsequently cooler bandpasses. As mentioned above, the emission in 193 Å and 211 Å is observed to gradually increase, with a number of smaller secondary peaks present, which is in disagreement with the single peak in each bandpass predicted by the model. This can be attributed to the temperature of the background coronal plasma steadily increasing. Such evolution could be expected e.g. for a bundle of thermally unstable loops in the background which are also going through the heating phase of the heating-condensation cycle but with the instability timescale being longer (e.g. due to longer loop length). This is further supported by the fact that the multiple prominent peaks in the 193 Å and 211 Å are each accompanied by secondary peaks in other bandpasses, which are not exactly co-temporal due to the expected temperature change. The observed evolution is therefore likely a result of superposition of multiple cooling/heating sequences in the foreground/background. The simulated emission peaks in 171 Å, 131 Å and 94 Å are narrower than observed and the decay of all light curves is more rapid than observed. Here it should be noted that the DEM model used is valid for a monolithic loop. Multithermal structure of the coronal loop would result in greater width of the emission peaks, in line with the observations. Considering the above limitations of the background model and the fact that at lower temperatures the plasma is likely entering the optically thick regime, the forward modelling approach should be viewed as a demonstration of the feasibility of the limit cycle model given the observed light curve evolution rather than as a direct reproduction of the observations.

2.6 Discussion and conclusions

2.6.1 Transverse oscillations traced by coronal rain

There is a number of possible sources that could potentially be responsible for the two distinct oscillation regimes with different periods. The 3.4 min average period characteristic for the small scale oscillation regime is consistent with the period of the fundamental standing mode $P \approx \sqrt{2}L/v_A \sim 3$ min if using typical estimate for the Alfvén speed (~ 1000 km s^{-1}) and loop length determined previously (129 Mm). Absence of observable damping in the small scale case suggests a presence of a continuously operating non-resonant driver. The mean period of the large scale oscillation regime is much longer than one expected for the fundamental harmonic

and therefore cannot be associated with the standing mode scenario, suggesting the agent instead being a propagating wave. Here the intermittent nature of the oscillations implies localised, transient driving mechanism operating near the foot points of the coronal loop.

Most prominent sources of the MHD waves in the corona are solar flares and other energetic events, which can be observed in a number of passbands (radio, UV, X-ray) as well as in the particle flux measurements. Such events were found to excite transverse oscillations in the coronal loops with the periods on the order of minutes [Aschwanden et al., 2002; Nakariakov et al., 2009], matching the time scale of the small scale oscillation regime observed and discussed in this work. However, event-triggered loop oscillations usually exhibit strong damping and were found to typically decay within few oscillation periods [Nakariakov et al., 1999; White and Verwichte, 2012], unlike the oscillations described here. There were no detected flares or other energetic events occurring on the date of the observation near AR 12151. An M class flare occurred in this active region during the previous day and a series of C class flares was observed in AR 12149 and AR 12150 on the day of observation; these were however perceived as being too distant to have a significant effect on the studied coronal loop. The limited STEREO-A dataset available for the day of observation was also checked to exclude the possibility of a nearby flare occurring behind the limb.

The persistent nature of the small scale oscillations and their lack of observable decay instead suggests that there is a possible link with the decayless transverse oscillations of coronal loops in non-flaring active regions having similar characteristics which were observed at EUV wavelengths [e.g. Nisticò et al., 2013]. If the small scale oscillation regime is indeed a manifestation of the same process as these decayless loop oscillations, the common occurrence of this phenomenon implies a global nature of the driving mechanism; possibly a stochastic driver (e.g. small scale reconnection events or stochastic motions in the chromospheric network resulting from granular flows). Another possibility is a global helioseismic p-mode coupling to the loop footpoints. Because of the large number of other loops in the vicinity of the studied coronal loop, a possibility of an interaction with neighbouring loops has to be taken into account. Assuming that their proximity is not just a projection effect, interaction with the neighbouring loops could perturb the conditions in the studied loop and trigger both condensation region formation and transverse loop oscillations. It has also been suggested that if the inertia of the coronal rain blobs is not negligible the condensations themselves could excite the oscillations in the loop.

Detailed analysis of this scenario will be addressed in the following chapters.

2.6.2 Kinematics of the individual condensations

The reasons behind sub-ballistic fall rates of the coronal rain blobs are less clear and subject to ongoing discussion. Gas pressure gradients in the loop are thought to have strong effect on the dynamics of plasma condensations. As the condensation falls down along the magnetic field line, it compresses the plasma below. The resulting strong pressure could slow down the blob significantly. Numerical simulations show that these pressure effects can be strong enough to account for some of the observed deceleration [Müller et al., 2005; Fang et al., 2013; Oliver et al., 2014]. The motion of the blobs would also appear sub-ballistic if the blobs would be moving along paths resulting from helical structure of magnetic field lines. Such helical configuration of the magnetic field would however need to be stable for extended periods of time which we consider unlikely. Another factor that needs to be considered is the ponderomotive force (PMF) exerted by the transverse oscillations in the loop. The PMF can be directed either along or against the direction of the motion of the condensations depending on their position along the loop and on the harmonic of the transverse standing wave in the loop. This would provide an explanation for the multiple acceleration and deceleration phases in the blob motion. The scenario that the coronal rain evolution is at least partially affected by the PMF is further supported by the fact that a number of coronal rain blobs was observed to oscillate around the loop top, as shown in Figure 2.6. Model of the effect of the PMF on the kinematics of the coronal rain has been proposed by Verwichte et al. [2017a].

2.6.3 Thermal evolution of the coronal loop and limit cycles

Our observations of the thermal evolution of the plasma in the studied coronal loop are consistent with the limit cycle model, where steadily heated loops are expected to undergo periodically repeating cycles consisting of heating and condensation phases with the periods on the time scales of hours, typically dependent on the loop length and the shape of the heating function. A possibility of cyclic evolution of coronal loops was first addressed by Kuin and Martens [1982] who obtained an oscillatory solution if the strength of the coupling between the coronal loop and the chromosphere was lower than a critical value, using a relatively simple semi-analytical model based on modelling the loop as a 0-dimensional system. Their model was further generalised by Gomez et al. [1990] by fully accounting for the hydrodynamic

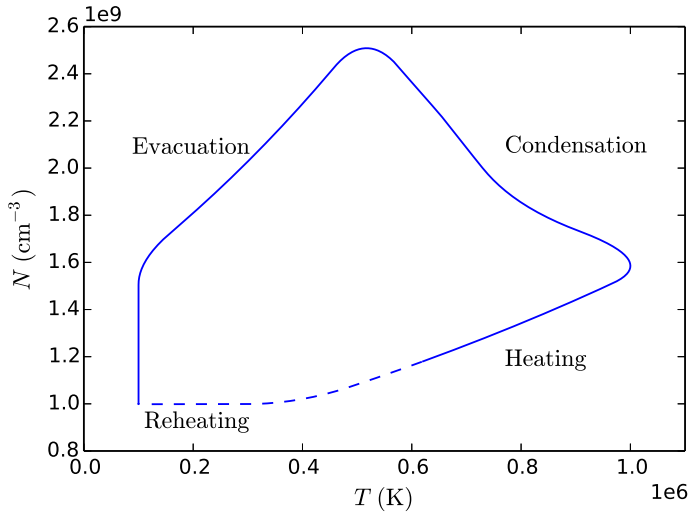

Figure 2.14: Phase diagram of the loop evolution deduced from forward modelling the SDO/AIA emission intensities. The dashed line shows extrapolated evolution prior to the start of the observational sequence.

considerations whose solution has the form of subcritical Hopf bifurcation. These models are of course highly simplified and use average values of the temperature and density along the loop, hence they do not account for a variation in the spatial distribution of the heating function, which we now know is an important factor that determines the thermal instability onset. They can be however still used for prediction of the general behaviour of the system, since they account for key ingredients of the heating-condensation cycle: chromospheric evaporation, catastrophic cooling and subsequent evacuation of the loop. The limit cycle behaviour has been also predicted by a number of numerical studies [e.g. Karpen et al., 2001; Müller et al., 2003; Fang et al., 2015].

Considering an idealised temperature-density limit cycle similar to the oscillatory solution of Kuin and Martens [1982], we expect presence of 4 different stages of the loop evolution in one cycle period (Figure 2.14): a heating phase associated with increasing temperature and density due to the chromospheric evaporation of the plasma into the loop; a radiative cooling phase associated with the rapid cooling and subsequent condensation of the plasma at the loop top, resulting in the decreasing temperature and increasing density, gradual cooling phase accompanied by the evacuation of the loop top as the coronal rain plasma falls towards the solar surface, thus decrease in the plasma density and final reheating phase where the density continues to decrease and the heating starts again. It can be immediately

seen that the first three stages of expected limit cycle behaviour are in agreement with the evolution of the plasma density and temperature deduced by the forward modelling of the observed emission intensities carried out in this study. It should be noted that when looking at the evolution of the observed emission intensities alone, only the cooling part of the heating-condensation cycle has a clear observational evidence (i.e. sequential peaks in progressively cooler bandpasses), given the lack of a simple observational signature of the presence of a heating phase immediately preceding the cooling of the loop plasma. The deduced effect of adding the heating phase on the onset of cooling progression when forward modelling the emission intensities however seems to be in line with the observations. This, together with the repeated coronal rain occurrences in the same coronal loop supports the complete heating-condensation cycle scenario.

Whereas the resulting DEM evolution calculated using the regularisation method is in agreement with the results deduced using the forward modelling approach, care must be taken with the interpretation of the thermal evolution of the plasma in the lower end of the analysed temperature range, where it is likely entering the optically thick regime. In addition, contamination of the emission from the studied region by the emission of the hot coronal background seems to be an ongoing problem. In order to evaluate the degree to which the DEM determined in this work is affected by the coronal background, it should be pointed out that due to the greater column depth, the contamination by the background emission is likely to be more severe near the solar limb than near the centre of the solar disk, where the DEM is usually much more accurate [e.g. Warren et al., 2010; Hannah and Kontar, 2012]. Since the coronal rain is best observed off-limb, this poses a challenge for the extraction of the relevant information about temperature evolution of the studied coronal loop. The background subtraction was not carried out in this work, as it proved impossible to select a reference area where the average intensity in the most noisy channels (94 Å and 335 Å) would be less than the average value in the analysed region in all time frames. An alternative approach would be to simply exclude these two channels from the analysis. However, this was viewed as undesirable due to the fact that it would lead to the DEM being even more under-constrained. Including the effect of the hot coronal background and tackling the problem using the forward modelling therefore seems to be the most viable approach for the off-limb regions. However, as shown by this work, the steady background model has its limitations, since a change in the background temperature during the period of the observation (e.g. due to a bundle of loops undergoing similar heating-cooling cycles, but with longer cycle periods) is entirely possible.

The change of plasma density near the loop top resulting from the chromospheric evaporation and subsequent condensation is expected to have an effect on the Alfvén speed in this part of the loop. For the change in density by a factor of 2.5 as estimated in the previous section, the Alfvén speed $v_A = B/\sqrt{\mu_0 \rho}$ is expected to change by a factor of 1.6. With $v_{ph} \approx \sqrt{2} v_A$ and $v_{ph} = \lambda / P$, this decrease in density will result in decrease in the oscillation period by a factor of 1.6 and vice versa. The observed scatter in the period of the oscillations traced by the coronal rain blobs could therefore be partially caused by the density change due to evacuation of the loop top.

Chapter 3

Dynamics of plasma condensations in a gravitationally stratified coronal loop

Contents of this chapter have been published in Kohutova and Verwichte [2017a].

3.1 Introduction

High-resolution solar observations show that the motion of coronal rain blobs is significantly sub-ballistic [e.g. Antolin and Verwichte, 2011; Antolin and Rouppe van der Voort, 2012], suggesting that forces other than gravity have an important effect on its dynamics and evolution. The formation and evolution of plasma condensations have been addressed by a number of numerical studies using 1D hydrodynamic simulations. The thermal instability onset and coronal rain formation in a coronal loop with footpoint-concentrated heating typically depends on the spatial distribution of the heating input and often occurs in periodically repeating limit cycles [Müller et al., 2003, 2004]. Using a 1D approach, the pressure effects are found to have a strong influence on the motion of the individual coronal rain blobs, often counteracting the effect of gravity [Antolin et al., 2010; Oliver et al., 2014] in the case of a compressed plasma below the condensation, providing net upward pressure gradient force. Conversely, if a plasma condensation is moving in a low-

pressure region, such as in the wake of a previously formed condensation, this can result in motion that is faster than free-fall [Müller et al., 2005].

The 1D hydrodynamic simulations modelling the evolution along a single field line neglect the effect of the finite magnetic field, however, as all of the plasma is confined below the condensation, and therefore 1D simulations likely overestimate the decelerating effects of coronal loop plasma pressure gradients. The effect of the finite magnetic field on the coronal rain evolution is only properly accounted for when using multidimensional magnetohydrodynamical (MHD) models.

Siphon flows due to local pressure variations can also have a strong effect on the motion and morphology of coronal rain condensations, as shown by 2D MHD studies of coronal rain formation and evolution [Fang et al., 2013, 2015].

Using 2D MHD simulations, Mackay and Galsgaard [2001] investigated the evolution of a density enhancement in the context of cool prominence material. The density enhancement was found to rebound multiple times in this setup, which was explained as a two-step process: a deceleration phase caused by the pressure build-up below the enhancement, and a rebound phase caused by the restoring action of the Lorentz force, stressing the importance of the effect a finite magnetic field can have on the evolution of plasma condensations. Similar longitudinal oscillations of cool condensations can be seen in coronal rain observations [Verwichte et al., 2017a] as well as in prominences [e.g. Jing et al., 2003; Zhang et al., 2012; Luna et al., 2014].

In order to investigate the mechanisms affecting the dynamics of the coronal rain and potential reasons behind the sub-ballistic speeds seen in observations, we carry out 2.5D MHD simulations of coronal rain dynamics. We model the evolution of a cool plasma condensation in a realistically stratified atmosphere that includes a cool high-density chromosphere, a transition region layer, and a hot corona. We choose our problem setup to be representative for small coronal rain condensations that are typically formed in thermally unstable loops as a result of catastrophic cooling. The geometry of the problem is therefore set up to reflect the coronal loop geometry, accounting for the reduced effective gravity due to the semicircular shape of the loop. We furthermore analyse condensation trajectories, velocities, and accelerations in order to be able to compare them to recent high-resolution coronal rain observations. Finally, we propose an analytical model for the condensation dynamics in order to explain the oscillatory behaviour of the plasma condensations and compare it with the numerical findings.

The chapter is structured as follows. Section 3.2 describes the numerical setup used to study dynamics and evolution of a cool plasma condensation in a gravitationally stratified coronal loop. In Section 3.3 we analyse condensation dynamics. High magnetic field or low condensation densities are found to lead damped oscillatory motion of the condensations. In Section 3.4 we investigate the evolution of the individual forces acting on the condensation to determine the mechanisms responsible for the oscillatory behaviour. Using these findings, in Section 3.5 we further propose an analytical model for the damped oscillatory motion of the condensations. Section 3.6 contains detailed discussion of the simulation results and their implications.

3.2 Numerical model

We solve the nonlinear MHD equations using Lare2d [Arber et al., 2001] assuming quasi-neutral fully conductive plasma and including gravity and shock viscosity. We use the ideal equation of state. Thermal conduction and radiative transport are not included in the energy equation. We introduce a rectangular simulation domain with the extent -30 Mm $\leqslant x \leqslant$ 30 Mm in horizontal direction and -120 Mm $\leqslant y \leqslant$ 120 Mm in the vertical direction with 512 $\times$ 2048 resolution. The coronal loop is modelled as a straight slab along the y-direction. We adopt the variable s to describe the position along the loop from one footpoint to the other, that is, $s = y + 120\,\mathrm{Mm}$. Thus, the loop has a length of 240 Mm. The density variation between the loop and the background medium in the x-direction is given by the symmetric Epstein profile [Nakariakov and Roberts, 1995]:

$$\rho(x) = \rho_\mathrm{e} + (\rho_\mathrm{i} - \rho_\mathrm{e})\,\mathrm{sech}^2\left(\frac{x}{a}\right), \tag{3.1}$$

where ρ_e and ρ_i are external and internal densities, respectively, and $a = 3$ Mm is the loop scale width. We assume a constant density contrast $\rho_\mathrm{i}/\rho_\mathrm{e} = 10$ throughout the whole domain. In order for the setup to be representative of a semicircular coronal loop with both footpoints anchored to the photosphere, the effective gravity g_eff is determined assuming a semicircular coronal loop of length L and varies with the coordinate along the loop s as

$$g_\mathrm{eff}(s) = g_\odot \cos\left(\frac{\pi s}{L}\right), \tag{3.2}$$

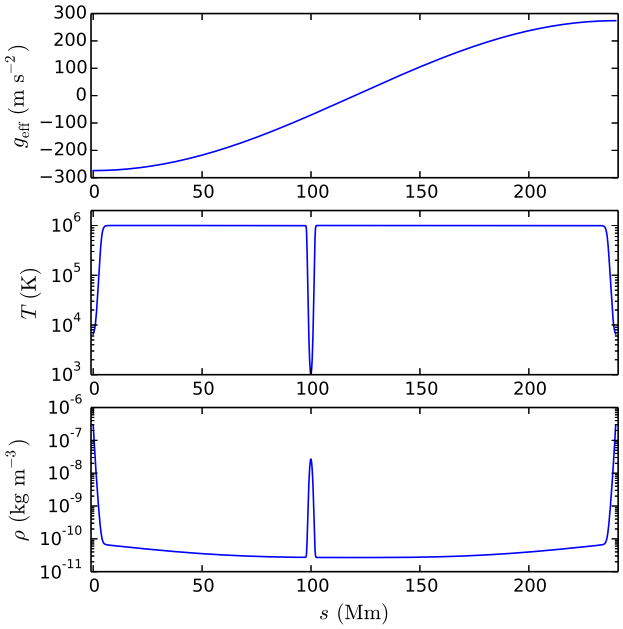

Figure 3.1: Initial effective gravity, density, and temperature profiles as a function of s at $x = 0$.

such that it equals zero at the loop top in the centre of the domain and $g_\odot = 274$ m s^{-2} at the loop footpoints at the top and bottom domain boundaries (Figure 3.1). The temperature is constant in the x-direction. In the vertical direction we create a realistic temperature variation representative of an atmosphere consisting of a cool chromosphere, transition region layer and hot corona by adopting a smoothed step function temperature profile [Cargill et al., 1997]:

$$T(s) = \frac{1}{2}(T_{\rm cor} + T_{\rm ph}) + \frac{1}{2}(T_{\rm cor} - T_{\rm ph}) \tanh\left(\frac{h(s) - s_{\rm t}}{\Delta s}\right), \tag{3.3}$$

with photospheric temperature $T_{\rm ph} = 6 \times 10^3$ K, coronal temperature $T_{\rm cor} = 10^6$ K, $s_{\rm t} = 4$ Mm, $\Delta s = 1$ Mm and $h(s) = \frac{L}{\pi} \sin \frac{\pi s}{L}$. The temperature variation controls the pressure scale height $H(s)$:

$$H(s) = \frac{k_b T(s)}{m g_{\rm eff}}. \tag{3.4}$$

The density profile for the non-isothermal stratified atmosphere is then determined by numerically solving for a hydrostatic pressure balance:

$$p(s) = p_0 \exp\left(-\int_0^{h(s)} \frac{\cos\left(\frac{\pi s'}{L}\right) ds'}{H(s')}\right), \tag{3.5}$$

$$\rho(s) = \frac{mp(s)}{k_b T(s)}\,. \tag{3.6}$$

The density stratification in the initial configuration is calculated using a footpoint density of $\rho_0 = 6.5 \times 10^{-7}$ kg m^{-3}. This results in the densities in the upper region of the loop of the order of 10^{-11} kg m^{-3} , which are representative of real coronal densities. The top and bottom boundaries are fixed to create a line-tied loop, and the boundary conditions along the vertical direction are symmetric (i.e. gradients are set to 0). The plasma condensation is superimposed on the background density and temperature profiles as follows. A 2D Gaussian enhancement is added to the equilibrium density profile and is positioned at $x_0 = 0$ Mm and $s_0 = 100$ Mm, that is, below the loop apex, of width $\sigma = 0.5$ Mm and height $\rho_{\rm blob} = r_{\rm bc}\,\rho_{\rm bg}(x_0, s_0)$, with $r_{\rm bc}$ being the density contrast between the peak blob density and the density of the background loop plasma $\rho_{\rm bg}$ at the same position. We surround the condensation with a low-temperature region to maintain the plasma pressure balance and to prevent rapid initial expansion of the condensation in the vertical direction (the expansion in the transverse direction is counteracted by the magnetic Lorentz force). A grid convergence study using a grid with 1024×4096 resolution has been carried out in order to check the convergence of the numerical results.

3.3 Blob evolution and kinematics

The evolution and kinematics of the plasma condensation, or blob, is analysed in detail for a magnetic field strength ranging from 20 G to 100 G and for three values of the initial density contrast between the condensation and the coronal loop plasma $r_{\rm bc} = 10^2$, 10^3, and 10^4 corresponding to peak blob densities of 2.5×10^{-9}, 2.5×10^{-8}, and 2.5×10^{-7}kg m^{-3}, respectively. The corresponding plasma-β ranges from 0.01 to 0.3.

The evolution of the density profile of the blob during the first 5600 s is shown in Figure 3.2 for the $B = 100$ G, $r_{\rm bc} = 10^3$ case. This leads to an initial decrease of the blob density and to the emission of sound waves, most clearly seen in the case of $r_{\rm bc} = 10^4$. As the condensation falls, it develops an elongated tail as a result of the differential component of the effective gravity acting along the finite longitudinal extent of the blob. This elongation of the plasma condensations is in line with recent high-resolution coronal rain observations [e.g. Antolin and Verwichte, 2011; Antolin and Rouppe van der Voort, 2012; Kohutova and Verwichte, 2016]. The build-up of the density near the leading edge of the blob is further enhanced during the

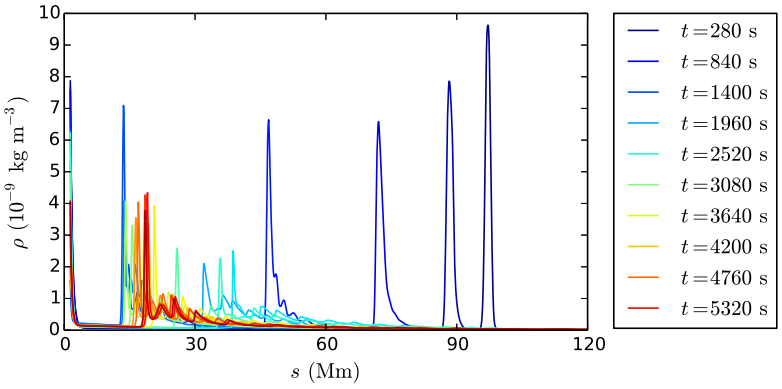

Figure 3.2: Evolution of the density profile along the bottom half of the loop plotted every 280 s during the first 500 time steps.

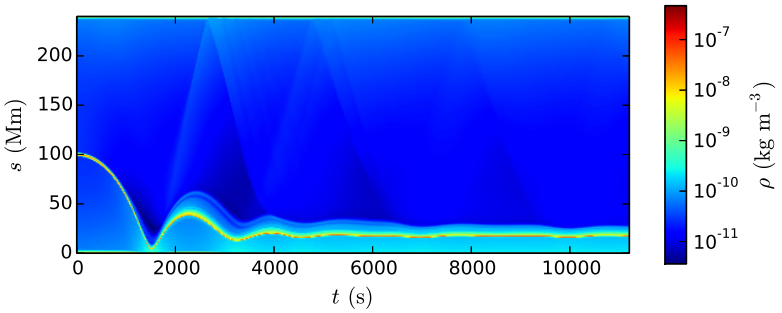

Figure 3.3: Time-distance plot of the density along s at $x = 0$ for the $r_{\rm bc} = 10^3$, $B = 100\,\mathrm{G}$ case.

deceleration phase that occurs as the blob approaches the transition region (Figure 3.2). Here the blob can be seen to rebound multiple times (Figure 3.3). When the blob hits the transition region, a rebound shock occurs that results in further sound wave emission. For low magnetic field strengths, the impact of the blob is accompanied by the ejection of chromospheric material since the finite plasma-β in the transition region and below does not restrict the transverse motion of the plasma. Except for heating the plasma along the blob edges, the overall temperature of the blob stays approximately constant during its downward motion. The temperature of the plasma below the blob increases as it is being compressed, whereas the plasma in the wake of the blob cools down. After the first rebound, the blob temperature slightly increases as a result of rebound shock dissipation.

The trajectory of the plasma condensation is determined by finding the position of the maximum in blob density along the vertical direction at each time step. This is

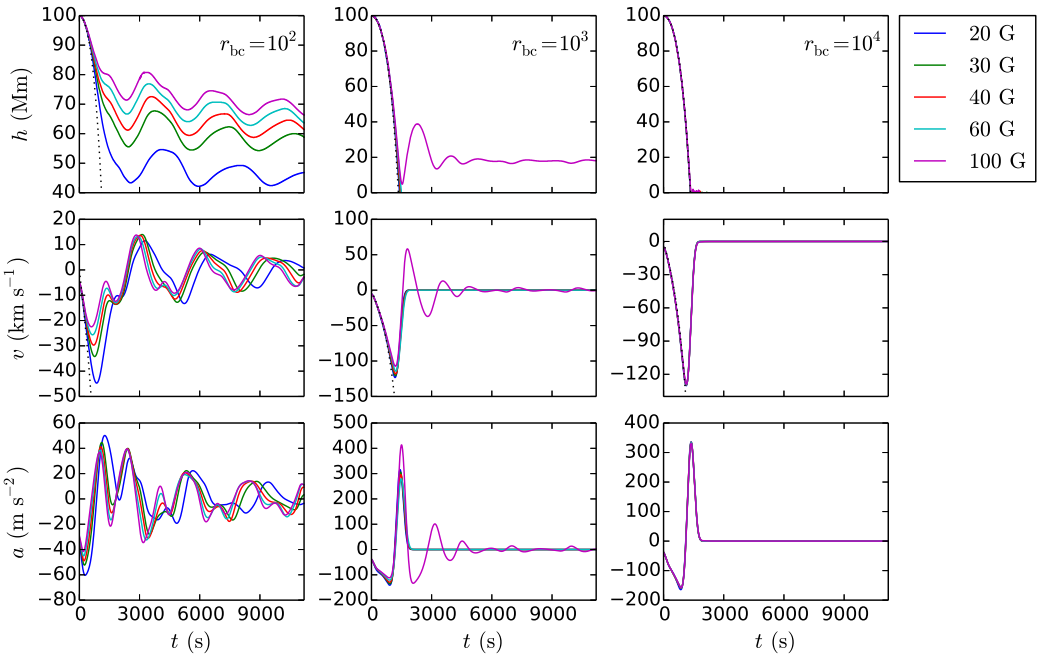

Figure 3.4: Height (top), velocity (middle), and acceleration (bottom) profiles of the condensation for different values of blob density contrast and magnitude of the magnetic field strength. The dotted line shows the free-fall height and velocity profiles.

subsequently used to deduce the evolution of the vertical velocity and acceleration. Two types of motion depending on the magnetic field strength and blob density are observed: a purely downward motion with the blob hitting the transition region, or damped oscillatory motion with the blob rebounding multiple times and eventually settling in an equilibrium position in the corona (Figure 3.4). Higher magnetic field strengths lead to greater heights of the rebound points and greater heights of the equilibrium positions around which the blob oscillates. In addition, increasing the blob density leads to a decrease of the rebound point height and to a greater number of condensations reaching the surface. Similarly, Figure 3.5 shows that the maximum downward velocity increases with increasing blob density and decreasing magnetic field strength. For $r_{\rm bc} = 10^2$, the rebound motion occurs for all values of magnetic field strengths. For $r_{\rm bc} = 10^3$, purely downward motion occurs at low magnetic field strengths, while for $r_{\rm bc} = 10^4$, no rebound motion is observed.

For the lowest blob density, the blob motion shows distinct acceleration and deceleration phases: during the first ~ 300 s the blob accelerates downwards, afterwards it decelerates to $t \sim 1000$ s, followed by another acceleration phase lasting up to

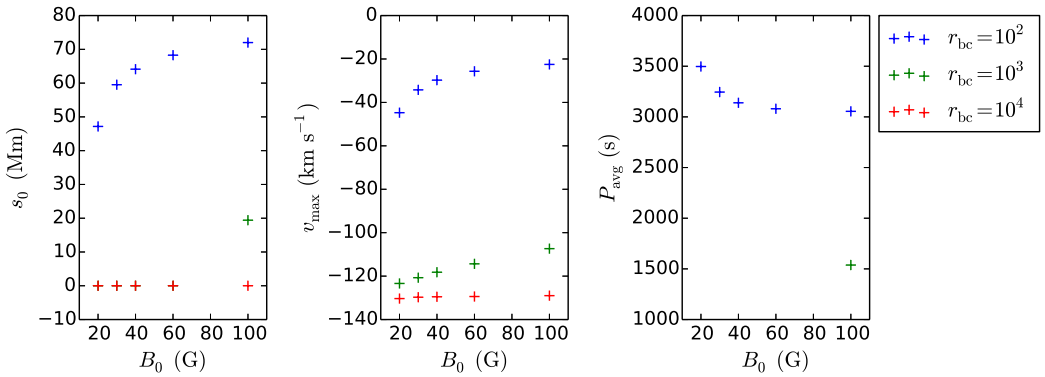

Figure 3.5: Dependence of the equilibrium height (left), maximum downward velocity (centre), and average period of blob oscillations (right) on the magnitude of the magnetic field strength for various blob densities.

$t \sim 1500$ s and so forth, with the maximum values of the downward velocity ranging from 23 km s^{-1} to 45 km s^{-1} depending on the magnetic field strength.

The distinction between acceleration and deceleration phases is similarly clear for higher blob densities. There the maximum values of downward velocities are much higher, ranging from 107 km s^{-1} to 130 km s^{-1}. The motion is sub-ballistic only in the case of lowest blob density, in the other two cases before the rebound, the blob falls approximately with free-fall speed. For the highest blob density, the effect of the varying magnetic field strength on the motion of the blob is negligible.

The motion of the coronal rain blobs deduced from high-resolution solar observations is mostly sub-ballistic with only few extreme cases [e.g. Antolin and Verwichte, 2011; Antolin and Rouppe van der Voort, 2012; Kohutova and Verwichte, 2016]. When we consider the significant effect that the peak blob density was found to have on its motion, the broad distribution of the blob velocities typically seen in the observations is therefore likely due to variations in masses of individual condensations. The extreme cases of observed velocities are likely caused by the variations in the plasma pressure across the coronal loop, for instance, when one blob travels in a wake of another, it can be siphoned into the region of the low pressure left behind by the first blob, which results in a motion that is faster than free fall [Müller et al., 2005].

3.4 Force balance analysis

In order to determine the relative influence of the individual forces on the motion and evolution of the plasma condensation, the vertical components of the gravitational force $\rho\vec{g}_{\rm eff}$, pressure gradient force $-\vec{\nabla}p$, magnetic pressure force $-\vec{\nabla}B^2/2\mu_0$, and magnetic tension force $(\vec{B}\cdot\vec{\nabla})\vec{B}/\mu_0$ were calculated inside the loop and averaged in the transverse direction to obtain the longitudinal dependence. The evolution of the force balance during the first 5600 s is shown for the $r_{\rm bc} = 10^3$, $B = 100$ G case in Figure 3.6.

For a rebounding blob, the force balance evolves as expected according to the conceptual model proposed by Mackay and Galsgaard [2001]. As the condensation falls, it compresses the coronal loop plasma below it, leading to a build-up of the pressure gradient. For a high magnetic field strength (low plasma-β), the plasma is confined by the magnetic field, and as it expands below the blob, it pulls the magnetic field lines with it. The magnitude of the magnetic field strength therefore decreases and plasma moves away from the centre of the loop, as demonstrated by the positive divergence of the plasma velocity (Figure 3.7). This results in a net upward magnetic tension force as shown in Figure 3.6 before the first rebound at t $\sim$ 1500 s. The blob rebounds upwards, and as a result of the lower pressure below the blob, the plasma now moves towards the centre of the loop, which leads to a negative plasma velocity divergence. The field lines return to their original position, and the magnitude of the magnetic field strength increases (Figure 3.7). This occurs multiple times until the blob eventually settles in an equilibrium position. The bending of the magnetic field lines is shown in Figure 3.8.

In the case of weak magnetic field, the plasma-β in the transition region is high enough to allow the plasma below the blob to be displaced sideways, which prevents the pressure build-up. Hence no rebound motion occurs, and the blob falls directly towards the solar surface.

It should be noted that the initial uniform magnetic field configuration used here leads to a zero magnetic pressure gradient. However, in an expanding flux tube configuration, this is no longer the case. In this case, the magnetic pressure gradient force would have an additional decelerating effect and would therefore lead to lower downward velocities and greater equilibrium height of the oscillating blobs. Similarly, neglecting thermal conduction very likely affects the morphology of the cool condensations without significantly affecting the condensation dynamics. Given that the thermal conduction acts predominantly along the magnetic field lines, the

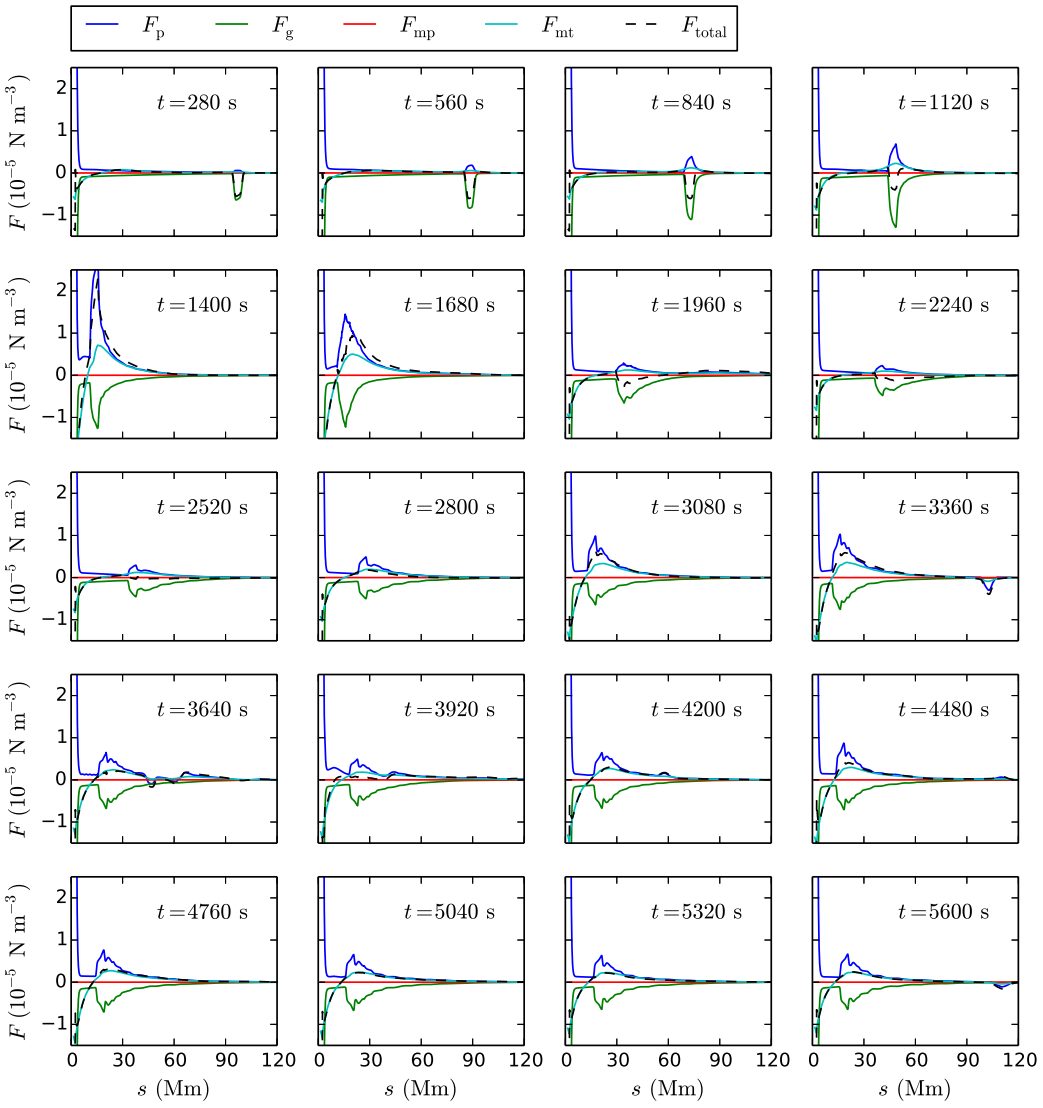

Figure 3.6: Evolution of the force balance along the bottom half of the loop plotted every 280 s during the first 500 time steps. We show the vertical components of the plasma pressure force (blue), gravity (green), magnetic pressure force (red), magnetic tension force (turquoise), and total net force in the vertical direction (black dashed line).

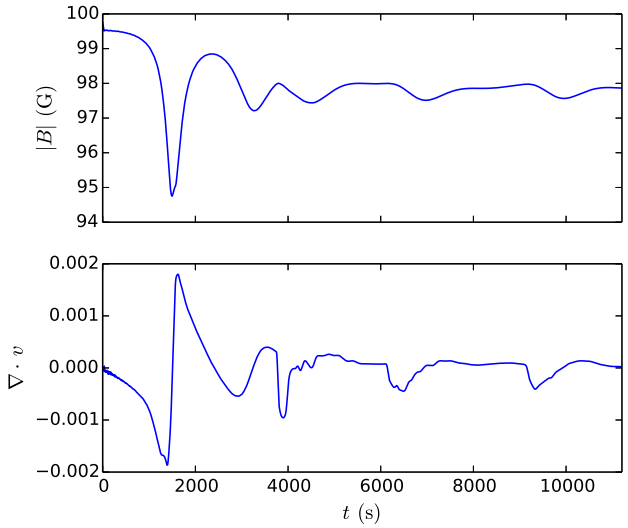

Figure 3.7: Evolution of the magnitude of the magnetic field strength (top) and velocity divergence (bottom) averaged over the region below the plasma blob for the $r_{\mathrm{bc}} = 10^3$, $B = 100$ G case.

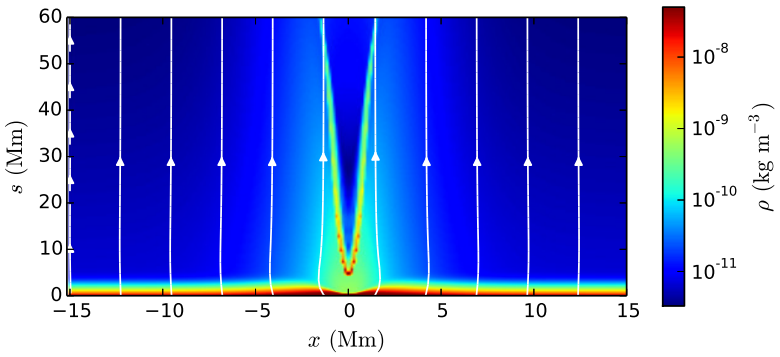

Figure 3.8: Bending of the magnetic field lines below the condensation at $t = 1523$ s for the $r_{\mathrm{bc}} = 10^3$, $B = 100$ G case.

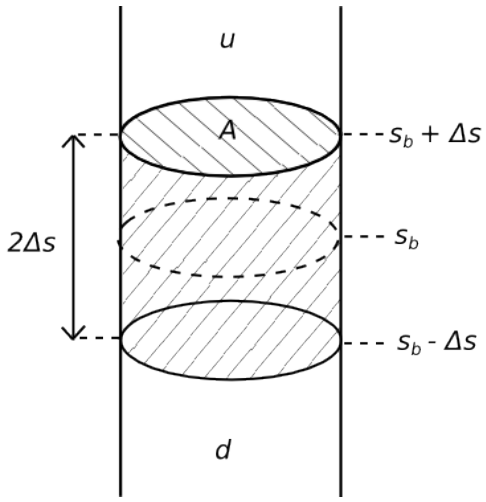

Figure 3.9: Setup of the 1D model of the blob motion, showing plasma blob with length $2\Delta s$, effective cross-section A and centre of mass at s_b, and coronal loop plasma confined above (u) and below (d) the blob.

only relevant exchange of energy will occur in the vertical direction. It is therefore not sufficient to remove significant amounts of thermal energy from the compressed underlying plasma, which would lead to large changes in plasma pressure.

3.5 Blob oscillations

We further focus on the damped oscillatory motion of the plasma blob. The period of the individual rebound phases varies strongly with the blob density, while the dependence on the magnetic field magnitude is weak (Figure 3.4). We therefore propose an analytical model for the period of the blob oscillations assuming a high β limit when the transverse motion of the plasma is prevented by the strong magnetic field in the vertical direction. We model a falling rain blob as a piston problem, where the rain blob is a piston compressing gas below it. We use a 1D model with s as the spatial coordinate along the loop. The rain blob has a fixed length $2\Delta s$ and its centre of mass is located at the position $s_\mathrm{b}(t)$ (Figure 3.9). Its equation of motion is

$$m\frac{\mathrm{d}^2 s_\mathrm{b}}{\mathrm{d}t^2} \;=\; -mg(s_\mathrm{b}) - \left[p_\mathrm{u}(s_\mathrm{b}+\Delta s) - p_\mathrm{d}(s_\mathrm{b}-\Delta s)\right] A \;, \tag{3.7}$$

where m is the blob mass, A is the effective cross-section of the blob, and $g(s)$ is the solar gravitational acceleration along a semi-circular loop, that is, $g(s) = g_\odot \cos(\pi s/L)$. It is measured at the blob's centre of mass. In order to be able to

solve the problem analytically, in the subsequent steps we neglect the stratification of the plasma. $p_{\rm d}(s_{\rm b}-\Delta s)$ is the plasma pressure of the plasma below the blob, measured at the lower interface with the blob at $s{=}s_{\rm b}-\Delta s$; $p_{\rm u}(s_{\rm b}+\Delta s)$ is the plasma pressure of the plasma above the blob, measured at the upper interface with the blob at $s{=}s_{\rm b}+\Delta s$.

The blob is in equilibrium at position s_0. We assume that there is no exchange of mass between the background plasma. Subsequently, the plasma masses above and below are conserved, and we may write the equilibrium densities as

$$\rho_{\rm u0} \,=\, \frac{M_{\rm u}}{(L-s_0-\Delta s)A} \;,\; \rho_{\rm d0} \,=\, \frac{M_{\rm d}}{(s_0-\Delta s)A} \;. \tag{3.8}$$

This allows us to rewrite the equilibrium pressures as

$$p_{\rm d0} \,=\, \frac{k_{\rm B}T_{\rm d0}M_{\rm d}}{\tilde{m}(s_0-\Delta s)A} \;,\; p_{\rm u0} \,=\, \frac{k_{\rm B}T_{\rm u0}M_{\rm u}}{\tilde{m}(L-s_0-\Delta s)A} \;. \tag{3.9}$$

Then, the equilibrium position of the blob is the solution of the transcendental equation

$$g_\odot \cos\left(\frac{\pi s_0}{L}\right) \,=\, -\frac{k_{\rm B}T_{\rm u0}M_{\rm d}}{\tilde{m}(L-s_0-\Delta s)m} + \frac{k_{\rm B}T_{\rm d0}M_{\rm u}}{\tilde{m}(s_0-\Delta s)m} \;. \tag{3.10}$$

We introduce the lower density scale height H and sound speed $C_{\rm Sd}$ defined as

$$H \,=\, \frac{k_{\rm B}T_{\rm d0}}{\tilde{m}g_\odot} \;,\; C_{\rm Sd} \,=\, \sqrt{\frac{\gamma k_{\rm B}T_{\rm d0}}{\tilde{m}}} \;, \tag{3.11}$$

and the following dimensionless variables

$$\begin{aligned} \theta_0 \;&=\; \frac{\pi s_0}{L} \;,\; \Delta\theta \,=\, \frac{\pi\Delta s}{L} \;,\; \theta_1 \,=\, \pi - \Delta\theta \;, \\ h \;&=\; \frac{\pi H}{L} \;,\; \nu \,=\, \frac{T_{\rm u0}}{T_{\rm d0}} \;. \end{aligned} \tag{3.12}$$

Subsequently, Eq. (3.10) may be rewritten in dimensionless form as

$$\cos\theta_0 \,=\, \frac{M_d}{m}\,\frac{h}{(\theta_0-\Delta\theta)} + \frac{M_u}{m}\,\frac{\nu h}{(\theta_0-\theta_1)} \;. \tag{3.13}$$

We linearise the equation of motion by considering small amplitude oscillations around the equilibrium position s_0, found by solving Eq. (3.10), such that $s = s_0{+}s_1$

with $|s_1| \ll L$. Hence,

$$\begin{aligned} m\frac{\mathrm{d}^2 s_1}{\mathrm{d}t^2} &= -m\,\frac{\mathrm{d}g}{\mathrm{d}s}(s_0)\,s_1 \\ &- \left[\frac{\partial p_{\mathrm{u}0}}{\partial s}(s_0+\Delta s) - \frac{\partial p_{\mathrm{d}0}}{\partial s}(s_0-\Delta s)\right] s_1\,A \\ &- \left[p_{\mathrm{u}1}(s_0+\Delta s) - p_{\mathrm{d}1}(s_0-\Delta s)\right]\,A\,, \end{aligned} \tag{3.14}$$

where p_1 is the linear perturbation of plasma pressure. The linear plasma displacement parallel to the equilibrium magnetic field ξ is governed by

$$\rho_0 \frac{\partial^2 \xi}{\partial t^2} = -\frac{\partial p_1}{\partial s}\,, \tag{3.15}$$

where ρ_0 is the equilibrium plasma density, which we assumed to be uniform. Furthermore, this displacement satisfies the boundary conditions

$$\xi(0,t) = 0\,,\; \xi(s_0-\Delta s,t) = s_1(t)\,,\; \xi(s_0)+\Delta s,t) = s_1(t)\,, \tag{3.16}$$

and is allowed to propagate in the upper region. We find

$$\xi(s,t) = \begin{cases} s_1(t)\,\frac{\sin(k_{\mathrm{d}}s)}{\sin(k_{\mathrm{d}}(s_0-\Delta s))} & 0 \le s \le s_0-\Delta s \\ s_1(t)\,\frac{\exp(ik_{\mathrm{u}}s)}{\exp(ik_{\mathrm{u}}(s_0+\Delta s))} & s \ge s_0+\Delta s \end{cases}\,, \tag{3.17}$$

where k_{d} and k_{u} are the wave numbers in the lower and upper regions, respectively. The corresponding pressure perturbation is found from Eq. (3.15):

$$p_1(s,t) = \begin{cases} \frac{\mathrm{d}^2 s_1}{\mathrm{d}t^2}\,\frac{1}{k_{\mathrm{d}}}\,\frac{M_d}{(s_0-\Delta s)A}\,\frac{\cos(k_{\mathrm{d}}s)}{\sin(k_{\mathrm{d}}(s_0-\Delta s))} \\ \frac{\mathrm{d}^2 s_1}{\mathrm{d}t^2}\,\frac{i}{k_{\mathrm{u}}}\,\frac{M_u}{(L-s_0-\Delta s)A}\,\frac{\exp(ik_{\mathrm{u}}s)}{\exp(ik_{\mathrm{u}}(s_0+\Delta s))} \end{cases}\,. \tag{3.18}$$

Equations (3.9) and (3.18) are substituted into Eq. (3.14):

$$\begin{aligned} \frac{\mathrm{d}^2 s_1}{\mathrm{d}t^2} &= \frac{\pi g_\odot}{L}\,\sin\left(\frac{\pi s_0}{L}\right)\,s_1 \\ &- \frac{M_d}{m}\,\frac{k_{\mathrm{B}}T_{\mathrm{d}0}}{\tilde{m}}\,\frac{s_1}{(s_0-\Delta s)^2} \\ &+ \frac{M_d}{m}\,\frac{1}{k_{\mathrm{d}}}\,\frac{1}{(s_0-\Delta s)}\cot(k_{\mathrm{d}}(s_0-\Delta s))\,\frac{\mathrm{d}^2 s_1}{\mathrm{d}t^2} \\ &- \frac{M_u}{m}\,\frac{k_{\mathrm{B}}T_{\mathrm{u}0}}{\tilde{m}}\,\frac{s_1}{(L-s_0-\Delta s)^2} \\ &- \frac{M_u}{m}\,\frac{i}{k_{\mathrm{u}}}\,\frac{1}{(L-s_0-\Delta s)}\,\frac{\mathrm{d}^2 s_1}{\mathrm{d}t^2}\,, \end{aligned} \tag{3.19}$$

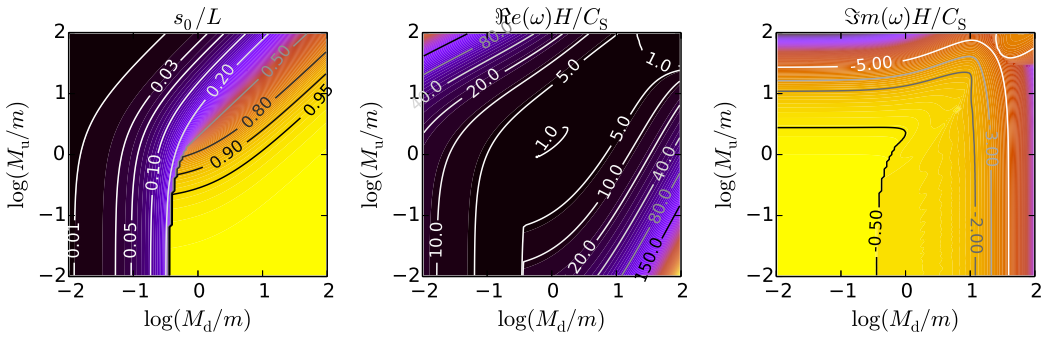

Figure 3.10: Solutions for the equilibrium position normalised by the loop length (left), and for the real and imaginary part of the normalised frequency of the blob oscillations (centre and right) as a function of loop-to-rain plasma mass ratios.

for which normal mode solutions of the form $s_1(t) \sim \exp(-i\omega t)$ are sought. Equation (3.19) then turns into a dispersion relation for ω. We introduce the additional dimensionless variables

$$\Omega = \frac{\omega H}{C_{\rm Sd}} \ , \ K_{\rm d} = k_{\rm d} H \ , \ K_{\rm u} = k_{\rm u} H \sqrt{\nu} \ . \tag{3.20}$$

Equation (3.19) becomes in dimensionless form

$$\begin{aligned} \Omega^2 \ &= \ \frac{h}{\gamma}\left[-\sin\theta_0 + \frac{M_d}{m}\frac{h}{(\theta_0-\Delta\theta)^2} + \frac{M_u}{m}\frac{\nu h}{(\theta_0-\theta_1)^2}\right] \\ &+ \ \Omega^2 h\left[\frac{M_d}{m}\frac{\cot\left(\frac{K_{\rm d}(\theta_0-\Delta\theta)}{h}\right)}{K_{\rm d}(\theta_0-\Delta\theta)} + i\frac{M_u}{m}\frac{\sqrt{\nu}}{K_{\rm u}(\theta_0-\theta_1)}\right]. \end{aligned} \tag{3.21}$$

Here $\Re e(\omega)$ determines the angular frequency of the blob oscillations and $-1/\Im m(\omega)$ sets the e-folding time for the damping due to wave radiation. Lastly, a dispersion relation is required in the two plasma regions to be able to connect $K_{\rm d}$ and $K_{\rm u}$ with ω. For a slow magnetoacoustic sausage mode, we find k in each region, defined by the solution to the dispersion relation [Edwin and Roberts, 1983]:

$$\frac{\kappa_{is}}{(\omega^2 - v_{\rm Ai}^2 k^2)}\frac{\mathcal{I}_0'(\kappa_{is}a)}{\mathcal{I}_0(\kappa_{is}a)} = \left(\frac{\rho_{0es}}{\rho_{0is}}\right)\frac{\kappa_{es}}{(\omega^2 - v_{\rm Ae}^2 k^2)}\frac{\mathcal{K}_0'(\kappa_{es}a)}{\mathcal{K}_0(\kappa_{es}a)}, \tag{3.22}$$

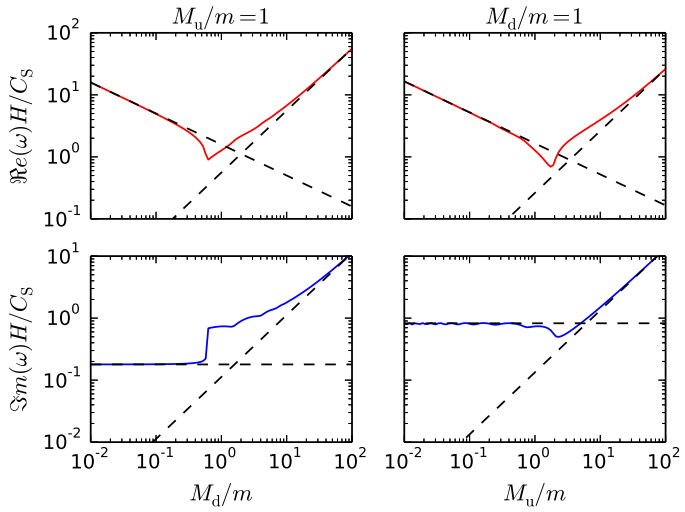

Figure 3.11: Horizontal (left) and vertical (right) cuts trough plots of the dependence of the angular frequency on the loop-to-rain mass ratio. Dashed lines mark the limit cases.

with the squared radial wave number

$$\kappa_{ps}^2 = \frac{(\omega^2 - C_{Sps}^2 k^2)(\omega^2 - v_{Ap}^2 k^2)}{(C_{Sps}^2 + v_{Ap}^2)(\omega^2 - c_{Tps}^2 k^2)} , \tag{3.23}$$

where $a = \sqrt{A}/\pi$ is the loop cross-section radius, v_A the Alfvén speed, c_T the tube speed, and $s \in \{d, u\}$, $p \in \{i, e\}$. index i (e) refers to internal (external) conditions to the loop. The density contrast and Alfvén speed are assumed to be identical in the lower and upper regions. $\mathcal{I}_0(x)$ and $\mathcal{K}_0(x)$ are the modified Bessel functions of the first and second kind, respectively. We further note that the oscillation seen in the simulations is essentially a slow magnetoacoustic sausage mode. We solve for the fundamental radial mode with the phase speed in the interval $[c_T, c_S]$. For $ka \ll 1$ the solution is approximately $k \approx \omega/C_{Ti}$.

This is also true for a slab geometry as used in the numerical simulations. Furthermore, for the range of values of density, temperature, and magnetic field strength, the tube speed varies from the sound speed by less than 10%. Therefore, it is reasonable to describe the mode with the dispersion relation of a one-dimensional acoustic mode with $k = \omega/C_{Si}$. Then, $K_d = K_u = \Omega$. Equation (3.21) is solved numerically together with the equilibrium Eq. (3.13) and the corresponding dispersion relation. We solve Equations (3.13) and (3.21) for a range of loop-to-rain mass ratios.

Table 3.1: Blob oscillation parameters

$r_{\rm bc}$	B(G)	$M_{\rm d}/m$	$M_{\rm u}/m$	$s_{\rm 0sim}$ (Mm)	$s_{\rm 0A}$ (Mm)	$P_{\rm sim}$ (s)	$P_{\rm A}$ (s)
10^2	20	3.73	7.55	47 ± 4	103 ± 7	3497 ± 100	2344 ± 100
10^2	30	3.00	4.86	60 ± 4	116 ± 10	3245 ± 100	2805 ± 200
10^2	40	3.13	4.83	64 ± 4	120 ± 10	3139 ± 70	2830 ± 200
10^2	60	3.16	4.59	68 ± 4	123 ± 7	3080 ± 40	2869 ± 200
10^2	100	3.35	4.82	72 ± 4	123 ± 6	3055 ± 10	2818 ± 300
10^3	100	0.31	1.81	19 ± 1	40 ± 6	1538 ± 200	1393 ± 200

Blob equilibrium positions and average oscillation periods determined from the simulation ($s_{\rm 0sim}$, $P_{\rm sim}$) and using the analytical model ($s_{\rm 0A}$, $P_{\rm A}$) for different values of blob density and magnetic field strength.

There is a discontinuity in the solution for the equilibrium position of blob from one loop leg to the other in the case of a high mass of plasma that is confined below the blob and a low mass of the plasma in the rest of the loop (Figure 3.10). This discontinuity then further propagates into the solutions for $\Re e(\omega)$ and $\Im m(\omega)$, resulting in discontinuity in the gradient. This is not likely to occur in a real gravitationally stratified loop that is initially symmetric, however, unless there is a direct mass injection occurring into one loop leg alone.

We further focus on the behaviour of the oscillation parameters in limit cases. In high M/m limit (no coronal rain) both $\Re e(\omega)$ and $\Im m(\omega)$ increase linearly with M/m. In low M/m limit (no coronal plasma) $\Re e(\omega)$ decreases with $\sqrt{M/m}$ while $\Im m(\omega)$ remains constant (Figure 3.11). Assuming realistic values of the loop-to-rain mass ratio are of the order of 1-10, the corresponding solutions for $\Re e(\omega)$ and $\Im m(\omega)$ are of the order of 0.001, or equivalently 1000 s for the period and damping scaling time.

The comparison of blob oscillation periods determined from the simulation and periods predicted by the analytical model is shown in Table 3.1. We determine the loop-to-rain mass ratios (serving as an input for the analytical model) from the final simulation snapshot at $t = 11200$ s, which we assume to be the best representation of the equilibrium state. The blob mass is determined by integrating the plasma density between blob boundaries, and the mass of the coronal loop plasma above and below the blob is determined by integrating the density between the blob boundary and loop footpoints while excluding the high-density chromosphere layer. Estimates of uncertainties in the parameters predicted by the analytical model are determined

assuming 20% uncertainty on the position of blob boundaries. The agreement between the two is best for higher blob density and for high values of the magnetic field strength. This is as expected given the limitations of the analytical model. It should be noted that the analytical model considerably overestimates the height of the equilibrium position in the case of the lowest blob density. The equilibrium position predicted by the analytical model is heavily dependent on the input loop-to-rain mass ratios. In the low-density case, these are inherently more difficult to determine accurately from the simulation because we lack a well-defined upper boundary of the plasma blob. Here the elongated tail of the blob accounts for a higher fraction of the total blob mass than in the higher density cases. The low-density blob is also more sensitive to sound waves that are reflected from the boundaries (the analytical model neglects the presence of the upper domain boundary and assumes a radiating solution above the blob). The validity of the analytical periods and damping times in the $r_{\mathrm{bc}} = 10^2$ case is therefore also limited.

Similarly, the agreement between the analytical model and the simulation is worse for cases with lower magnetic field strength when the plasma below the blob is less constrained in the transverse direction and hence allowed to expand, whereas the model explicitly assumes a constant loop cross-section. This also means that while the blob oscillates, transfer of plasma can occur from the lower loop leg to the region above the blob, thus invalidating the assumption of a piston-like behaviour. However, when we use the values corresponding to the case with $B = 100$ G and $r_{\mathrm{bc}} = 10^3$, which best adheres to assumptions made by the analytical model, this results in the predicted period of 1393 s and a damping scaling time of 1695 s, which corresponds to about three clearly observable oscillation periods. This is in good agreement with the simulation results.

3.6 Discussion and conclusions

The motion and evolution of plasma condensations were found to be strongly affected by the pressure of the coronal loop plasma, and the pressure gradients can be high enough to account for the lower-than-free-fall speed of the coronal rain even in finite magnetic field cases. The fastest downward velocities are in agreement with recent coronal rain observations. High coronal magnetic field strength or a low mass of the condensations can lead to oscillatory motion consisting of multiple rebounds damped through sound wave emission, with the condensation eventually settling in an equilibrium position supported by the pressure of the underlying plasma.

Rebounding of the condensation is due to a combined effect of the pressure gradient force and the magnetic tension force that results from bending of the magnetic field lines in the lower part of the coronal loop. The period and damping scaling time of the oscillatory motion are consistent with values determined using an analytical model for the balance of forces that act on the condensation.

Although the majority of coronal rain condensations are observed to fall directly towards the solar surface, the individual blobs are sometimes observed to longitudinally oscillate up and down before falling, as show in Chapter 2. This loss of equilibrium has not been accounted for in our simulations and could be due to the change in mass of the coronal loop plasma that supports the blob or due to presence of other condensations. It should further be noted that in the non-equilibrium scenario, siphon flows caused by pressure differences in the loop can significantly affect the motion of the condensations, sometimes completely overriding the effects of the plasma pressure gradient and magnetic tension force addressed here.

The analytical model also highlights the fact that the dynamics of the plasma condensations (i.e. presence or lack of oscillatory motion and oscillation parameters) is determined by the loop-to-rain mass ratio. There is still considerable uncertainty about what fraction of the total mass of the coronal loop plasma condenses into coronal rain after catastrophic cooling takes place; current estimates of the loop-to-rain mass ratio from observations are in the order of 1 - 10 [Antolin et al., 2015b]. These estimates are subject to the spatial resolution limits of the instruments, however, it is therefore likely that a significant fraction of the condensation mass remains undetected.

The longitudinal oscillations of the coronal rain blobs were typically observed in transversely oscillating coronal loops [Verwichte et al., 2017a]. This means that the action of the ponderomotive force that is due to transverse oscillations should be taken into account [Terradas and Ofman, 2004]. It has been proposed that the ponderomotive force can in fact affect the motion of the coronal rain condensations; however, typical amplitudes of the transverse loop oscillations are not sufficient to fully explain the observed oscillatory motion and sub-ballistic fall rates of coronal rain on their own [Verwichte et al., 2017a]. The ponderomotive force may still play a non-negligible role in the condensation dynamics, however, in addition to the effects of the coronal plasma pressure gradients and magnetic field effects addressed in this chapter. This is further supported by the fact that the oscillatory behaviour of coronal rain is usually observed near the loop top, and it suggests that the force that counteracts the motion under the gravity has a maximum near the loop apex,

whereas the pressure gradient force was found to have greatest effect on the condensations in the lower part of the loop legs.

Chapter 4

Excitation of vertical coronal loop oscillations by plasma condensations and flows

Contents of this chapter have been published in Kohutova and Verwichte [2017b] and Kohutova and Verwichte [2018].

4.1 Introduction

Coronal loops are commonly subject to transverse oscillations [e.g. Aschwanden et al., 1999; Nakariakov et al., 1999; Verwichte et al., 2004; White and Verwichte, 2012]. The basic properties of observed transverse oscillations can be modelled by assuming a homogeneous flux tube model [Nakariakov and Verwichte, 2005]. This approximation works reasonably well for predicting basic oscillation characteristics such as fundamental mode period; however, for more complex oscillatory loop behaviour the effects of the density variation within the loop should be considered.

The effect of longitudinal density stratification on the period and spatial structure of the fundamental kink mode has been studied for straight flux-tube coronal loop models [Andries et al., 2005a,b; Dymova and Ruderman, 2005, 2006]. For line-tied flux tubes, the effect of the density structuring on the fundamental kink mode properties is most significant when it is located near the loop apex and almost negligible in the case of the density structuring near the loop footpoints [Díaz et al., 2006].

The transverse loop oscillations have been observed to occur in two polarisations; horizontal [Aschwanden et al., 2002; Schrijver et al., 2002] and vertical [Wang and Solanki, 2004; Mrozek, 2011; White et al., 2013]. The horizontally polarised oscillations are typically excited by a nearby flare [e.g. Aschwanden et al., 1999; Verwichte et al., 2004], while the source of excitation of the vertical oscillations remains unclear. They are usually explained by placing an external driver below the loop, by the reconnection process or by footpoint motion [Brady and Arber, 2005; Gruszecki and Murawski, 2008; Selwa et al., 2010; White et al., 2013]. Subsonic siphon flows have also been proposed as a possible excitation mechanism [Ofman et al., 2012].

Given that many coronal loops are subject to thermal instability undergoing catastrophic cooling, as shown by recent observations [Antolin and Rouppe van der Voort, 2012], a significant fraction of loops are likely to contain an overdense region in the part of the loop where the condensation occurs which is typically near the loop apex. As shown in Chapter 2, small amplitude transverse oscillations are often present in rainy coronal loops, with the observed loops in question typically tilted with respect to the photospheric normal [Antolin and Verwichte, 2011; Verwichte and Kohutova, 2017].

A 1D mechanical model for the excitation of small amplitude transverse oscillations by the coronal rain condensations via their concentrated mass was proposed by Verwichte et al. [2017a]. These authors also showed that small amplitude transverse oscillations analysed in Chapter 2 could be excited by the coronal rain. In the special case of a coronal loop lying in a plane perpendicular to solar surface, this mechanism would lead to the excitation of oscillation polarised in vertical direction only.

The first observational evidence of excitation and evolution of vertical coronal loop oscillations caused by catastrophic cooling and coronal rain formation was shown in Verwichte and Kohutova [2017]. The observations presented therein also showed a change of the oscillation period over the duration of the loop evolution caused by the drainage of the coronal loop mass by the coronal rain.

In the following study we carry out 2.5D MHD simulations of a coronal loop with cool plasma condensation region at the loop apex in order to investigate the possibility of the excitation of transverse loop oscillations by the mass of the condensation plasma. We also look for signatures of shift in the fundamental kink mode period previously seen in coronal rain observations by Verwichte and Kohutova [2017].

In addition, we investigate effects of plasma flows on the coronal loop. High speed

plasma flows are ubiquitous in the solar corona. Flow velocities are measured by Doppler shifts in the spectral data in the case of line-of-sight motions and by feature tracking using imaging data when the motion is perpendicular to the line of sight. Sub-Alfvénic flows with speeds around 100 km s^{-1} are the most common, with faster flows sporadically occurring in the vicinity of energetic events such as CMEs or in flaring regions [Innes et al., 2001, 2003; Harra et al., 2005]. Unidirectional flows along the coronal loop from one footpoint to the other caused by the pressure difference between the footpoints are known as siphon flows and multiple analytical solutions for which exist for non-hydrostatic coronal loops [Cargill and Priest, 1980; Mariska and Boris, 1983; Orlando et al., 1994]. Siphon flows were observed in imaging data by TRACE [Doyle et al., 2006] and STEREO [Tian et al., 2009] as well as by using Doppler shifts in spectral data by SOHO/SUMER and Hinode/EIS [Teriaca et al., 2004; Tian et al., 2008]. They are also often seen in simulations of coronal loop dynamics and evolution, often in the response to the asymmetric footpoint heating of the coronal loop [McClymont and Craig, 1987; Mariska, 1988], or as a result of internal pressure gradients in the loop following the onset of thermal instability and coronal rain formation [Fang et al., 2013, 2015].

The interplay between flows and coronal loop oscillations is twofold. Presence of a steady flow in a uniform flux tube modifies the oscillation profile and increases the period of the fundamental harmonic [Terradas et al., 2011]. Conversely, flows in a coronal loop can lead to excitation of a variety of magnetoacoustic modes as shown in Ofman et al. [2012], who studied excitation of slow and fast mode oscillations in a coronal loop with high speed inflow driven either continuously or periodically. The main effect of the flow was to excite damped slow magnetoacoustic modes propagating along the loop. They also observed excitation of an oscillation mainly in the plane of the loop in the direction parallel to solar surface with the displacements of both loop legs in phase, with properties similar to the second harmonic of a vertical kink mode. It was suggested here that the oscillations are excited by the momentum of the initial pulse and the centrifugal force. We therefore carry out 2.5 MHD simulations of a coronal loop with an impulsive flow triggered by the pressure difference between the footpoints to investigate the possibility of the excitation of transverse loop oscillations by fast moving plasma.

The chapter is structured as follows. Section 4.2 describes the numerical setup used to study evolution of a coronal loop arcade embedded in a realistically stratified atmosphere. In Section 4.3 we study the excitation of transverse loop oscillations by plasma condensations. The presence of a dense condensation region near the loop

apex is found to excite sustained, small amplitude, vertically polarised transverse loop oscillations. We analyse the oscillation parameters as a function of condensation region mass and calculate the expected change in the period of the fundamental mode due to changing density profile along the loop, which is a result of the condensations falling down towards the loop footpoints under the influence of gravity. In Section 4.4 we investigate excitation of transverse loop oscillations by an impulsive flow triggered by the pressure difference between the footpoints and show that the excitation is primarily caused by the centrifugal force due to plasma moving along curved magnetic field lines. We also investigate the dependence of the oscillation amplitude on the kinetic energy of the fast-flowing material and deduce conditions under which are the flow-excited oscillations observable. Section 4.5 contains detailed discussion of the simulation results and their implications.

4.2 Numerical model

We solved the nonlinear MHD equations using Lare2d [Arber et al., 2001] assuming perfectly ionised, fully conductive plasma and using the ideal equation of state. We included the effect of gravity and shock viscosity. The role of shock viscosity is to introduce dissipation at strong gradients only, preventing false oscillations behind the shock that would arise from applying second order accurate finite difference scheme when the pressure difference exceeds the jump condition. Thermal conduction and radiative transport terms were not included in the energy equation. The equations were solved on a square, uniform 1024×1024 grid with the extent -100 Mm $\leqslant x \leqslant 100$ Mm in horizontal direction and 0 Mm $\leqslant y \leqslant 200$ Mm in the vertical direction. Grid convergence study has been carried out in order to check the convergence of the numerical results. We set up the problem so as to represent a relatively long coronal loop embedded in a magnetic arcade which contains a high-density, low-temperature condensation region at its apex (Figure 4.1). The gravity was assumed to be uniform and along negative y-direction. Both the coronal loop and the ambient plasma are gravitationally stratified.

The equilibrium magnetic field is given by a current-free magnetic arcade model determined by the potential $\vec{A} = -B_0 H_\mathrm{B} \cos(x/H_\mathrm{B}) \mathrm{e}^{(-y/H_\mathrm{B})} \hat{\vec{z}}$ [Priest, 1982] such that the magnetic field components are given by:

$$(B_x, B_y, B_z) = B_0[\cos(x/H_\mathrm{B}), -\sin(x/H_\mathrm{B}), 0]\mathrm{e}^{-y/H_\mathrm{B}}\,, \tag{4.1}$$

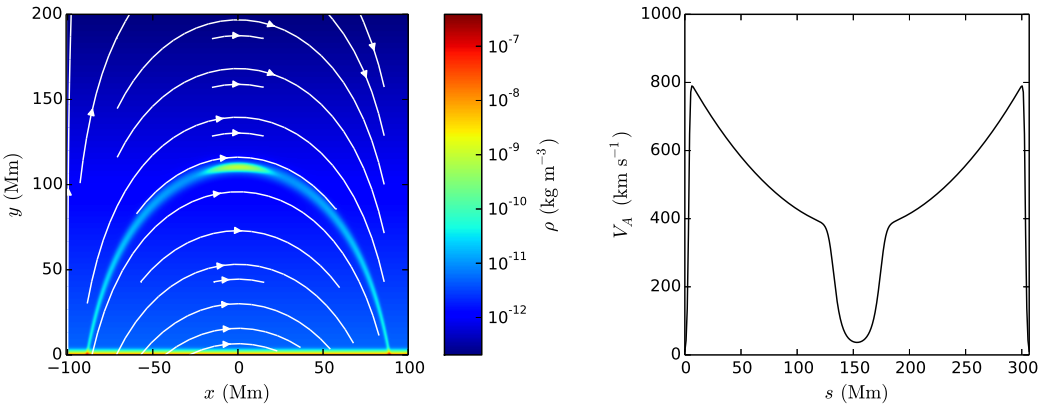

Figure 4.1: Left: Initial density configuration of the coronal loop with cool condensation region for $\mu = 0.7$. The white lines show the B-field direction. Right: Alfvén speed profile along the centre of the coronal loop.

where H_B is the magnetic scale height given by $H_\mathrm{B} = W/\pi$ with $W = 200\,\mathrm{Mm}$ being the horizontal extend of the arcade and $B_0 = 70\,\mathrm{G}$ is the magnetic field at $y = 0$. This results in the magnetic field of ~ 20 G at coronal heights, which is representative of real coronal conditions.

We assumed the background temperature to be constant in the x-direction and in the y-direction we create a smoothed step function temperature profile representative of an atmosphere consisting of a cool chromosphere, transition region layer and hot corona [Cargill et al., 1997]:

$$T(y) = \frac{1}{2}(T_\mathrm{cor} + T_\mathrm{ph}) + \frac{1}{2}(T_\mathrm{cor} - T_\mathrm{ph}) \tanh\left(\frac{y - y_\mathrm{t}}{\Delta y}\right), \tag{4.2}$$

with photospheric temperature $T_\mathrm{ph} = 6 \times 10^3$ K, coronal temperature $T_\mathrm{cor} = 10^6$ K, $y_\mathrm{t} = 4$ Mm and $\Delta y = 1$ Mm. The temperature variation controls the pressure scale height $\Lambda(y)$:

$$\Lambda(y) = \frac{k_b T(y)}{m g_\odot}, \tag{4.3}$$

where $g_\odot = 274\,\mathrm{m\,s^{-2}}$ is the average solar surface gravity and m is the mean particle mass. The density profile for the non-isothermal stratified atmosphere is then determined by numerically solving for a hydrostatic pressure balance:

$$p(y) = p_0 \exp\left(-\int_0^y \frac{dy'}{\Lambda(y')}\right), \quad \rho(y) = \frac{mp(y)}{k_b T(y)}. \tag{4.4}$$

The coronal loop was modelled as a density enhancement along a magnetic field line

defined by:

$$y_{\mathrm{L}}(x) = \frac{1}{2} H_{\mathrm{B}} \left[\ln \left(\frac{\cos(x/H_{\mathrm{B}})}{\cos(h/H_{\mathrm{B}})} \right) + \ln \left(\frac{\cos(x/H_{\mathrm{B}})}{\cos((h-a)/H_{\mathrm{B}})} \right) \right], \tag{4.5}$$

where $h = 90\,\mathrm{Mm}$ and $a = 3\,\mathrm{Mm}$ is the loop scale width. The density variation between the loop and the background medium is given by the symmetric Epstein profile [Nakariakov and Roberts, 1995]:

$$\rho(x,y) = \rho_{\mathrm{e}}(x,y) + (\rho_{\mathrm{i}}(x,y) - \rho_{\mathrm{e}}(x,y)) \operatorname{sech}^2 \left(\frac{(y - y_{\mathrm{L}}(x))}{a} \right), \tag{4.6}$$

where ρ_{e} and ρ_{i} are external and internal densities respectively. We assumed a constant density contrast $\chi = \rho_{\mathrm{i}}/\rho_{\mathrm{e}} = 10$ along the whole loop. The density stratification was calculated using base density $\rho_0 = \rho_{\mathrm{e}}(y = 0) = 5 \times 10^{-8}$ kg m^{-3}, resulting in a density in the upper half of the loop of the order of 10^{-11} kg m^{-3}, that is, representative of coronal values. The bottom domain boundary was fixed to create a line-tied loop and the boundary conditions along the remaining three boundaries are symmetric (i.e. gradients set to zero).

4.3 Excitation of vertical loop oscillations by plasma condensations

The plasma condensation region was represented as a density enhancement superimposed on top of the equilibrium density profile, accompanied by the corresponding low temperature region necessary to maintain the plasma pressure balance and to prevent rapid initial expansion. The two-dimensional (2D) Gaussian density enhancement is positioned at $x_0 = 0$ Mm and $y_0 = y_{\mathrm{L}}(x_0)$ and has widths $\sigma_{\mathrm{x}} = 7$ Mm in horizontal direction and $\sigma_{\mathrm{y}} = 1$ Mm in vertical direction and height $\rho_{\mathrm{blob}} = r_{\mathrm{bc}} \rho_{\mathrm{bg}}(x_0, y_0)$, with r_{bc} being the density contrast between the peak condensation density and the density ρ_{bg} of the hot background plasma at the loop axis at the same position in height.

Without the presence of the condensation region, the whole system is in near-equilibrium state (it should be noted that we are not explicitly forcing plasma pressure balance inside and outside of the coronal loop, this is however negligible, since the plasma-β is small and the magnetic pressure dominates, preventing loop expansion). The finite mass of the condensation region, however, displaces the axis of the coronal loop downwards which triggers vertically polarised transverse

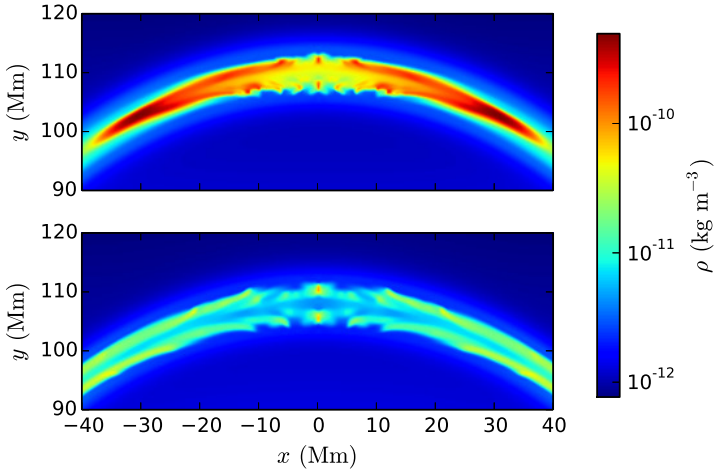

Figure 4.2: Top: Ripples due to Rayleigh-Taylor instability formed at the interface between the condensation region and ambient coronal plasma near at the top of the loop at $t = 5544$ s. Bottom: Subsequent fragmentation of tails of downfalling plasma condensations at $t = 6720$ s.

loop oscillations.

The excitation of the vertical oscillations is studied for six different values of peak density of the condensation region, with the density contrast ranging from $r_{\rm bc} = 10$ ($\rho = 9.2 \times 10^{-11}$ kg m^{-3}) to $r_{\rm bc} = 200$ ($\rho = 1.8 \times 10^{-9}$ kg m^{-3}). This corresponds to fraction of rain mass relative to total loop mass including rain ranging from $\mu = 0.19$ to $\mu = 0.83$.

Initially, the loop top is displaced downwards by the mass of the condensation region, resulting in onset of a vertically polarised transverse loop oscillation. For low condensation region densities ($\mu = 0.19$ to $\mu = 0.54$) the cool plasma is confined to the loop top by combination of the pressure from the underlying plasma and the ponderomotive force resulting from the loop oscillations directed towards the antinode of the oscillation, that is, the loop apex for the fundamental harmonic [Verwichte et al., 2017a]. The amplitude and period of the loop oscillation stays approximately constant for the duration of the simulation. For the high condensation region densities ($\mu = 0.62$ to $\mu = 0.83$) the cool plasma falls towards the loop footpoints along both sides of the loop similar to a real coronal rain shower scenario. This results in long period, large amplitude oscillations transitioning into persistent, smaller amplitude, shorter period oscillations once the condensations have fallen into the lower loop legs, where their mass has negligible effect on the loop oscillation period. The downfalling plasma blobs elongate as they fall due to the differential effective gravity

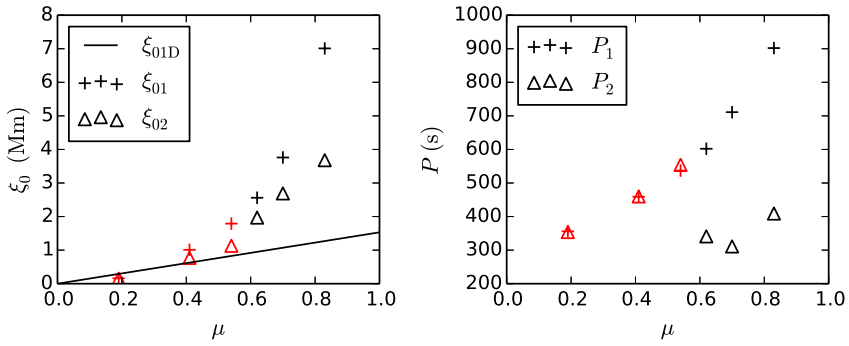

Figure 4.3: Dependence of amplitudes (left) and periods (right) of the vertical oscillation on the rain mass fraction μ at the beginning (ξ_{01}, P_1) and end (ξ_{02}, P_2) of the simulation. Values for low mass condensation regions for which the plasma remains trapped at the loop apex are shown in red. The solid line shows amplitudes predicted by 1D mechanical model by Verwichte et al. [2017a].

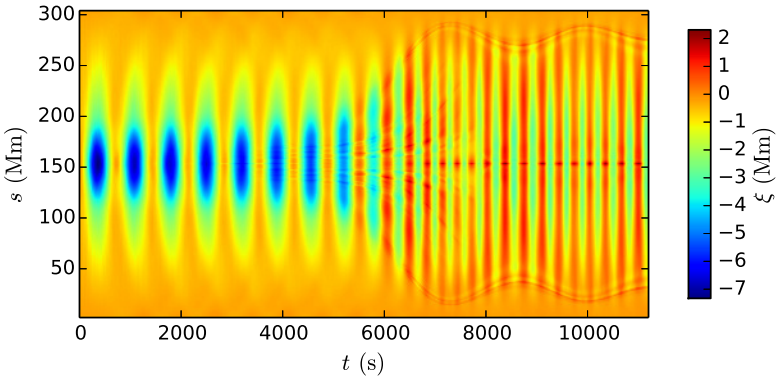

Figure 4.4: Loop axis displacement from its original position as a function of time and position along the loop for $\mu = 0.7$.

component acting along the finite length of the blob. The blobs develop elongated wings, leaving an evacuated region behind. The development of this v-shape is likely caused by the fact that the motion of the blob is subsonic in the background plasma but supersonic for its own temperature, leading to shock behaviour. The blobs are then gradually slowed down and ultimately rebound multiple times in the lower loop leg due the combined effect of the underlying plasma pressure and magnetic tension force counteracting the effective gravity [Mackay and Galsgaard, 2001]. This type of oscillatory motion of plasma condensations in longitudinal direction was studied in detail in Chapter 3.

The density difference between the condensation region and the background plasma

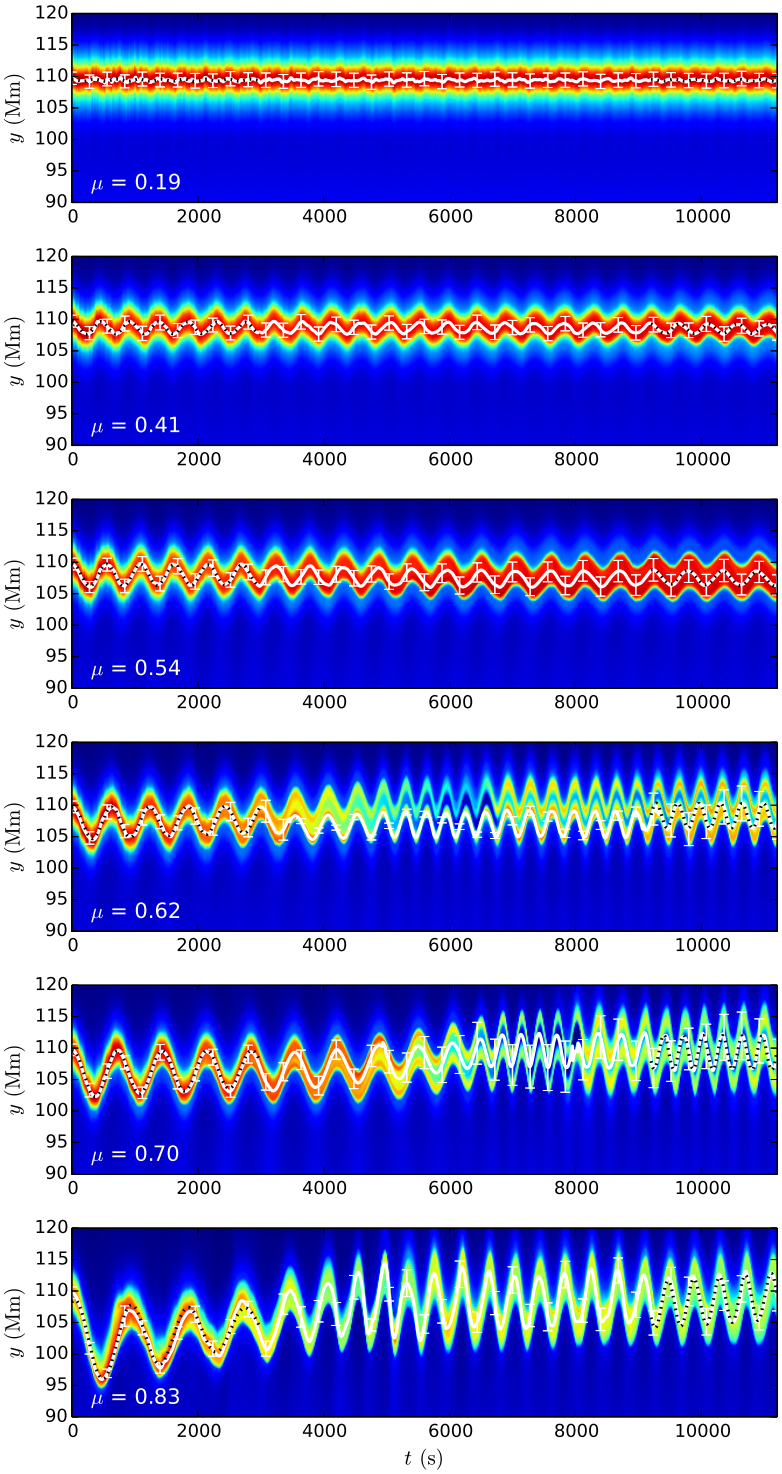

Figure 4.5: Time-distance plots at the loop apex for different values of condensation region masses. White solid lines show the centre of the loop profile determined by Gaussian fitting. Black dotted lines show best-fit damped sine function.

leads to onset of the Rayleigh-Taylor instability at the loop apex. Ripples of cool plasma are formed in the condensation region and later lead to fragmentation of the tails of the downfalling plasma blobs (Figure 4.2). A similar phenomenon can be seen in coronal rain observations, which typically show a lot of structuring in the longitudinal direction, resulting in a clumpy appearance of the downfalling coronal rain material [e.g. Antolin and Rouppe van der Voort, 2012; Antolin et al., 2015b]. Small fraction of the cool condensation plasma remains confined at the loop apex. This is caused by the action of the ponderomotive force pushing the plasma in the vicinity of the loop top towards the apex point where the effective gravity is zero. As the simulation setup is symmetric, the plasma remains trapped here for the duration of the simulation.

In order to analyse the evolution of the oscillation in detail, at each timestep we take a cut along the domain centre perpendicular to the loop axis to create density time-distance plots. The loop displacement time series is obtained by fitting a Gaussian to the density profile at each timestep. For the two peak profile seen at the higher condensation densities due to evacuation of the loop centre this approach leads to tracking one of the loop edges. Damped sine function of the form $\xi(t) = \xi_0 \exp(-t/\tau) \sin(\omega t + \phi)$ is fitted to the loop top displacement timeseries at the beginning and end of the simulation to obtain oscillation periods and amplitudes shown in Table 4.1. The periods and amplitudes of the oscillation during the initial phase increase with increasing mass of the condensation region (Figure 4.3). After most of the condensation mass has fallen from the loop top towards the loop footpoints, the oscillation period decreases to less than half of the original value. This is a result of change in the longitudinal density distribution along the loop, even though the total mass of the plasma in the loop remains conserved. A small degree of periodic modulation of the period can be observed during the latter half of the simulation as the plasma blobs oscillate in lower loop legs. The oscillation displacement profile of the fundamental harmonic also evolves with time, starting with a concentrated peak at the loop top and gradually broadening into a sine-like profile as the dense plasma moves towards loop footpoints (Figure 4.4).

Using an expression from Verwichte et al. [2017a] for the amplitude of a vertical oscillation excited by a dense plasma blob ξ_0 based on a 1D mechanical coronal rain model:

$$\xi_0 = (5.0 \pm 0.6) 10^{-3} \sqrt{1 - \frac{2\theta}{\pi}} \mu L \,, \tag{4.7}$$

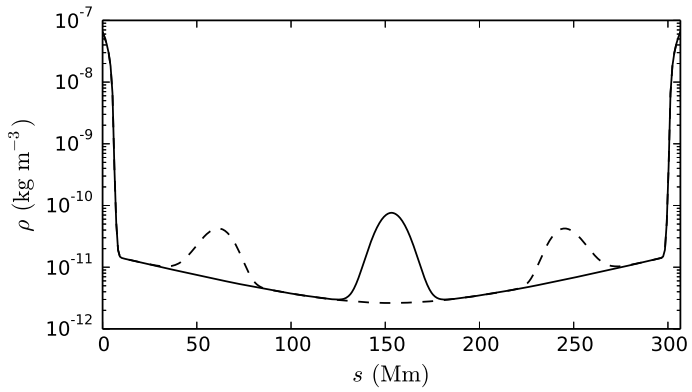

Figure 4.6: Internal density profiles used for the calculation of the oscillation period in thin flux tube approximation for the $\mu = 0.7$ case. Solid and dashed line show initial and final state of the loop respectively.

where θ is the angle between the loop plane and the photospheric normal, μ is the rain mass fraction and L is the length of the loop we estimate expected oscillation amplitudes for all condensation masses. We find that amplitude values predicted by this model agree with the oscillation amplitudes determined from the simulation for lowest masses of the condensation region, while at higher masses the two diverge and the 1D mechanical model underestimates the oscillation amplitude (Figure 4.3). Here we note that the simulated scenario does not comply with number of assumptions made in the 1D mechanical model, namely the assumption of small size of the plasma blobs and the constant loop length. The size of the condensation region used in the simulation is extended in the longitudinal direction, that is, along the loop axis and therefore cannot be approximated by a point-like mass. Similarly the coronal loop is significantly deformed in the simulation, thus violating the constant loop length assumption. The applicability of the 1D kinematic model to the cases with high condensation region masses studied here is therefore limited. It is however encouraging that the two models agree within their common range of validity at low condensation region masses. Furthermore, these results not only confirm that the presence of coronal rain is a possible excitation mechanism of transverse loop oscillations but also show that its effect is even greater than originally predicted.

We further determine the dependence of the loop oscillation periods on the longitudinal density profile of the loop semi-analytically using a 1D model. The vertical oscillation of a loop with longitudinal density dependence can be modelled in the thin flux tube limit using the equation [Dymova and Ruderman, 2005, 2006]:

$$\frac{\mathrm{d}^2\xi}{\mathrm{d}s^2} + \frac{\omega^2}{C_\mathrm{k}^2}\xi = 0\,, \tag{4.8}$$

where $\xi(s)$ is the loop displacement, ω is the mode frequency, $C_\mathrm{k}^2 = 2B^2/\mu_0(\rho_\mathrm{i}(s) + \rho_\mathrm{e}(s))$ and s is the coordinate along the loop. To model a line-tied coronal loop, $\xi(s)$ must satisfy the boundary conditions $\xi(0) = \xi(L) = 0$. Equation (4.8) is derived for the case of the uniform magnetic field. In the case of magnetic field variation in the longitudinal direction $\xi(s)$ in Eq. (4.8) modifies to $\xi(s)/\sqrt{B(s)}$ [Ruderman et al., 2008]. This change of the normalisation however only affects the displacement profile of the oscillation; the oscillation period remains unchanged.

Equation (4.8) for the thin flux tube model is solved numerically, with the mode frequency subsequently determined using a shooting method. Internal and external plasma density and magnetic field strength profiles along the loop are determined using the same magnetic field and density configuration as described in Sect. 2 and by averaging along the transverse direction of the loop. We solve the equation for all condensation region masses and for each mass we use two different density profiles; one corresponding to the initial state of the loop with density enhancement located at the loop apex, and one with the density enhancement split into two components each located in one loop leg, representative of the final state of the loop, where the condensation mass has fallen down under the influence of gravity (Figure 4.6). The resulting initial and final periods are shown in Table 4.1. For all condensation region masses, the thin flux tube model is found to overestimate the periods of the fundamental oscillation mode by about a factor of two compared to the periods determined from the simulation. The simulation setup used in this work is equivalent to modelling the loop as a curved magnetic slab rather than thin flux tube model used in the above calculation. We therefore attribute this difference to a different geometry used by the two models. The initial to final period ratios however agree with the simulation results for the higher condensation region masses ($\mu = 0.62$ to $\mu = 0.83$). We refrain from calculating the final state periods (i.e. with two density enhancements in the loop legs) for the low condensation region masses ($\mu = 0.19$ to $\mu = 0.54$) as in these cases there is no significant mass redistribution along the length of the loop during the simulation.

We further proceed to 1D calculation done for the case of a magnetic slab. The main caveat in this approach is that in the slab case, the kink speed is not well defined and the phase speed of a fast kink mode in a slab instead tends to external Alfvén speed in the long wavelength limit [Edwin and Roberts, 1982]. External Alfvén

speed of the loop in our setup however does not contain the information about the high density region. In order to incorporate the density variation inside the loop into a slab model, $C_{\rm k}$ in Eq. (4.8) is replaced by $V_{\rm Ae}(s) = B(s)/\sqrt{\mu\rho_{\rm i}(s)/\chi}$, where $\rho_{\rm i}$ is the density along the centre of the loop and $\chi = 10$ as specified in Sect. 2. This is not strictly correct as it assumes constant density contrast between the internal and external density profile which is equivalent to assuming that the structure of the external medium self-adjusts such that it reflects the density structuring along the centre of the loop. This is further supported by the fact that both the oscillation periods and period ratios calculated using this approach diverge from the simulation values with increasing mass of the condensation region (Table 4.1).

Table 4.1: Loop oscillation parameters

$r_{\rm bc}$	μ	$P_{\rm s1}$ (s)	$\xi_{0\rm s1}$ (Mm)	$P_{\rm s2}$ (s)	$\xi_{0\rm s2}$ (Mm)	$P_{\rm s1}/P_{\rm s2}$	$P_{\rm tube1}$ (s)	$P_{\rm tube2}$ (s)	$P_{\rm tube1}/P_{\rm tube2}$	$P_{\rm slab1}$ (s)	$P_{\rm slab2}$ (s)	$P_{\rm slab1}/P_{\rm slab2}$
1×10^1	0.19	356	0.16	354	0.15	1.0	758	-	1.0	555	-	1.0
3×10^1	0.41	459	1.01	460	0.77	1.0	931	-	1.0	850	-	1.0
5×10^1	0.54	537	1.79	554	1.13	1.0	1079	-	1.0	1068	-	1.0
7×10^1	0.62	602	2.56	341	1.97	1.8	1210	712	1.7	1248	474	2.6
1×10^2	0.70	711	3.76	311	2.69	2.3	1385	735	1.9	1478	532	2.8
2×10^2	0.83	902	7.01	409	3.68	2.2	1853	809	2.3	2068	697	3.0

Initial and final oscillation periods and amplitudes for different condensation region masses determined from the simulation ($P_{\rm s1}$, $P_{\rm s2}$) and calculated using the thin flux-tube model ($P_{\rm tube1}$, $P_{\rm tube2}$) and slab model ($P_{\rm slab1}$, $P_{\rm slab2}$). We do not include 1D model final state periods for the low condensation region masses as there is no significant mass redistribution during the simulation.

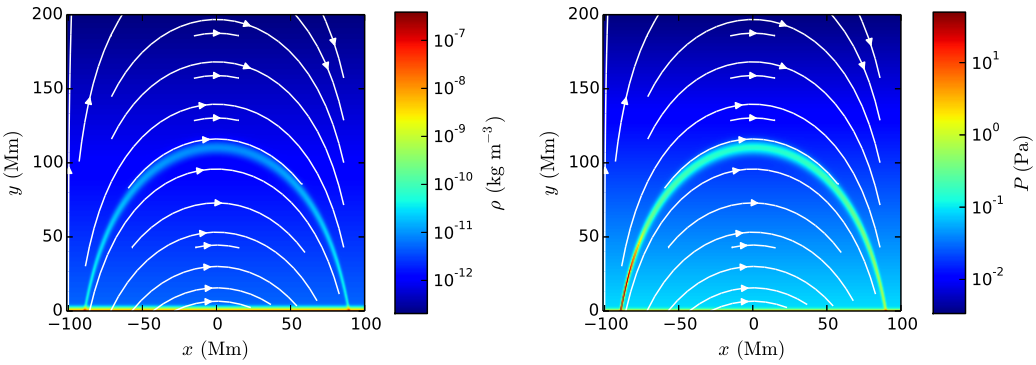

Figure 4.7: Left: Initial density configuration of the coronal loop. Right: Initial pressure configuration showing enhanced pressure in the left foot point. The white lines show the B-field direction.

4.4 Excitation of vertical loop oscillations by siphon flows

In order to establish a siphon flow, the pressure difference between the loop footpoints is created by increasing the pressure of left footpoint according to

$$P = \Pi P_{\rm eq} \exp\left(-\frac{(x - x_{\rm fp})^2}{2\sigma_{\rm x}^2} - \frac{(y - y_{\rm L})^2}{2\sigma_{\rm y}^2} \right) \tag{4.9}$$

where $\sigma_{\rm x} = 5$ Mm, $\sigma_{\rm y} = 1$ Mm, $x_{\rm fp}$ is the x-coordinate of the left footpoint, $P_{\rm eq}(x, y)$ is the background equilibrium pressure and Π is the contrast between the peak and equilibrium values at the footpoint (Figure 4.7). This pressure enhancement corresponds to increase in temperature by the same factor, assuming the density remains at the equilibrium values.

We run simulations for 5 different values of amplitude of the pressure enhancement corresponding to the values of the pressure contrast $\Pi = 30$, 40, 50, 70 and 100. In all cases, the pressure imbalance between the footpoints triggers a flow of material from the left footpoint to the right, as clearly seen in a time-distance plot of the density along the loop against time (Figure 4.8). As the material approaches the right footpoint, it rebounds in the opposite direction. This process repeats with the material traversing the apex multiple times with decreasing speeds. The mechanism for this rebound is associated with the pressure build-up in the plasma close to the footpoints and with the action of the magnetic tension force resulting from bending of magnetic field lines and has been investigated in detail in Mackay and Galsgaard

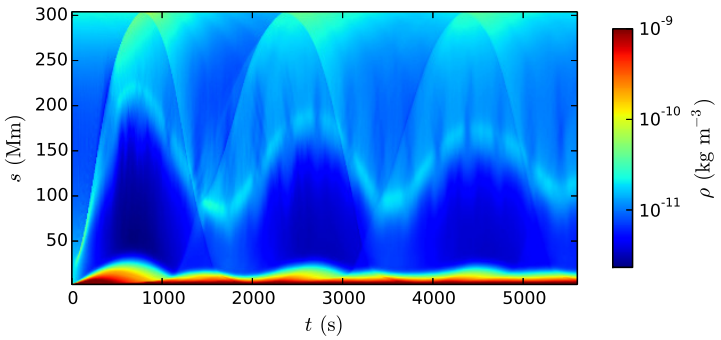

Figure 4.8: Time-distance plot of the density along the loop averaged over 3 Mm in the direction perpendicular to the loop axis for $\Pi = 50$ during first 5600 s.

[2001] and in Chapter 3.

During the initial phase of the flow, the fast moving material travels past the loop apex at the maximum speed. The centrifugal force on the fast flowing plasma initially displaces the loop axis outwards. The restoring action of the Lorentz force pulls it back down resulting in onset of a fundamental harmonic of a fast kink mode, as seen in the plot of the loop axis displacement determined as a function of distance along the loop. As seen from the time-distance plots of the location of the loop apex as a function of time shown in Figure 4.9, there is a delay of ~ 300 s between the launch of the flow and the onset of the oscillation. This suggests that the excitation happens when the fast moving material first passes the apex of the loop. This is as expected taking into account the magnetic field geometry in our setup; the centrifugal force is inversely proportional to the radius of the curvature, which is greatest at the loop apex.

These oscillations are not predominantly caused by the overdensity at the loop apex as studied in Section 4.3, despite the fact that a considerable mass of plasma is passing through the loop apex, as this would result in a downward displacement of the loop axis. Figure 4.10 shows that the loop axis is displaced outwards, suggesting that this effect is negligible compared to the effect of the centrifugal force.

In order to analyse the loop oscillations, at each timestep we take a cut along the centre of the domain perpendicular to the loop axis to create density time-distance plots. The loop apex displacement time series is obtained by fitting a Gaussian to the density profile at each timestep. We determine the loop oscillation parameters by fitting a sine function of the form $\xi(t) = \xi_0 \sin(\omega t + \phi)$ to the loop displacement time series. The average oscillation period is ~ 340 s; although a slight modulation of

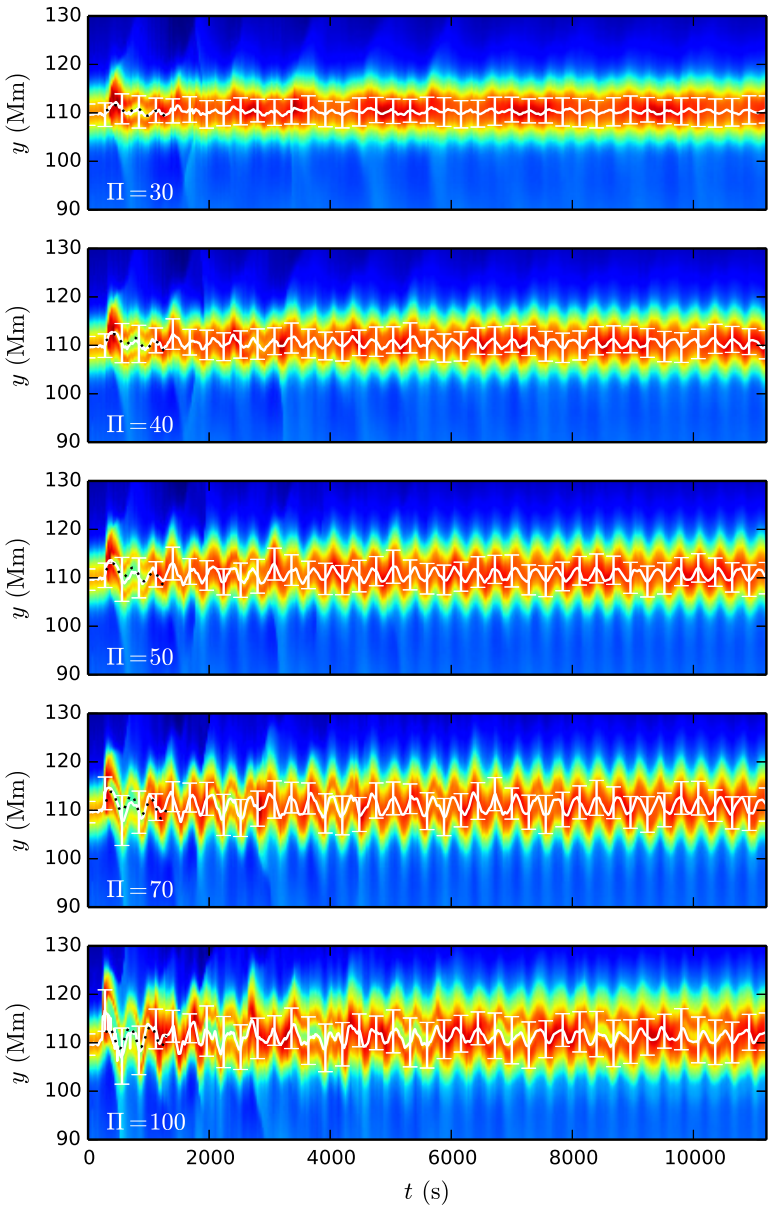

Figure 4.9: Time-distance plots at the loop apex for different values of footpoint pressure contrast. White solid lines show the centre of the loop profile determined by Gaussian fitting. Black dotted lines show best-fit sine function.

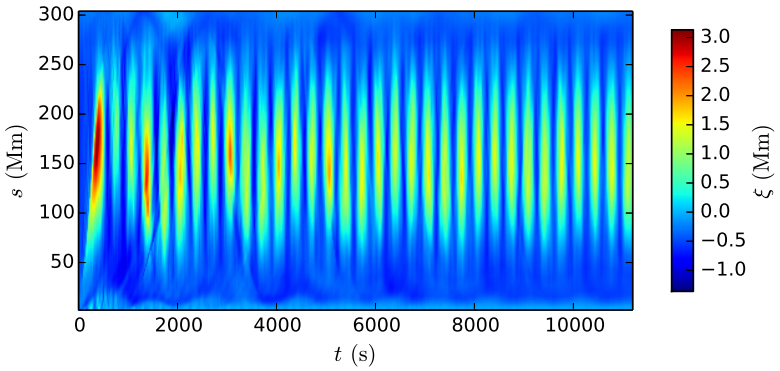

Figure 4.10: Loop axis displacement from its original position as a function of time and position along the loop for $\Pi = 50$.

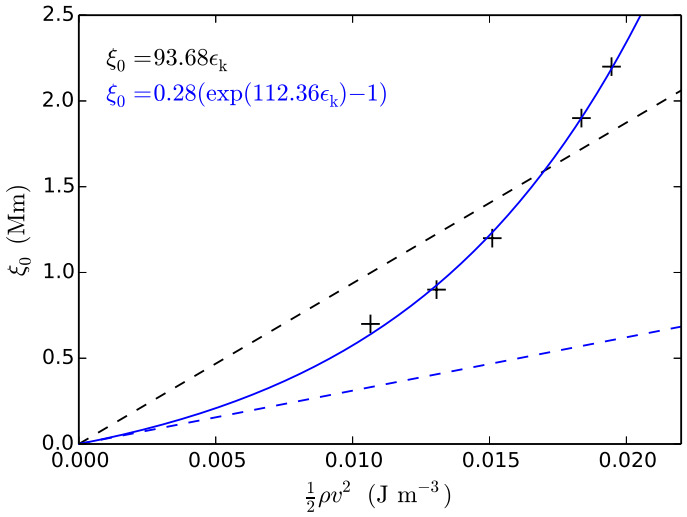

Figure 4.11: Dependence of loop oscillation amplitude on kinetic energy density of the moving plasma at the loop apex. Solid blue line shows exponential fit to the data and dashed blue line shows linear expansion for small values of ϵ_k. Black dashed line shows linear fit to the data.

the oscillation period is present for all pressure amplitudes, caused by the changes of the longitudinal density profile of the loop resulting from the motion of the flowing material along the loop axis (as studied in Section 4.3). The amplitude of the oscillation varies from 0.7 to 2.2 Mm and increases with increasing pressure contrast at the footpoint, leading to faster flow velocity. The average speeds at which the flow passes the loop apex vary from 63 to 96 km s^{-1}, while the sound speed at the loop apex is $\sim$ 170 km s^{-1}. We determine the kinetic energy density of the flow plasma using the average flow speed and the average density of the fast moving plasma at the apex. The dependence of the oscillation amplitude on the flow kinetic energy is approximately linear for small values of kinetic energy density and diverges from the linear regime for larger values (Figure 4.11).

An estimate of the amplitude of the oscillation excited by the flow can be obtained by writing down an equation for a flow driven kink oscillation:

$$\left[\frac{\partial^2}{\partial t^2} - C_{\rm k}^2 \frac{\partial^2}{\partial s^2}\right] \xi = \frac{\rho \Delta s}{\rho_{\rm L} L_{\rm loop}} \frac{V_0^2}{R(s)} G(s,t)\,, \tag{4.10}$$

where $C_{\rm k}$ is the kink speed and the right hand side represents the driving centrifugal force. Here V_0 is the average flow velocity, $R(s)$ is the radius of the curvature of the loop as a function of distance along the loop, the $\rho\Delta s/\rho_{\rm L} L_{\rm loop}$ term represents the mass of the plasma contained in the flow normalised by the total loop mass and $G(s,t)$ is the shape of the flow pulse (to account for the fact that the flow due to the footpoint pressure difference is localised, as opposed to a uniform flow along the whole loop) represented by a dimensionless and normalised function of time and distance along the loop. The loop displacement ξ can be written as a superposition of normal modes $\xi = \Sigma a_n \sin(k_n s)$. Similarly, $G(s,t)/R(s) = \Sigma g_n(t)/R_n \sin(k_n s)$. Equation (4.10) therefore becomes

$$\left[\frac{d^2}{dt^2} - \omega_n^2\right] a_n = \frac{\rho \Delta s}{\rho_{\rm L} L_{\rm loop}} \frac{V_0^2}{R_n} g_n(t)\,, \tag{4.11}$$

where ω_n is the mode frequency. This leads to the estimate of the mode amplitude given by

$$a_n \sim \frac{\rho \Delta s}{\rho_{\rm L} L_{\rm loop}} \frac{V_0^2}{R_n} \frac{g_n(t)}{\omega_n^2}\,. \tag{4.12}$$

Assuming $V_0 = 80$ km s^{-1}, $g_1 = 1$ for a sine-like pulse, $R_1 = 90$ Mm, $\omega_1 = 0.018$ rad s^{-1} corresponding to oscillation periods of $\sim$ 340 s, $\Delta s/L_{\rm loop} = 0.5$ and $\rho/\rho_{\rm L} \sim 10$ results in the amplitude of the fundamental harmonic $a_1 \sim 1$ Mm, i.e. in agreement

with the simulation amplitudes.

4.5 Discussion and conclusions

4.5.1 Effect of dense condensation region

We presented 2.5D MHD simulations of the evolution of a coronal loop with a cool and dense condensation region located at the loop apex. The mass of the condensation region was found to excite vertically polarised transverse loop oscillations. We analysed the dependence of the amplitudes and periods of the excited oscillations as a function of condensation region mass. The observed shift in the fundamental kink mode period of the loop following a coronal rain shower seen in the simulation agrees with the period shift described in Verwichte and Kohutova [2017], where it was explained as a consequence of the drainage of the total loop mass by the coronal rain into the chromosphere. Here we have shown that period shifts can also be explained by redistribution of the mass along the length of the coronal loop as the cool dense plasma falls from the top of the loop.

Long term confinement of the plasma at the loop apex seen in the simulation is not likely for real loops undergoing condensation formation due to lack of symmetry being common in these cases. This lack of symmetry can be due to a number of reasons such as the asymmetric nature of footpoint heating mechanism or due to siphon flows caused by the pressure difference between the footpoints. It has indeed been observed that the latter can lead to shifting the condensation region away from the loop apex such that the coronal rain is seen to fall along one loop leg only as shown in Chapter 2.

The development of Rayleigh-Taylor instability along the interface between the dense condensation plasma and coronal plasma at the bottom edge of the loop apex resulting from the density difference between the two was seen during early stages of the loop evolution. This resulted in a formation of ripples along the interface and subsequently lead to fragmentation of the tails of the downfalling condensations. The Rayleigh-Taylor instability has been observed to develop in prominence-corona transition region in cases where dense prominence plasma is suspended above a coronal cavity [Berger et al., 2010; Hillier et al., 2012]. It is however unclear if such scenario is realistic in coronal loops undergoing condensation formation, given the realistic density estimates and taking into account typical magnitudes and orientation of the magnetic field (which at the loop top is parallel to the fluid interface).

The fragmentation of the condensed plasma seen in our simulation resulting from the Rayleigh Taylor instability is however in line with observed clumpy structure of the coronal rain.

The approach used here imposes the existence of the condensation region as an initial condition and hence the density enhancement is introduced abruptly, which is equivalent to assuming that the catastrophic cooling leading to condensation formation occurs instantaneously. Here we point out that in the real scenario, the condensation formation process will be gradual and the coronal loop can be expected to readjust to some extent while the condensation region is being formed. This will limit the effect of the density enhancement on the oscillatory behaviour of the loop. We can estimate whether the vertical oscillations will still be triggered during the gradual formation process by comparing the characteristic radiative cooling time scale with the typical oscillation amplitude. The radiative cooling time scale $\tau_{\rm rad}$ can be estimated using the RTV radiative loss function:

$$n_{\rm e}^2 \chi_{\rm R} T^{\alpha} \simeq \frac{k_{\rm b}}{(\gamma - 1)} n_{\rm e} \frac{T}{\tau_{\rm rad}} \,, \tag{4.13}$$

where $n_{\rm e}$ is the plasma electron density, γ is the ratio of specific heats, $\chi_{\rm R}$ and α are radiative loss function coefficients as given in Rosner et al. [1978]. Using the typical coronal values $T = 10^6$ K and $\rho = 10^{-11}$ kg m^{-3} as employed in the simulation, we obtain $\tau_{\rm rad} = 300$ s, i.e. similar but less than the typical oscillation periods of 400 - 900 s. This is the higher bound on the $\tau_{\rm rad}$ since as the condensation forms, the density increases from coronal to chromospheric values and the characteristic radiative cooling time scale will further decrease. In this particular scenario it can be concluded that the condensation formation is abrupt enough for the loop oscillations to be triggered. In addition, we also use the temperature and density values determined from the observations in Verwichte and Kohutova [2017] and obtain $\tau_{\rm rad} \sim 500$ s as compared to the typical oscillation period of ~ 150 s observed therein, i.e. the same order of magnitude but larger. Here it should be pointed out that the determination of the plasma electron density from the observations depends on the assumption of line-of-sight depth of the loop and is therefore subject to large uncertainties. The oscillations and catastrophic cooling can therefore be expected to occur on similar time scales, exact balance of which is subject to specific conditions in the loop.

A decrease in the oscillation period similar to the one studied in this work was found in cooling loops [Morton and Erdélyi, 2009; Ruderman, 2011; Magyar et al.,

2015]. Both have the same fundamental cause, the change in the longitudinal density profile of the loop, namely the redistribution of the loop plasma from the loop top to the loop footpoints. However, the processes leading to the mass redistribution are different in the two cases; in our case the cause are downfalling condensations, modelled as a result of catastrophic cooling process with short timescale $\tau_{\rm cool}$. The change in period due to downfalling condensations is therefore abrupt and occurs on a timescales of ~ 100 s, that is, the time it takes for the condensations to move significantly under the influence of gravity. In the latter scenario it is the gradual flow of mass from the loop top to the loop points caused by temperature decrease leading to scale-height decrease as a result of gradual cooling process with long $\tau_{\rm cool}$. The period change due to loop cooling obviously depends on the cooling timescale, but is usually more gradual and in the above studies occurs on timescales of ~ 1000 s.

A natural extension of the work presented here is to model the coronal rain self-consistently, that is, model the whole process of thermal instability onset and coronal rain formation starting with a footpoint-heated stratified loop and look for signatures of vertical oscillations. The excitation of the vertical oscillations will then depend on the fraction of the total loop mass that condenses to form coronal rain and on the spatial distribution of the condensed plasma as well as on the temporal evolution of the condensation process. The approach used in this chapter however enables us to carry out a parameter study. Imposing the existence of the condensation region as an initial condition gives us control over its properties, which makes it easier for us to understand the conditions under which the excitation of the vertical oscillations is significant and how the condensation mass affects the periods and amplitudes of the excited oscillations.

4.5.2 Effect of siphon flow

The flows of plasma with speeds below 100 km s^{-1} are common in dynamic coronal loops [Teriaca et al., 2004; Doyle et al., 2006]. We found that a siphon flow with realistic speed is capable of exciting vertically polarised transverse loop oscillations with observable amplitudes ranging from few hundred km to 2 Mm, depending on the flow speed and the length of the loop. In addition to rapidly damped large amplitude transverse loop oscillations excited by a blast wave or a nearby flare and damped within few oscillation periods [e.g. Aschwanden et al., 1999; Nakariakov et al., 1999; White and Verwichte, 2012], there are multiple observations of small amplitude persistent transverse loop oscillations seen by SDO/AIA in quiet regions

with no apparent excitation mechanism [Wang et al., 2012; Nisticò et al., 2013]. These are typically explained by footpoint motions driven from the photosphere. In addition to the excitation of oscillations linked to thermal instability and coronal rain formation [Verwichte and Kohutova, 2017] also studied in Section 4.3, siphon flows (whether sustained of intermittent) hence act as another possible excitation mechanism that can explain these small amplitude sustained oscillations.

Pressure enhancement at one footpoint, which is equivalent to enhancement in temperature can occur as a result of asymmetric footpoint concentrated heating. Hence our problem could also be set up by enabling thermal conduction and heating one footpoint, rather than imposing a pressure enhancement as an initial condition. Neglecting thermal conduction does not have a significant effect on the large scale evolution of the loop and excitation of the oscillations, as verified by a test run for the $\Pi = 50$ case with the thermal conduction enabled. This is not surprising as the thermal conduction timescale $\tau_\kappa \sim L^2 n_\mathrm{e} k_\mathrm{B}/\kappa_0 T^{5/2}$ is of the order of ~ 1000 s for coronal values used here and $L = 10$ Mm, which is long compared to the timescale on which the flow with average speed 100 km s^{-1} travels over the same distance $\tau_\mathrm{flow} \sim 100$ s. Our approach was therefore chosen purely due to being less computationally expensive. Considering likely differences in the response of the loop plasma to the pressure enhancement once both thermal conduction and radiative losses are taken into account, the most accurate way to simulate flow velocities resulting from pressure imbalance would be using a fully self-consistent approach. This would involve including thermal conduction together with radiative losses, steady background coronal heating and using additional asymmetric footpoint heating term to create the pressure imbalance and trigger the flow.

We note that we observed excitation of fundamental harmonic with the maximum displacement of the loop axis at the loop apex, in contrast to oscillations with maximum displacement in the loop legs reminiscent of second order harmonic seen in Ofman et al. [2012]. We attribute this difference to differences in the magnetic field configuration used in the two studies, with the radius of curvature of magnetic field lines being greater in coronal loop legs using our model.

It has also been proposed that the centrifugal force can result in excitation of transverse loop oscillations by fast moving coronal rain condensations formed in the loop as a result of thermal instability [Verwichte et al., 2017b]. However, the coronal rain blobs typically move with sub-ballistic speeds caused by pressure of the underlying plasma [Oliver et al., 2014] with only a small fraction having faster than free fall speeds [Antolin and Verwichte, 2011]. The fast speeds are typically explained by

the blobs being accelerated by a background flow of the plasma [Müller et al., 2005; Fang et al., 2015]. In this scenario, it is the combined effect of the fast moving cool blobs and the flow that can act as an oscillation excitation mechanism.

Chapter 5

Summary

This work addressed the interplay between MHD oscillations and coronal rain. We presented observational evidence of thermal instability and an associated analysis of temperature and density evolution of a thermally unstable coronal loop; evidence and analysis of transverse coronal rain oscillations; and a detailed study of kinematics and evolution of coronal rain condensations utilising high resolution solar observations from multiple space-based instruments. We further studied observed phenomena by carrying out large scale numerical simulations of coronal rain formation and evolution to pinpoint fundamental physical mechanisms responsible for behaviour seen in observations. We established possible reasons for observed sub-ballistic motion and for longitudinal oscillations of coronal rain condensations. We further established that the thermal instability and coronal rain can lead to the excitation of transverse coronal loop oscillations and addressed excitation mechanisms linked to presence of a cool and dense condensation region and to siphon flows caused by pressure imbalance between loop footpoints. This section summarises conclusions resulting from each chapter.

In Chapter 2 we analysed transverse oscillations and kinematics of coronal rain observed by IRIS, Hinode/SOT and SDO/AIA. Two different regimes of transverse oscillations traced by the rain in the studied coronal loop were observed: small-scale oscillations with mean period of 3.4 min and amplitudes between 0.2-0.4 Mm observable along the whole loop length and large-scale oscillations with mean period 17.4 min and amplitudes around 1 Mm, observable only in the lower part of the loop. The small scale oscillations were visible during most of the duration of the dataset without any observable damping, they were therefore likely driven by a continuously operating process. The collective behaviour of the individual oscillating strands and

lack of phase shift suggests they correspond to a standing wave excited along the whole loop. The 3.4 min period of this oscillation regime is consistent with period expected for a fundamental harmonic of the loop with similar length. The large scale oscillations were only visible in the latter half of the observational sequence. The unusually long period suggests a propagating wave scenario, where the wave is excited by a transient mechanism localised near the loop footpoints.

Plasma condensations were found to move with speeds ranging from few km s^{-1} up to 180 km s^{-1} and with accelerations that were largely below the free-fall rate. The broad velocity distribution, sub-ballistic motion and complex velocity profiles of individual blobs showing multiple acceleration and deceleration phases suggest that forces other than gravity have significant effect on the evolution of the coronal rain, with the likely candidates being pressure effects and the ponderomotive force caused by the transverse loop oscillations.

The evolution of the emission of the plasma at the loop top observed in individual SDO/AIA bandpasses was found to exhibit clear signatures of a gradual cooling linked to the formation of plasma condensations. The temperature evolution of the plasma was examined in more detail using DEM regularisation technique and by forward modelling the emission intensities in the SDO/AIA bandpasses using a two component DEM model dependent on the evolution of the temperature and density of the plasma near the apex of the coronal loop. The inferred evolution was found to be consistent with the limit cycle model of the coronal loop and suggests the observed loop was going through a sequence of periodically repeating heating-condensation cycles.

In Chapter 3 we analysed mechanisms responsible for the sub-ballistic fall rates and for longitudinal oscillations of coronal rain condensations seen in the observational study. To do this, we carried out 2.5D MHD simulations of dynamics and evolution of a cool and dense plasma condensation in a gravitationally stratified coronal loop. The problem set up was chosen to be representative of small coronal rain condensations formed near the top of a coronal loop as a result of thermal instability. The geometry of the problem was set up to reflect the coronal loop geometry, accounting for the reduced effective gravity due to the semicircular shape of the loop. Realistic stratification of the atmosphere was subsequently achieved by using a temperature profile representative of a cool chromosphere, thin transition region layer and hot corona.

We analysed the dynamics of the plasma condensations for a range of condensa-

tion densities and magnetic field strengths by tracking condensation trajectories, speeds and accelerations and by comparing them to high resolution coronal rain observations. We found that the motion and evolution of plasma condensations were strongly affected by the plasma pressure in the coronal loop, and the coronal plasma pressure gradients can be high enough to account for the lower-than-free-fall speed of the coronal rain. The fastest downward velocities of plasma condensations seen in the simulations were found to be in agreement with recent coronal rain observations. We also found that high coronal magnetic field strength or low mass of condensations can lead to oscillatory motion consisting of multiple rebounds damped through sound wave emission, with the condensation eventually settling in an equilibrium position supported by the pressure of the underlying plasma. We further analysed the balance of forces acting on the condensation. Rebounding of the condensation was found to be due to a combined effect of the pressure gradient force and the magnetic tension force resulting from bending of the magnetic field lines under the condensation in the lower part of the coronal loop. The period and damping scaling time of the condensation oscillations were consistent with values determined using an analytical model based on an idealised MHD piston scenario.

This analysis also highlighted the fact that the dynamics of the plasma condensations, especially the presence or lack of oscillatory motion and the parameters of the condensation oscillations are determined by the mass of the condensation relative to the total coronal loop mass. There is still considerable uncertainty about what fraction of the total mass of the coronal loop plasma condenses into coronal rain after catastrophic cooling takes place; current estimates of the loop-to-rain mass ratio from observations are of the order of 1 - 10 [Antolin et al., 2015b], these are however subject to the spatial resolution limits of the instruments. It is therefore likely that a significant fraction of the condensation mass in thermally unstable coronal loops remains undetected.

In Chapter 4 we analysed mechanisms responsible for excitation of transverse coronal loop oscillations associated with thermal instability and coronal rain, as the observational evidence suggested presence of a link between the two phenomena. This was done by carrying out 2.5D MHD simulations of a coronal loop embedded in a realistically stratified atmosphere consisting of cool chromosphere, thin transition region and hot corona.

We first investigated the effect of a cool and dense condensation region located at the apex of the loop. We found that the presence of the condensation region excites fundamental harmonic of a vertically polarised kink mode. We analysed the

dependence of the amplitudes and periods of the excited oscillations on the mass of the condensation region. The change in the longitudinal density profile of the coronal loop caused by the condensations falling from the top of the loop towards the solar surface due to gravity was found to lead to the decrease of the oscillation period. It was therefore shown that the evolution of the oscillation period can be used to determine the fraction of the condensation plasma relative to the total loop mass from observations of coronal loop oscillations.

We further investigated the effect of plasma flow directed from one footpoint to another caused by a pressure imbalance between the footpoints. Such flows are though to be a consequence of an asymmetric footpoint heating likely to lead to coronal rain formation, and therefore are often present in thermally unstable loops. The siphon flow was found to excite fundamental harmonic of a vertically polarised kink mode due to the effect of the centrifugal force acting on the fast moving plasma. Dependence of the oscillation amplitude on the amplitude of the pressure difference was found to diverge from expected linear relationship, likely as a result of change in the distribution of the total mass of the plasma contained in the flow.

These two mechanisms therefore provide explanation for the excitation of vertically polarised transverse loop oscillations in quiescent loops without the need for specific external drivers placed below the loop. Approach used in this chapter based on imposing the existence of the condensation region as an initial condition provides full control over the condensation properties. This enabled us to carry out a parameter study of the dependence of loop oscillation properties on the mass of the condensation region. However, in order to study the effect of the two mechanisms formed in self-consistent manner, a complete simulation including coronal rain formation as a result of footpoint-localised asymmetric heating is necessary.

The observational evidence shown in this work together with other studies [Antolin and Verwichte, 2011; Verwichte et al., 2017a; Verwichte and Kohutova, 2017] suggest that coronal rain oscillations are not a rare phenomenon. Their small oscillation amplitudes, lack of observable damping and oscillation periods matching the loop fundamental harmonic period mean that coronal rain oscillations share many characteristics with so-called "decayless" coronal loop oscillations, recently reported in AIA observations [Wang et al., 2012; Nisticò et al., 2013] and hence are their likely counterpart in hotter wavelengths. These are now known to be abundant in the solar corona [Anfinogentov et al., 2015]; however, their excitation mechanism is unclear. It was previously proposed that their excitation might be related to p-mode leakage or that they might be driven by footpoint motions [Nisticò et al., 2013]. This work

has shown that this oscillation regime can also be excited by thermal instability and coronal rain formation, rather than being driven from the photosphere, which has implications for our understanding of coupling and dissipation of oscillations in lower solar atmosphere. This work, together with the observational study by Verwichte and Kohutova [2017] has further highlighted the seismological potential of coronal rain oscillations, as they can be used to determine what fraction of coronal loop plasma becomes thermally unstable and hence how localised the coronal loop heating is.

A natural extension of the work presented here is to carry out numerical simulations of the coronal rain formation by including the effects of thermal conduction, radiative losses and footpoint-localised coronal heating. Studying coronal rain formation under different conditions and looking for evidence of oscillation excitation mechanisms investigated in this work would establish their validity in more general context. Numerical simulations of the complete thermal cycle of a coronal loop can be further linked to observations of all phases of a coronal rain event in wavelengths covering temperatures ranging from chromospheric to coronal. This will be possible after DKIST observations become available, providing unprecedented spatial and temporal resolution as well as spectral information across a wide range of wavelengths.

Bibliography

J. Andries, I. Arregui, and M. Goossens. Determination of the Coronal Density Stratification from the Observation of Harmonic Coronal Loop Oscillations. *ApJ*, 624(1):L57, 2005a. doi: 10.1086/430347.

J. Andries, M. Goossens, J. V. Hollweg, I. Arregui, and T. Van Doorsselaere. Coronal loop oscillations - Calculation of resonantly damped MHD quasi-mode kink oscillations of longitudinally stratified loops. *A&A*, 430(3):1109–1118, 2005b. doi: 10.1051/0004-6361:20041832.

J. Andries, T. Van Doorsselaere, B. Roberts, G. Verth, E. Verwichte, and R. Erdélyi. Coronal Seismology by Means of Kink Oscillation Overtones. *Space Sci. Rev.*, 149 (1-4):3–29, 2009. doi: 10.1007/s11214-009-9561-2.

S. Anfinogentov, G. Nisticò, and V. M. Nakariakov. Decay-less kink oscillations in coronal loops. *A&A*, 560:A107, 2013. doi: 10.1051/0004-6361/201322094.

S. A. Anfinogentov, V. M. Nakariakov, and G. Nisticò. Decayless low-amplitude kink oscillations: a common phenomenon in the solar corona? *A&A*, 583:A136, 2015. doi: 10.1051/0004-6361/201526195.

S. K. Antiochos and J. A. Klimchuk. A model for the formation of solar prominences. *ApJ*, 378:372–377, 1991. doi: 10.1086/170437.

S. K. Antiochos, P. J. MacNeice, D. S. Spicer, and J. A. Klimchuk. The Dynamic Formation of Prominence Condensations. *ApJ*, 512(2):985, 1999. doi: 10.1086/306804.

P. Antolin and L. Rouppe van der Voort. Observing the Fine Structure of Loops through High-resolution Spectroscopic Observations of Coronal Rain with the CRISP Instrument at the Swedish Solar Telescope. *ApJ*, 745(2):152, 2012. doi: 10.1088/0004-637X/745/2/152.

P. Antolin and E. Verwichte. Transverse Oscillations of Loops with Coronal Rain

Observed by Hinode/Solar Optical Telescope. *ApJ*, 736(2):121, 2011. doi: 10.1088/0004-637X/736/2/121.

P. Antolin, K. Shibata, and G. Vissers. Coronal Rain as a Marker for Coronal Heating Mechanisms. *ApJ*, 716(1):154, 2010. doi: 10.1088/0004-637X/716/1/154.

P. Antolin, G. Vissers, and L. Rouppe van der Voort. On-Disk Coronal Rain. *Sol. Phys.*, 280(2):457–474, 2012. doi: 10.1007/s11207-012-9979-7.

P. Antolin, T. Yokoyama, and T. Van Doorsselaere. Fine Strand-like Structure in the Solar Corona from Magnetohydrodynamic Transverse Oscillations. *ApJ*, 787 (2):L22, 2014. doi: 10.1088/2041-8205/787/2/L22.

P. Antolin, T. J. Okamoto, B. De Pontieu, H. Uitenbroek, T. Van Doorsselaere, and T. Yokoyama. Resonant Absorption of Transverse Oscillations and Associated Heating in a Solar Prominence. II. Numerical Aspects. *ApJ*, 809(1):72, 2015a. doi: 10.1088/0004-637X/809/1/72.

P. Antolin, G. Vissers, T. M. D. Pereira, L. Rouppe van der Voort, and E. Scullion. The Multithermal and Multi-stranded Nature of Coronal Rain. *ApJ*, 806(1):81, 2015b. doi: 10.1088/0004-637X/806/1/81.

U. Anzer. The stability of force-free magnetic fields with cylindrical symmetry in the context of solar flares. *Sol. Phys.*, 3:298–315, 1968. doi: 10.1007/BF00155164.

T. Arber, A. Longbottom, C. Gerrard, and A. Milne. A staggered grid, Lagrangian-Eulerian remap code for 3-D MHD simulations. *J. Comput. Phys.*, 171(1):151–181, 2001. doi: 10.1006/jcph.2001.6780.

M. J. Aschwanden, L. Fletcher, C. J. Schrijver, and D. Alexander. Coronal Loop Oscillations Observed with the Transition Region and Coronal Explorer. *ApJ*, 520:880–894, 1999. doi: 10.1086/307502.

M. J. Aschwanden, R. W. Nightingale, and D. Alexander. Evidence for Nonuniform Heating of Coronal Loops Inferred from Multithread Modeling of TRACE Data. *ApJ*, 541:1059–1077, 2000. doi: 10.1086/309486.

M. J. Aschwanden, C. J. Schrijver, and D. Alexander. Modeling of Coronal EUV Loops Observed with TRACE. I. Hydrostatic Solutions with Nonuniform Heating. *ApJ*, 550(2):1036, 2001. doi: 10.1086/319796.

M. J. Aschwanden, B. De Pontieu, C. J. Schrijver, and A. M. Title. Transverse Oscillations in Coronal Loops Observed with TRACE II. Measurements

of Geometric and Physical Parameters. *Sol. Phys.*, 206(1):99–132, 2002. doi: 10.1023/A:1014916701283.

R. G. Athay. *The solar chromosphere and corona: Quiet sun.* Reidel, 1976.

F. Auchère, K. Bocchialini, J. Solomon, and E. Tison. Long-period intensity pulsations in the solar corona during activity cycle 23. *A&A*, 563:A8, 2014. doi: 10.1051/0004-6361/201322572.

I. Ballai, R. Erdélyi, and B. Pinér. On the Nature of Coronal EIT Waves. *ApJL*, 633:L145–L148, 2005. doi: 10.1086/498447.

D. Banerjee, D. Pérez-Suérez, and J. G. Doyle. Signatures of Alfvén waves in the polar coronal holes as seen by EIS/Hinode. *A&A*, 501(3):L15–L18, 2009. doi: 10.1051/0004-6361/200912242.

T. Berger, P. Testa, A. Hillier, P. Boerner, B. C. Low, K. Shibata, C. Schrijver, T. Tarbell, and A. Title. Magneto-thermal convection in solar prominences. *Nature*, 472(7342):197–200, 2011. doi: 10.1038/nature09925.

T. E. Berger, G. Slater, N. Hurlburt, R. Shine, T. Tarbell, A. Title, Bruce W. Lites, T. J. Okamoto, K. Ichimoto, Y. Katsukawa, T. Magara, Yoshinori Suematsu, and T. Shimizu. Quiescent Prominence Dynamics Observed with the Hinode Solar Optical Telescope. I. Turbulent Upflow Plumes. *ApJ*, 716(2):1288, 2010. doi: 10.1088/0004-637X/716/2/1288.

P. Boerner, C. Edwards, J. Lemen, A. Rausch, C. Schrijver, R. Shine, L. Shing, R. Stern, T. Tarbell, A. Title, C. J. Wolfson, R. Soufli, E. Spiller, E. Gullikson, D. McKenzie, D. Windt, L. Golub, W. Podgorski, P. Testa, and M. Weber. Initial Calibration of the Atmospheric Imaging Assembly (AIA) on the Solar Dynamics Observatory (SDO). *Sol. Phys.*, 275(1-2):41–66, 2011. doi: 10.1007/s11207-011-9804-8.

C. S. Brady and T. D. Arber. Damping of vertical coronal loop kink oscillations through wave tunneling. *A&A*, 438(2):733–740, 2005. doi: 10.1051/0004-6361:20042527.

P. J. Cargill and E. R. Priest. Siphon flows in coronal loops: I. adiabatic flow. *Sol. Phys.*, 65(2):251–269, 1980. doi: 10.1007/BF00152793.

P. J. Cargill, D. S. Spicer, and S. T. Zalesak. Magnetohydrodynamic Simulations of Alfvnic Pulse Propagation in Solar Magnetic Flux Tubes: Two-dimensional Slab Geometries. *ApJ*, 488(2):854, 1997. doi: 10.1086/304715.

S. R. Cranmer. Coronal holes. *Living Rev. Sol. Phys.*, 6(1):3, 2009. doi: 10.12942/lrsp-2009-3.

J. L. Culhane, L. K. Harra, A. M. James, K. Al-Janabi, L. J. Bradley, R. A. Chaudry, K. Rees, J. A. Tandy, P. Thomas, M. C. R. Whillock, B. Winter, G. A. Doschek, C. M. Korendyke, C. M. Brown, S. Myers, J. Mariska, J. Seely, J. Lang, B. J. Kent, B. M. Shaughnessy, P. R. Young, G. M. Simnett, C. M. Castelli, S. Mahmoud, H. Mapson-Menard, B. J. Probyn, R. J. Thomas, J. Davila, K. Dere, D. Windt, J. Shea, R. Hagood, R. Moye, H. Hara, T. Watanabe, K. Matsuzaki, T. Kosugi, V. Hansteen, and Ø. Wikstol. The EUV Imaging Spectrometer for Hinode. *Sol. Phys.*, 243(1):19–61, 2007. doi: 10.1007/s01007-007-0293-1.

R. B. Dahlburg, S. K. Antiochos, and J. A. Klimchuk. Prominence Formation by Localized Heating. *ApJ*, 495(1):485, 1998. doi: 10.1086/305286.

A. De Groof, D. Berghmans, L. Van Driel-Gesztelyi, and S. Poedts. Intensity variations in EIT shutterless mode: Waves or flows? *A&A*, 415:1141–1151, 2004. doi: 10.1051/0004-6361:20034252.

A. De Groof, C. Bastiaensen, D. A. N. Müller, D. Berghmans, and S. Poedts. Detailed comparison of downflows seen both in EIT 30.4 nm and Big Bear H-alpha movies. *A&A*, 443:319–328, 2005. doi: 10.1051/0004-6361:20053129.

I. De Moortel and C. S. Brady. Observation of Higher Harmonic Coronal Loop Oscillations. *ApJ*, 664:1210–1213, 2007. doi: 10.1086/518830.

I. De Moortel and V. M. Nakariakov. Magnetohydrodynamic waves and coronal seismology: an overview of recent results. *Phil. Trans. R. Soc. London Ser. A*, 370(1970):3193–3216, 2012. doi: 10.2307/23250393.

I. De Moortel, A. W. Hood, J. Ireland, and T. D. Arber. Phase mixing of Alfvén waves in a stratified and open atmosphere. *A&A*, 346:641–651, 1999.

I. De Moortel, J. Ireland, and R. W. Walsh. Observation of oscillations in coronal loops. *A&A*, 355:L23–L26, 2000.

I. De Moortel, A. W. Hood, J. Ireland, and R. W. Walsh. Longitudinal intensity oscillations in coronal loops observed with TRACE II. Discussion of Measured Parameters. *Sol. Phys.*, 209:89–108, 2002a. doi: 10.1023/A:1020960505133.

I. De Moortel, J. Ireland, R. W. Walsh, and A. W. Hood. Longitudinal intensity oscillations in coronal loops observed with TRACE I. Overview of Measured Parameters. *Sol. Phys.*, 209:61–88, 2002b. doi: 10.1023/A:1020956421063.

B. De Pontieu and R. Erdélyi. The nature of moss and lower atmospheric seismology. *Phil. Trans. R. Soc. London Ser. A*, 364(1839):383–394, 2006. doi: 10.1098/rsta.2005.1704.

B. De Pontieu, R. Erdélyi, and I. De Moortel. How to Channel Photospheric Oscillations into the Corona. *ApJL*, 624:L61–L64, 2005. doi: 10.1086/430345.

B. De Pontieu, S. W. McIntosh, M. Carlsson, V. H. Hansteen, T. D. Tarbell, C. J. Schrijver, A. M. Title, R. A. Shine, S. Tsuneta, Y. Katsukawa, K. Ichimoto, Y. Suematsu, T. Shimizu, and S. Nagata. Chromospheric Alfvénic Waves Strong Enough to Power the Solar Wind. *Science*, 318(5856):1574–1577, 2007. doi: 10.1126/science.1151747.

B. De Pontieu, A. M. Title, J. R. Lemen, G. D. Kushner, D. J. Akin, B. Allard, T. Berger, P. Boerner, M. Cheung, C. Chou, J. F. Drake, D. W. Duncan, S. Freeland, G. F. Heyman, C. Hoffman, N. E. Hurlburt, R. W. Lindgren, D. Mathur, R. Rehse, D. Sabolish, R. Seguin, C. J. Schrijver, T. D. Tarbell, J.-P. Wlser, C. J. Wolfson, C. Yanari, J. Mudge, N. Nguyen-Phuc, R. Timmons, R. V. Bezooijen, I. Weingrod, R. Brookner, G. Butcher, B. Dougherty, J. Eder, V. Knagenhjelm, S. Larsen, D. Mansir, L. Phan, P. Boyle, P. N. Cheimets, E. E. DeLuca, L. Golub, R. Gates, E. Hertz, S. McKillop, S. Park, T. Perry, W. A. Podgorski, K. Reeves, S. Saar, P. Testa, H. Tian, M. Weber, C. Dunn, S. Eccles, S. A. Jaeggli, C. C. Kankelborg, K. Mashburn, N. Pust, L. Springer, R. Carvalho, L. Kleint, J. Marmie, E. Mazmanian, T. M. D. Pereira, S. Sawyer, J. Strong, S. P. Worden, M. Carlsson, V. H. Hansteen, J. Leenaarts, M. Wiesmann, J. Aloise, K.-C. Chu, R. I. Bush, P. H. Scherrer, P. Brekke, J. Martínez-Sykora, B. W. Lites, S. W. McIntosh, H. Uitenbroek, T. J. Okamoto, M. A. Gummin, G. Auker, P. Jerram, P. Pool, and N. Waltham. The Interface Region Imaging Spectrograph (IRIS). *Sol. Phys.*, 289(7):2733–2779, 2014. doi: 10.1007/s11207-014-0485-y.

C. E. DeForest and J. B. Gurman. Observation of Quasi-periodic Compressive Waves in Solar Polar Plumes. *ApJL*, 501:L217–L220, 1998. doi: 10.1086/311460.

K. P. Dere and H. E. Mason. Nonthermal velocities in the solar transition zone observed with the high-resolution telescope and spectrograph. *Sol. Phys.*, 144(2): 217–241, 1993. doi: 10.1007/BF00627590.

M. L. DeRosa, C. J. Schrijver, G. Barnes, K. D. Leka, B. W. Lites, M. J. Aschwanden, T. Amari, A. Canou, J. M. McTiernan, S. Régnier, J. K. Thalmann, G. Valori, M. S. Wheatland, T. Wiegelmann, M. C. M. Cheung, P. A. Conlon, M. Fuhrmann, B. Inhester, and T. Tadesse. A Critical Assessment of Nonlinear

Force-Free Field Modeling of the Solar Corona for Active Region 10953. *ApJ*, 696 (2):1780, 2009. doi: 10.1088/0004-637X/696/2/1780.

A. J. Díaz, R. Oliver, and J. L. Ballester. Fast Magnetohydrodynamic Oscillations in Coronal Loops with Heating Profiles. *ApJ*, 645(1):766, 2006. doi: 10.1086/504145.

J. G. Doyle, Y. Taroyan, B. Ishak, M. S. Madjarska, and S. J. Bradshaw. Study of a transient siphon flow in a cold loop. *A&A*, 452(3):1075–1082, 2006. doi: 10.1051/0004-6361:20054506.

S. Dumont, Z. Mouradian, and J.-C. Pecker. Structure and physics of solar faculae. *Sol. Phys.*, 78(1):71–81, 1982. doi: 10.1007/BF00151144.

M. V. Dymova and M. S. Ruderman. Non-Axisymmetric Oscillations of Thin Prominence Fibrils. *Sol. Phys.*, 229(1):79–94, 2005. doi: 10.1007/s11207-005-5002-x.

M. V. Dymova and M. S. Ruderman. Resonantly damped oscillations of longitudinally stratified coronal loops. *A&A*, 457(3):1059–1070, 2006. doi: 10.1051/0004-6361:20065051.

P. M. Edwin and B. Roberts. Wave propagation in a magnetically structured atmosphere. *Sol. Phys.*, 76(2):239–259, 1982. doi: 10.1007/BF00170986.

P. M. Edwin and B. Roberts. Wave propagation in a magnetic cylinder. *Sol. Phys.*, 88(1-2):179–191, 1983. doi: 10.1007/BF00196186.

X. Fang, C. Xia, and R. Keppens. Multidimensional Modeling of Coronal Rain Dynamics. *ApJL*, 771(2):L29, 2013. doi: 10.1088/2041-8205/771/2/L29.

X. Fang, C. Xia, R. Keppens, and T. Van Doorsselaere. Coronal Rain in Magnetic Arcades: Rebound Shocks, Limit Cycles, and Shear Flows. *ApJ*, 807(2):142, 2015. doi: 10.1088/0004-637X/807/2/142.

G. B. Field. Thermal Instability. *ApJ*, 142:531, 1965. doi: 10.1086/148317.

P. Foukal. *Solar Astrophysics*. Wiley-Interscience, 2004.

C. Foullon, E. Verwichte, and V. M. Nakariakov. Detection of ultra-long-period oscillations in an EUV filament. *A&A*, 427(1):4, 2004. doi: 10.1051/0004-6361:200400083.

C. Foullon, E. Verwichte, and V. M. Nakariakov. Ultra-long-period Oscillations in EUV Filaments Near to Eruption: Two-wavelength Correlation and Seismology. *ApJ*, 700(2):1658, 2009.

C. Froment, F. Auchère, K. Bocchialini, E. Buchlin, C. Guennou, and J. Solomon. Evidence for Evaporation-Incomplete Condensation Cycles in Warm Solar Coronal Loops. *ApJ*, 807(2):158, 2015. doi: 10.1088/0004-637X/807/2/158.

C. Froment, F. Auchère, G. Aulanier, Z. Mikić, K. Bocchialini, E. Buchlin, and J. Solomon. Long-period Intensity Pulsations in Coronal Loops Explained by Thermal Non-equilibrium Cycles. *ApJ*, 835(2):272, 2017. doi: 10.3847/1538-4357/835/2/272.

D. W. Goldsmith. Thermal Effects in the Formation of Loop Prominences. *Sol. Phys.*, 19:86–91, 1971. doi: 10.1007/BF00148826.

L. Golub, E. DeLuca, G. Austin, J. Bookbinder, D. Caldwell, P. Cheimets, J. Cirtain, M. Cosmo, P. Reid, A. Sette, M. Weber, T. Sakao, R. Kano, K. Shibasaki, H. Hara, S. Tsuneta, K. Kumagai, T. Tamura, M. Shimojo, J. McCracken, J. Carpenter, H. Haight, R. Siler, E. Wright, J. Tucker, H. Rutledge, M. Barbera, G. Peres, and S. Varisco. The X-Ray Telescope (XRT) for the Hinode Mission. *Sol. Phys.*, 243 (1):63–86, 2007. doi: 10.1007/s11207-007-0182-1.

D. Gomez, A. Sicardi Schifino, and C. Ferro Fontan. Hopf bifurcations in coronal loops. I - Stability conditions for static equilibrium. II - Nonlinear evolution of instabilities. *ApJ*, 352:318–332, 1990. doi: 10.1086/168538.

M. Goossens, J. Andries, and M. J. Aschwanden. Coronal loop oscillations. An interpretation in terms of resonant absorption of quasi-mode kink oscillations. *A&A*, 394:L39–L42, 2002. doi: 10.1051/0004-6361:20021378.

M. Goossens, R. Erdélyi, and M. S. Ruderman. Resonant MHD Waves in the Solar Atmosphere. *Space Sci. Rev.*, 158(2-4):289–338, 2010. doi: 10.1007/s11214-010-9702-7.

D. F. Gray. *The Observation and Analysis of Stellar Photospheres*. Cambridge University Press, 2005.

M. Gruszecki and K. Murawski. Vertical oscillations of an arcade loop in a gravitationally stratified solar corona. *A&A*, 487(2):717–721, 2008. doi: 10.1051/0004-6361:20079266.

G. R. Gupta, D. Banerjee, L. Teriaca, S. Imada, and S. Solanki. Accelerating Waves in Polar Coronal Holes as Seen by EIS and SUMER. *ApJ*, 718(1):11, 2010. doi: 10.1088/0004-637X/718/1/11.

I. G. Hannah and E. P. Kontar. Differential emission measures from the regularized

inversion of Hinode and SDO data. *A&A*, 539:A146, 2012. doi: 10.1051/0004-6361/201117576.

L. K. Harra, P. Démoulin, C. H. Mandrini, S. A. Matthews, L. Van Driel-Gesztelyi, J. L. Culhane, and L. Fletcher. Flows in the solar atmosphere due to the eruptions on the 15th july, 2002. *A&A*, 438(3):1099–1106, 2005. doi: 10.1051/0004-6361:20052965.

J.-S. He, C.-Y. Tu, E. Marsch, L.-J. Guo, S. Yao, and H. Tian. Upward propagating high-frequency Alfvén waves as identified from dynamic wave-like spicules observed by SOT on Hinode. *A&A*, 497(2):525–535, 2009. doi: 10.1051/0004-6361/200810777.

J. Hershaw, C. Foullon, V. M. Nakariakov, and E. Verwichte. Damped large amplitude transverse oscillations in an EUV solar prominence, triggered by large-scale transient coronal waves. *A&A*, 531:A53, 2011. doi: 10.1051/0004-6361/201116750.

J. Heyvaerts and E. R. Priest. Coronal heating by phase-mixed shear Alfvén waves. *A&A*, 117:220–234, 1983.

E. Hildner. The formation of solar quiescent prominences by condensation. *Sol. Phys.*, 35(1):123–136, 1974. doi: 10.1007/BF00156962.

A. Hillier, H. Isobe, K. Shibata, and T. Berger. Numerical Simulations of the Magnetic Rayleigh-Taylor Instability in the Kippenhahn-Schlter Prominence Model. II. Reconnection-triggered Downflows. *ApJ*, 756(2):110, 2012. doi: 10.1088/0004-637X/756/2/110.

J. V. Hollweg and G. Yang. Resonance absorption of compressible magnetohydrodynamic waves at thin surfaces. *J. Geophys. Res.*, 93(A6):5423–5436, 1988. doi: 10.1029/JA093iA06p05423.

A. W. Hood and E. R. Priest. Kink instability of solar coronal loops as the cause of solar flares. *Sol. Phys.*, 64:303–321, 1979. doi: 10.1007/BF00151441.

D. E. Innes, W. Curdt, R. Schwenn, S. Solanki, G. Stenborg, and D. E. McKenzie. Large doppler shifts in x-ray plasma: An explosive start to coronal mass ejection. *ApJ*, 549(2):L249, 2001. doi: 10.1086/319164.

D. E. Innes, D. E. McKenzie, and T. Wang. Observations of 1000 km/s doppler shifts in 107 K solar flare supra-arcade. *Sol. Phys.*, 217(2):267–279, 2003. doi: 10.1023/B:SOLA.0000006874.31799.bc.

D. B. Jess, M. Mathioudakis, R. Erdélyi, P. J. Crockett, F. P. Keenan, and D. J. Christian. Alfvén Waves in the Lower Solar Atmosphere. *Science*, 323(5921): 1582–1585, 2009. doi: 10.1126/science.1168680.

D. B. Jess, D. J. Pascoe, D. J. Christian, M. Mathioudakis, P. H. Keys, and F. P. Keenan. The Origin of Type I Spicule Oscillations. *ApJL*, 744(1):L5, 2012. doi: 10.1088/2041-8205/744/1/L5.

J. Jing, J. Lee, T. J. Spirock, Y. Xu, H. Wang, and G. S. Choe. Periodic Motion along a Solar Filament Initiated by a Subflare. *ApJ*, 584(2):L103, 2003. doi: 10.1086/373886.

M. L. Kaiser. The STEREO mission: an overview. *Adv. Space Res.*, 36(8):1483–1488, 2005. doi: 10.1016/j.asr.2004.12.066.

S. Kamio, H. Peter, W. Curdt, and S. K. Solanki. Continuous upflows and sporadic downflows observed in active regions. *A&A*, 532:A96, 2011. doi: 10.1051/0004-6361/201117188.

J. T. Karpen, S. K. Antiochos, M. Hohensee, J. A. Klimchuk, and P. J. MacNeice. Are Magnetic Dips Necessary for Prominence Formation? *ApJ*, 553(1):L85, 2001. doi: 10.1086/320497.

J. T. Karpen, S. E. M. Tanner, S. K. Antiochos, and C. R. DeVore. Prominence Formation by Thermal Nonequilibrium in the Sheared-Arcade Model. *ApJ*, 635 (2):1319, 2005. doi: 10.1086/497531.

J. T. Karpen, S. K. Antiochos, and J. A. Klimchuk. The Origin of High-Speed Motions and Threads in Prominences. *ApJ*, 637(1):531, 2006. doi: 10.1086/498237.

I. Kawaguchi. Observed Interaction between Prominences. *PASJ*, 22:405, 1970.

C. U. Keller, M. Schüssler, A. Vögler, and V. Zakharov. On the origin of solar faculae. *ApJ*, 607(1):L59, 2004. doi: 10.1086/421553.

L. Kleint, P. Antolin, H. Tian, P. Judge, P. Testa, B. De Pontieu, J. Martínez-Sykora, K. K. Reeves, J. P. Wuelser, S. McKillop, S. Saar, M. Carlsson, P. Boerner, N. Hurlburt, J. Lemen, T. D. Tarbell, A. Title, L. Golub, V. Hansteen, S. Jaeggli, and C. Kankelborg. Detection of Supersonic Downflows and Associated Heating Events in the Transition Region above Sunspots. *ApJ*, 789(2):L42, 2014. doi: 10.1088/2041-8205/789/2/L42.

B. Kliem, I. E. Dammasch, W. Curdt, and K. Wilhelm. Correlated Dynamics of

Hot and Cool Plasmas in the Main Phase of a Solar Flare. *ApJL*, 568:L61–L65, 2002. doi: 10.1086/340136.

J. A. Klimchuk and P. J. Cargill. Spectroscopic Diagnostics of Nanoflare-heated Loops. *ApJ*, 553(1):440, 2001. doi: 10.1086/320666.

P. Kohutova and E. Verwichte. Analysis of Coronal Rain Observed by IRIS, HINODE/SOT, and SDO/AIA: Transverse Oscillations, Kinematics, and Thermal Evolution. *ApJ*, 827(1):39, 2016. doi: 10.3847/0004-637X/827/1/39.

P. Kohutova and E. Verwichte. Dynamics of plasma condensations in a gravitationally stratified coronal loop. *A&A*, 602:A23, 2017a. doi: 10.1051/0004-6361/201629912.

P. Kohutova and E. Verwichte. Excitation of vertical coronal loop oscillations by plasma condensations. *A&A*, 606:A120, 2017b. doi: 10.1051/0004-6361/201731417.

P. Kohutova and E. Verwichte. Excitation of vertical coronal loop oscillations by impulsively driven flows. *A&A, in press*, 2018.

T. Kosugi, K. Matsuzaki, T. Sakao, T. Shimizu, Y. Sone, S. Tachikawa, T. Hashimoto, K. Minesugi, A. Ohnishi, T. Yamada, S. Tsuneta, H. Hara, K. Ichimoto, Y. Suematsu, M. Shimojo, T. Watanabe, S. Shimada, J. M. Davis, L. D. Hill, J. K. Owens, A. M. Title, J. L. Culhane, L. K. Harra, G. A. Doschek, and L. Golub. The Hinode (Solar-B) Mission: An Overview. *Sol. Phys.*, 243(1):3–17, 2007. doi: 10.1007/s11207-007-9014-6.

N. P. M. Kuin and P. C. H. Martens. On the thermal stability of hot coronal loops - The coupling between chromosphere and corona. *A&A*, 108:L1–L4, 1982.

P. Kumar, D. E. Innes, and B. Inhester. Solar Dynamics Observatory/Atmospheric Imaging Assembly Observations of a Reflecting Longitudinal Wave in a Coronal Loop. *ApJL*, 779(1):L7, 2013. doi: 10.1088/2041-8205/779/1/L7.

N. Labrosse, P. Heinzel, J.-C. Vial, T. Kucera, S. Parenti, S. Gunár, B. Schmieder, and G. Kilper. Physics of solar prominences: I-spectral diagnostics and non-LTE modelling. *Space Sci. Rev.*, 151(4):243–332, 2010. doi: 10.1007/s11214-010-9630-6.

J. R. Lemen, A. M. Title, D. J. Akin, P. F. Boerner, C. Chou, J. F. Drake, D. W. Duncan, C. G. Edwards, F. M. Friedlaender, G. F. Heyman, N. E. Hurlburt, N. L. Katz, G. D. Kushner, M. Levay, R. W. Lindgren, D. P. Mathur, E. L. McFeaters,

S. Mitchell, R. A. Rehse, C. J. Schrijver, L. A. Springer, R. A. Stern, T. D. Tarbell, J.-P. Wuelser, C. J. Wolfson, C. Yanari, J. A. Bookbinder, P. N. Cheimets, D. Caldwell, E. E. DeLuca, R. Gates, L. Golub, S. Park, W. A. Podgorski, R. I. Bush, P. H. Scherrer, M. A. Gummin, P. Smith, G. Auker, P. Jerram, P. Pool, R. Soufli, D. L. Windt, S. Beardsley, M. Clapp, J. Lang, and N. Waltham. The Atmospheric Imaging Assembly (AIA) on the Solar Dynamics Observatory (SDO). *Sol. Phys.*, 275(1-2):17–40, 2012. doi: 10.1007/s11207-011-9776-8.

J.-L. Leroy. Emissions 'froides' dans la couronne solaire. *Sol. Phys.*, 25:413–417, 1972. doi: 10.1007/BF00192338.

M. Luna, J. T. Karpen, and C. R. DeVore. Formation and Evolution of a Multi-threaded Solar Prominence. *ApJ*, 746(1):30, 2012. doi: 10.1088/0004-637X/746/1/30.

M. Luna, K. Knizhnik, K. Muglach, J. Karpen, H. Gilbert, T. A. Kucera, and V. Uritsky. Observations and Implications of Large-amplitude Longitudinal Oscillations in a Solar Filament. *ApJ*, 785(1):79, 2014. doi: 10.1088/0004-637X/785/1/79.

D. Mackay and K. Galsgaard. Evolution of a Density Enhancement in a Stratified Atmosphere With Uniform Vertical Magnetic Field. *Sol. Phys.*, 198(2):289–312, 2001. doi: 10.1023/A:1005266330720.

D. H. Mackay, J. T. Karpen, J. L. Ballester, B. Schmieder, and G. Aulanier. Physics of solar prominences: II-magnetic structure and dynamics. *Space Sci. Rev.*, 151 (4):333–399, 2010. doi: 10.1007/s11214-010-9628-0.

N. Magyar, T. Van Doorsselaere, and A. Marcu. Numerical simulations of transverse oscillations in radiatively cooling coronal loops. *A&A*, 582:A117, 2015. doi: 10.1051/0004-6361/201526287.

S. Mandal, D. Yuan, X. Fang, D. Banerjee, V. Pant, and T. Van Doorsselaere. Reflection of Propagating Slow Magneto-acoustic Waves in Hot Coronal Loops: Multi-instrument Observations and Numerical Modeling. *ApJ*, 828(2):72, 2016. doi: 10.3847/0004-637X/828/2/72.

J. T. Mariska. Observational signatures of loop flows driven by asymmetric heating. *ApJ*, 334:489, 1988. doi: 10.1086/166853.

J. T. Mariska and J. P. Boris. Dynamics and spectroscopy of asymmetrically heated coronal loops. *ApJ*, 267:409–420, 1983. doi: 10.1086/160879.

E. Marsch, H. Tian, J. Sun, W. Curdt, and T. Wiegelmann. Plasma Flows Guided by Strong Magnetic Fields in the Solar Corona. *ApJ*, 685(2):1262, 2008. doi: 10.1086/591038.

M. S. Marsh, R. W. Walsh, I. De Moortel, and J. Ireland. Joint observations of propagating oscillations with SOHO/CDS and TRACE. *A&A*, 404(2):L37–L41, 2003. doi: 10.1051/0004-6361:20030709.

J.-C. Martínez Oliveros, S. Krucker, H. S. Hudson, P. Saint-Hilaire, H. Bain, C. Lindsey, R. Bogart, S. Couvidat, P. Scherrer, and J. Schou. Chromospheric and Coronal Observations of Solar Flares with the Helioseismic and Magnetic Imager. *ApJ*, 780(2):L28, 2014. doi: 10.1088/2041-8205/780/2/L28.

A. N. McClymont and I. J. D. Craig. Fast downflows in the solar transition region explained. *ApJ*, 312:402, 1987. doi: 10.1086/164885.

M. P. McEwan, G. R. Donnelly, A. J. Daz, and B. Roberts. On the period ratio P1/2P2 in the oscillations of coronal loops. *A&A*, 460(3):893–899, 2006. doi: 10.1051/0004-6361:20065313.

S. W. McIntosh, B. De Pontieu, M. Carlsson, V. Hansteen, P. Boerner, and M. Goossens. Alfvénic waves with sufficient energy to power the quiet solar corona and fast solar wind. *Nature*, 475(7357):477–480, 2011. doi: 10.1038/nature10235.

S. W. McIntosh, H. Tian, M. Sechler, and B. De Pontieu. On the Doppler Velocity of Emission Line Profiles Formed in the "Coronal Contraflow" that Is the Chromosphere-Corona Mass Cycle. *ApJ*, 749(1):60, 2012. doi: 10.1088/0004-637X/749/1/60.

V. F. Melnikov, V. E. Reznikova, K. Shibasaki, and V. M. Nakariakov. Spatially resolved microwave pulsations of a flare loop. *A&A*, 439(2):727–736, 2005. doi: 10.1051/0004-6361:20052774.

C. A. Mendoza-Briceño, L. D. G. Sigalotti, and R. Erdélyi. Catastrophic Cooling of Impulsively Heated Coronal Loops. *ApJ*, 624(2):1080, 2005. doi: 10.1086/429249.

C. D. Meyer, D. S. Balsara, and T. D. Aslam. A second-order accurate super TimeStepping formulation for anisotropic thermal conduction. *MNRAS*, 422(3): 2102, 2012. doi: 10.1111/j.1365-2966.2012.20744.x.

C. D. Meyer, D. S. Balsara, and T. D. Aslam. A stabilized Runge-Kutta-Legendre method for explicit super-time-stepping of parabolic and mixed equations. *J. Comput. Phys.*, 257:594, 2014. doi: 10.1016/j.jcp.2013.08.021.

Y. Mok, J. F. Drake, D. D. Schnack, and G. Van Hoven. Prominence formation in a coronal loop. *ApJ*, 359:228–231, 1990. doi: 10.1086/169053.

G. E. Moreton and H. E. Ramsey. Recent Observations of Dynamical Phenomena Associated with Solar Flares. *Publ. Astron. Soc. Pac.*, 72:357, 1960. doi: 10.1086/127549.

R. J. Morton and R. Erdélyi. Transverse Oscillations of a Cooling Coronal Loop. *ApJ*, 707(1):750, 2009. doi: 10.1088/0004-637X/707/1/750.

T. Mrozek. Failed Eruption of a Filament as a Driver for Vertical Oscillations of Coronal Loops. *Sol. Phys.*, 270(1):191, 2011. doi: 10.1007/s11207-011-9750-5.

D. A. N. Müller, V. H. Hansteen, and H. Peter. Dynamics of solar coronal loops - I. Condensation in cool loops and its effect on transition region lines. *A&A*, 411 (3):9, 2003. doi: 10.1051/0004-6361:20031328.

D. A. N. Müller, H. Peter, and V. H. Hansteen. Dynamics of solar coronal loops - II. Catastrophic cooling and high-speed downflows. *A&A*, 424(1):12, 2004. doi: 10.1051/0004-6361:20040403.

D. A. N. Müller, A. De Groof, V. H. Hansteen, and H. Peter. High-speed coronal rain. *A&A*, 436(3):1067–1074, 2005. doi: 10.1051/0004-6361:20042141.

V. M. Nakariakov and B. Roberts. On fast magnetosonic coronal pulsations. *Sol. Phys.*, 159(2):399–402, 1995. doi: 10.1007/BF00686541.

V. M. Nakariakov and E. Verwichte. Coronal Waves and Oscillations. *Living Rev. Sol. Phys.*, 2:3, 2005. doi: 10.12942/lrsp-2005-3.

V. M. Nakariakov, L. Ofman, E. E. DeLuca, B. Roberts, and J. M. Davila. TRACE observation of damped coronal loop oscillations: Implications for coronal heating. *Science*, 285:862–864, 1999. doi: 10.1126/science.285.5429.862.

V. M. Nakariakov, E. Verwichte, D. Berghmans, and E. Robbrecht. Slow magnetoacoustic waves in coronal loops. *A&A*, 362:1151–1157, 2000.

V. M. Nakariakov, V. F. Melnikov, and V. E. Reznikova. Global sausage modes of coronal loops. *A&A*, 412(1):L7–L10, 2003. doi: 10.1051/0004-6361:20031660.

V. M. Nakariakov, M. J. Aschwanden, and T. Van Doorsselaere. The possible role of vortex shedding in the excitation of kink-mode oscillations in the solar corona. *A&A*, 502:661–664, 2009. doi: 10.1051/0004-6361/200810847.

G. Nisticò, V. M. Nakariakov, and E. Verwichte. Decaying and decayless transverse oscillations of a coronal loop. *A&A*, 552:A57, 2013. doi: 10.1051/0004-6361/201220676.

L. Ofman. Chromospheric Leakage of Alfvn Waves in Coronal Loops. *ApJ*, 568(2): L135, 2002. doi: 10.1086/340329.

L. Ofman, M. Romoli, G. Poletto, G. Noci, and J. L. Kohl. Ultraviolet Coronagraph Spectrometer Observations of Density Fluctuations in the Solar Wind. *ApJL*, 491: L111–L114, 1997. doi: 10.1086/311067.

L. Ofman, V. M. Nakariakov, and C. E. DeForest. Slow Magnetosonic Waves in Coronal Plumes. *ApJ*, 514:441–447, 1999. doi: 10.1086/306944.

L. Ofman, T. J. Wang, and J. M. Davila. Slow magnetosonic waves and fast flows in active region loops. *ApJ*, 754:111, 2012. doi: 10.1088/0004-637X/754/2/111.

T. J. Okamoto, S. Tsuneta, T. E. Berger, K. Ichimoto, Y. Katsukawa, B. W. Lites, S. Nagata, K. Shibata, T. Shimizu, R. A. Shine, Y. Suematsu, T. D. Tarbell, and A. M. Title. Coronal Transverse Magnetohydrodynamic Waves in a Solar Prominence. *Science*, 318(5856):1577–1580, 2007. doi: 10.1126/science.1145447.

T. J. Okamoto, P. Antolin, B. De Pontieu, H. Uitenbroek, T. Van Doorsselaere, and T. Yokoyama. Resonant Absorption of Transverse Oscillations and Associated Heating in a Solar Prominence. I. Observational Aspects. *ApJ*, 809(1):71, 2015. doi: 10.1088/0004-637X/809/1/71.

R. Oliver, R. Soler, J. Terradas, T. V. Zaqarashvili, and M. L. Khodachenko. Dynamics of Coronal Rain and Descending Plasma Blobs in Solar Prominences. I. Fully Ionized Case. *ApJ*, 784(1):21, 2014. doi: 10.1088/0004-637X/784/1/21.

S. Orlando, S. Serio, and G. Peres. Stationary flows in coronal loops. *Space Sci. Rev.*, 70(1):203–206, 1994. doi: 10.1007/BF00777869.

V. S. Pandey and B. N. Dwivedi. Strong and Weak Damping of Slow MHD Standing Waves in Hot Coronal Loops. *Sol. Phys.*, 236(1):127–136, 2006. doi: 10.1007/s11207-006-0123-4.

S. Parenti. Solar prominences: Observations. *Living Rev. Sol. Phys.*, 11(1):1, 2014. doi: 10.12942/lrsp-2014-1.

E. N. Parker. Instability of Thermal Fields. *ApJ*, 117:431, 1953. doi: 10.1086/145707.

E. N. Parker. Hydromagnetic Dynamo Models. *ApJ*, 122:293, 1955. doi: 10.1086/146087.

G. W. Pneuman. Some general properties of helmeted coronal structures. *Sol. Phys.*, 3:578–597, 1968. doi: 10.1007/BF00151939.

G. Poletto. Solar coronal plumes. *Living Rev. Sol. Phys.*, 12(1):7, 2015. doi: 10.1007/lrsp-2015-7.

E. R. Priest. The structure of coronal loops. *Sol. Phys.*, 58:57–87, 1978. doi: 10.1007/BF00152555.

E. R. Priest. *Solar Magnetohydrodynamics*. Springer, 1982.

R. Rankin, P. Frycz, V. T. Tikhonchuk, and J. C. Samson. Nonlinear standing shear Alfvén waves in the Earth's magnetosphere. *J. Geophys. Res.*, 99(A11): 21291–21301, 1994. doi: 10.1029/94JA01629.

E. Robbrecht, E. Verwichte, D. Berghmans, J. F. Hochedez, S. Poedts, and V. M. Nakariakov. Slow magnetoacoustic waves in coronal loops: EIT and TRACE. *A&A*, 370:591–601, 2001. doi: 10.1051/0004-6361:20010226.

R. Rosner, W. H. Tucker, and G. S. Vaiana. Dynamics of the quiescent solar corona. *ApJ*, 220:643–645, 1978. doi: 10.1086/155949.

M. S. Ruderman. Transverse Oscillations of Coronal Loops with Slowly Changing Density. *Sol. Phys.*, 271(1-2):41–54, 2011. doi: 10.1007/s11207-011-9772-z.

M. S. Ruderman and R. Erdélyi. Transverse Oscillations of Coronal Loops. *Space Sci. Rev.*, 149(1-4):199–228, 2009. doi: 10.1007/s11214-009-9535-4.

M. S. Ruderman and B. Roberts. The Damping of Coronal Loop Oscillations. *ApJ*, 577:475–486, 2002. doi: 10.1086/342130.

M. S. Ruderman, G. Verth, and R. Erdélyi. Transverse Oscillations of Longitudinally Stratified Coronal Loops with Variable Cross Section. *ApJ*, 686(1):694, 2008. doi: 10.1086/591444.

G. B. Scharmer. Comments on the optimization of high resolution Fabry-Pérot filtergraphs. *A&A*, 447(3):1111–1120, 2006. doi: 10.1051/0004-6361:20052981.

P. H. Scherrer, J. Schou, R. I. Bush, A. G. Kosovichev, R. S. Bogart, J. T. Hoeksema, Y. Liu, T. L. Duvall, J. Zhao, A. M. Title, C. J. Schrijver, T. D. Tarbell, and S. Tomczyk. The Helioseismic and Magnetic Imager (HMI) Investigation for the

Solar Dynamics Observatory (SDO). *Sol. Phys.*, 275(1-2):207–227, 2012. doi: 10.1007/s11207-011-9834-2.

C. J. Schrijver. Catastrophic cooling and high-speed downflow in quiescent solar coronal loops observed with TRACE. *Sol. Phys.*, 198(2):325–345, 2001. doi: 10.1023/A:1005211925515.

C. J. Schrijver, M. J. Aschwanden, and A. M. Title. Transverse oscillations in coronal loops observed with TRACE I. An Overview of Events, Movies, and a Discussion of Common Properties and Required Conditions. *Sol. Phys.*, 206(1): 69–98, 2002. doi: 10.1023/A:1014957715396.

E. Scullion, L. Rouppe van der Voort, P. Antolin, S. Wedemeyer, G. Vissers, E. P. Kontar, and P. T. Gallagher. Observing the Formation of Flare-driven Coronal Rain. *ApJ*, 833(2):184, 2016. doi: 10.3847/1538-4357/833/2/184.

M. Selwa, K. Murawski, S. K. Solanki, and L. Ofman. Excitation of vertical kink waves in a solar coronal arcade loop by a periodic driver. *A&A*, 512:A76, 2010. doi: 10.1051/0004-6361/200912603.

S. Serio, G. Peres, G. S. Vaiana, L. Golub, and R. Rosner. Closed coronal structures. II - Generalized hydrostatic model. *ApJ*, 243:288–300, 1981. doi: 10.1086/158597.

S. K. Solanki. Sunspots: An overview. *The Astron. Astrophys. Rev.*, 11(2):153–286, 2003. doi: 10.1007/s00159-003-0018-4.

H. C. Spruit, A. Nordlund, and A. M. Title. Solar convection. *Annu. Rev. Astron. Astrophys.*, 28(1):263–303, 1990. doi: 10.1146/annurev.aa.28.090190.001403.

A. C. Sterling. Solar spicules: A review of recent models and targets for future observations (invited review). *Sol. Phys.*, 196(1):79–111, 2000. doi: 10.1023/A:1005213923962.

L. Teriaca, D. Banerjee, A. Falchi, J. G. Doyle, and M. S. Madjarska. Transition region small-scale dynamics as seen by SUMER on SOHO. *A&A*, 427(3):1065–1074, 2004. doi: 10.1051/0004-6361:20040503.

J. Terradas and L. Ofman. Loop Density Enhancement by Nonlinear Magnetohydrodynamic Waves. *ApJ*, 610(1):523–531, 2004. doi: 10.1086/421514.

J. Terradas, J. Andries, M. Goossens, I. Arregui, R. Oliver, and J. L. Ballester. Nonlinear instability of kink oscillations due to shear motions. *ApJ*, 687(2):L115, 2008. doi: 10.1086/593203.

J. Terradas, I. Arregui, G. Verth, and M. Goossens. Seismology of transversely oscillating coronal loops with siphon flows. *ApJL*, 729(2):L22, 2011. doi: 10.1088/2041-8205/729/2/L22.

B. J. Thompson, S. P. Plunkett, J. B. Gurman, J. S. Newmark, O. C. St. Cyr, and D. J. Michels. SOHO/EIT observations of an Earth-directed coronal mass ejection on May 12, 1997. *Geophys. Res. Lett.*, 25:2465–2468, 1998. doi: 10.1029/98GL50429.

H. Tian, W. Curdt, E. Marsch, and J. He. Cool and hot components of a coronal bright point. *ApJ*, 681(2):L121, 2008. doi: 10.1086/590410.

H. Tian, E. Marsch, W. Curdt, and J. He. Upflows in funnel-like legs of coronal magnetic loops. *ApJ*, 704(1):883, 2009. doi: 10.1088/0004-637X/704/1/883.

A. N. Tikhonov. Solution of incorrectly formulated problems and the regularization method. *Soviet Math. Dokl.*, 4:1035, 1963.

S. Tomczyk, S. W. McIntosh, S. L. Keil, P. G. Judge, T. Schad, D. H. Seeley, and J. Edmondson. Alfvén Waves in the Solar Corona. *Science*, 317:1192, 2007. doi: 10.1126/science.1143304.

R. H. D. Townsend. An Exact Integration Scheme for Radiative Cooling in Hydrodynamical Simulations. *ApJS*, 181(2):391, 2009. doi: 10.1088/0067-0049/181/2/391.

S. Tsuneta, K. Ichimoto, Y. Katsukawa, S. Nagata, M. Otsubo, T. Shimizu, Y. Suematsu, M. Nakagiri, M. Noguchi, T. Tarbell, A. Title, R. Shine, W. Rosenberg, C. Hoffmann, B. Jurcevich, G. Kushner, M. Levay, B. Lites, D. Elmore, T. Matsushita, N. Kawaguchi, H. Saito, I. Mikami, L. D. Hill, and J. K. Owens. The Solar Optical Telescope for the Hinode Mission: An Overview. *Sol. Phys.*, 249 (2):167–196, 2008. doi: 10.1007/s11207-008-9174-z.

I. Ugarte-Urra, A. R. Winebarger, and H. P. Warren. An Investigation into the Variability of Heating in a Solar Active Region. *ApJ*, 643:1245–1257, 2006. doi: 10.1086/503196.

I. Ugarte-Urra, H. P. Warren, and D. H. Brooks. Active Region Transition Region Loop Populations and Their Relationship to the Corona. *ApJ*, 695:642–651, 2009. doi: 10.1088/0004-637X/695/1/642.

T. Van Doorsselaere, V. M. Nakariakov, and E. Verwichte. Coronal loop seismology using multiple transverse loop oscillation harmonics. *A&A*, 473(3):959–966, 2007. doi: 10.1051/0004-6361:20077783.

T. Van Doorsselaere, D. C. C. Birtill, and G. R. Evans. Detection of three periodicities in a single oscillating coronal loop. *A&A*, 508(3):1485–1491, 2009. doi: 10.1051/0004-6361/200912753.

E. Verwichte and P. Kohutova. Excitation and evolution of vertically polarised transverse loop oscillations by coronal rain. *A&A*, 601:L2, 2017. doi: 10.1051/0004-6361/201730675.

E. Verwichte, V. M. Nakariakov, and A. W. Longbottom. On the evolution of a nonlinear alfvén pulse. *J. Plasma Phys.*, 62(2):219, 1999.

E. Verwichte, V. M. Nakariakov, L. Ofman, and E. E. DeLuca. Characteristics of transverse oscillations in a coronal loop arcade. *Sol. Phys.*, 223(1):77–94, 2004. doi: 10.1007/s11207-004-0807-6.

E. Verwichte, M. J. Aschwanden, T. Van Doorsselaere, C. Foullon, and V. M. Nakariakov. Seismology of a Large Solar Coronal Loop from EUVI/STEREO Observations of its Transverse Oscillation. *ApJ*, 698(1):397, 2009. doi: 10.1088/0004-637X/698/1/397.

E. Verwichte, C. Foullon, and T. Van Doorsselaere. Spatial Seismology of a Large Coronal Loop Arcade from TRACE and EIT Observations of its Transverse Oscillations. *ApJ*, 717(1):458, 2010. doi: 10.1088/0004-637X/717/1/458.

E. Verwichte, P. Antolin, G. Rowlands, P. Kohutova, and T. Neukirch. Kinematics of coronal rain in a transversely oscillating loop: Ponderomotive force and rain-excited oscillations. *A&A*, 598:A57, 2017a. doi: 10.1051/0004-6361/201629634.

E. Verwichte, P. Kohutova, P. Antolin, G. Rowlands, and T. Neukirch. Excitation and evolution of transverse loop oscillations by coronal rain. *Proc. Int. Astron. Union, in press*, 2017b.

T. Wang, S. K. Solanki, W. Curdt, D. E. Innes, and I. E. Dammasch. Doppler Shift Oscillations of Hot Solar Coronal Plasma Seen by SUMER: A Signature of Loop Oscillations? *ApJL*, 574:L101–L104, 2002. doi: 10.1086/342189.

T. Wang, D. E. Innes, and J. Qiu. Determination of the Coronal Magnetic Field from Hot-Loop Oscillations Observed by SUMER and SXT. *ApJ*, 656(1):598, 2007. doi: 10.1086/510424.

T. Wang, L. Ofman, J. M. Davila, and Y. Su. Growing Transverse Oscillations of a Multistranded Loop Observed by SDO/AIA. *ApJ*, 751(2):L27, 2012. doi: 10.1088/2041-8205/751/2/L27.

T. J. Wang and S. K. Solanki. Vertical oscillations of a coronal loop observed by TRACE. *A&A*, 421(2):L33–L36, 2004. doi: 10.1051/0004-6361:20040186.

T. J. Wang, S. K. Solanki, W. Curdt, D. E. Innes, I. E. Dammasch, and B. Kliem. Hot coronal loop oscillations observed with SUMER: Examples and statistics. *A&A*, 406(3):1105–1121, 2003a. doi: 10.1051/0004-6361:20030858.

T. J. Wang, S. K. Solanki, D. E. Innes, W. Curdt, and E. Marsch. Slow-mode standing waves observed by SUMER in hot coronal loops. *A&A*, 402(2):L17–L20, 2003b. doi: 10.1051/0004-6361:20030448.

T. J. Wang, L. Ofman, and J. M. Davila. Propagating Slow Magnetoacoustic Waves in Coronal Loops Observed by Hinode/EIS. *ApJ*, 696(2):1448, 2009. doi: 10.1088/0004-637X/696/2/1448.

H. P. Warren, A. R. Winebarger, and D. H. Brooks. Evidence for Steady Heating: Observations of an Active Region Core with Hinode and TRACE. *ApJ*, 711(1): 228, 2010. doi: 10.1088/0004-637X/711/1/228.

S. Wedemeyer-Böhm, A. Lagg, and Å. Nordlund. Coupling from the Photosphere to the Chromosphere and the Corona. *Space Sci. Rev.*, 144(1-4):317–350, 2009. doi: 10.1007/s11214-008-9447-8.

R. S. White and E. Verwichte. Transverse coronal loop oscillations seen in unprecedented detail by AIA/SDO. *A&A*, 537:A49, 2012. doi: 10.1051/0004-6361/201118093.

R. S. White, E. Verwichte, and C. Foullon. First observation of a transverse vertical oscillation during the formation of a hot post-flare loop. *A&A*, 545:A129, 2012. doi: 10.1051/0004-6361/201219856.

R. S. White, E. Verwichte, and C. Foullon. Anti-phase Signature of Flare Generated Transverse Loop Oscillations. *ApJ*, 774(2):104, 2013. doi: 10.1088/0004-637X/774/2/104.

D. R. Williams, K. J. H. Phillips, P. Rudawy, M. Mathioudakis, P. T. Gallagher, E. O'Shea, F. P. Keenan, P. Read, and B. Rompolt. High-frequency oscillations in a solar active region coronal loop. *MNRAS*, 326:428–436, 2001. doi: 10.1046/j.1365-8711.2001.04491.x.

A. P. Witkin. Scale-space Filtering. In *Proc. Int. Joint Conf. Artificial Intell.*, page 1019, 1983.

T. N. Woods, F. G. Eparvier, R. Hock, A. R. Jones, D. Woodraska, D. Judge, L. Didkovsky, J. Lean, J. Mariska, H. Warren, D. McMullin, P. Chamberlin, G. Berthiaume, S. Bailey, T. Fuller-Rowell, J. Sojka, W. K. Tobiska, and R. Viereck. Extreme Ultraviolet Variability Experiment (EVE) on the Solar Dynamics Observatory (SDO): Overview of Science Objectives, Instrument Design, Data Products, and Model Developments. *Sol. Phys.*, 275(1-2):115–143, 2012. doi: 10.1007/s11207-009-9487-6.

C. Xia, P. F. Chen, R. Keppens, and A. J. Van Marle. Formation of Solar Filaments by Steady and Nonsteady Chromospheric Heating. *ApJ*, 737(1):27, 2011. doi: 10.1088/0004-637X/737/1/27.

C. Xia, P. F. Chen, and R. Keppens. Simulations of Prominence Formation in the Magnetized Solar Corona by Chromospheric Heating. *ApJL*, 748(2):L26, 2012. doi: 10.1088/2041-8205/748/2/L26.

V. V. Zaitsev and A. V. Stepanov. On the Origin of the Hard X-Ray Pulsations during Solar Flares. *Sov. Astron. Lett.*, 8:132–134, 1982.

Q. M. Zhang, P. F. Chen, C. Xia, and R. Keppens. Observations and simulations of longitudinal oscillations of an active region prominence. *A&A*, 542:A52, 2012. doi: 10.1051/0004-6361/201218786.